Doctoral Dissertation
Doctoral Program in Electrical, Electronics and Communications Engineering
(33th Cycle)

Research on graphene/silicon Schottky junction based photodetector

Yiming Wang
* * * * * *

Supervisors
Prof. Shuming Yang, Supervisor
Prof. Fabrizio Candido Pirri, Co-Supervisor

Doctoral Examination Committee:
Prof. Mingxing Jiao, Xi'an University of Technology
Prof. Shiyu Wang, Xidian University
Prof. Hui Ding, Xi'an Jiaotong University
Prof. Shuhai Jia, Xi'an Jiaotong University
Prof. Elena Maria Tresso, Politecnico di Torino
Prof. Alberto Tagliaferro, Politecnico di Torino
Prof. Stefano Bianco, Politecnico di Torino

Politecnico di Torino
May 2, 2021

I hereby declare that, the contents and organisation of this dissertation constitute my own original work and does not compromise in any way the rights of third parties, including those relating to the security of personal data.

…….....

Yiming Wang

Xi'an, May 2, 2020

Summary

Photodetector based on traditional semiconductor materials has stable performance, mature technology and wide application, but it also faces many problems. The doping concentration of impurities in the monoatomic semiconductor is limited by the solid solubility of the material itself; the control of the element types and contents in the multi-component semiconductor is complex; and some semiconductors for photodetection are synthesized with toxic source materials. These disadvantages limit the application and development of traditional semiconductor materials. Graphene is a two-dimensional material composed of monolayer carbon atoms, which has excellent photoelectric properties such as wide spectral absorption and high carrier mobility. Graphene/silicon (Gr/Si) Schottky junction photodetector can be constructed by simply transferring graphene to silicon substrate. Compared with traditional semiconductor photodetectors, the fabrication process is simple. Due to the rectifying characteristics of Schottky junction, under reverse bias the dark current is small, which leads to high on-off ratio and detectivity. In this work, the graphene/silicon Schottky junction photodetectors were studied. The graphene oxide (GO) interface layer and gold nanoparticles (AuNPs) are used to improve the photoelectric performance of Gr/Si photodetector. Two-step hot-embossing method was proposed to directly transferr graphene and fabricate Gr/Si Schottky photodetector.

1. Single layer graphene films were grown by chemical vapor deposition (CVD) method and used to fabricate Gr/Si Schottky photodetector. The results of Raman spectroscopy, SEM and AFM indicated that the graphene was monolayer. After transferring by PMMA temporary support layer, graphene still had good integrity and continuity, while PMMA residue with thickness of about 5 nm existed on the surface. Gr/Si Schottky junction photodetector was fabricated by metal deposition, photolithography and lift-off. The responsivity of the detector

was 0.23 A/W and the on-off ratio reached 3.7×10^3 under 633 nm illumination. The detector responded quickly and accurately to the periodic optical signals with different power density, and the response time was about 1ms.

2. The performance of Gr/Si Schottky photodetectors was improved by inserting a graphene oxide film as interfacial layer. The interface between graphene and silicon normally contains a relatively high density of surface states, which leads to Fermi level pinning and increases the leakage current noise, thus limits the overall performance of Gr/Si Schottky photodetector. The inserted GO interfacial layer can enhance the interface properties, the results show that the dark current of Gr/GO/Si photodetector was 26 times lower than that of the Gr/Si photodetector, and the photocurrent is 2.73 times higher than Gr/Si detector. Under 633 nm illumination the responsivity reached 0.65 A/W. After inserting GO interfacial layer, the series resistance of the device had no obvious change, while the Schottky barrier height and shunt resistance increased significantly. The dark current of graphene photodetector was reduced due to the suppression of reverse saturation current. The enhancement of photocurrent was attributed to multiple factors, including the increase of Schottky barrier height, the extra light absorption of GO interlayer and the passivation of Schottky junction interface.

3. AuNPs obtained by two different methods, thin film annealing and electron beam lithography, were used to enhance the performance of Gr/Si Schottky junction photodetectors. By coupling gold nanoparticles to graphene surface, the optical near-field intensity of the photosensitive region can be enhanced by surface plasma resonance effect, which can effectively improve the photoelectric response of Gr/Si Schottky photodetector. AuNPs obtained by thin film annealing were disorderly distributed semi ellipsoidal gold nanoparticles, which significantly improved the responsivity of the detector in the visible light band. When the incident light wavelength was 500 nm, AuNPs/Gr/Si have the maximum enhancement, the responsivity increased by 48% (from 0.15 A/W to 0.22 A/W). The Au NPs fabricated by electron beam lithography are neat gold nanodisk arrays. When the incident light wavelength was 630 nm, the responsivity increased by 61% (from 0.23 A/W to 0.37 A/W). At the same time, the on-off ratio, detectivity, noise equivalent power and other performance indexes of the detector also significantly improved.

4. Two-step hot-embossing method was proposed to directly transfer of graphene and fabricate of Gr/Si Schottky photodetector. At present, the most commonly used graphene transfer method is using a temporary support layer like PMMA, but it requires experienced manual operation, which is not applicable for mass production, besides PMMA residue usually leads to degradation of device

performance. Two-step hot-embossing method was carried out without the assistance of PMMA temporary support layer. Graphene was directly transferred to COC film substrate by hot-embossing process, and then COC/graphene structure was embossed with prefabricated substrate by using hot-embossing process again to form Gr/Si Schottky photodetector. The Raman spectra of graphene films before and after hot-embossing showed that the structure of graphene remained intact after undergoing the molding pressure of 25 MPa. The photoelectric response showed that the responsivity reached 0.73 A/W under 633 nm illumination.

Acknowledgment

I would like to thank my supervisor Prof. Shuming Yang for the meticulous guidance, invaluable advice and continuous support from the determination of theme to the thesis writing. I would also like to thank my co-supervisor Prof. Fabrizio Candido Pirri for his help during my study in Italy. I would like to thank all the members in Prof. Shuming Yang's group and Prof. Fabrizio Candido Pirri's group for their kindly help in both study and life. Finally, I would like to express my gratitude to my family and friends for their encouragement and support all through my studies.

Contents

List of Tables

List of Figures

Chapter 1

Introduction

1.1 Background

Photodetector is a medium to convert optical signal into electrical signal, which is widely used in daily life, industrial production, national defence, aerospace and other fields [1-5]. At present, the development of photodetectors is relatively mature, various photodetectors based on GaN, Si, InGaAs, HgCdTe and other different band gap semiconductor materials have been able to cover the entire application band from ultraviolet to infrared [6-10]. In particular, benefitting from the mature silicon micromachining technology, photodetectors based on Si, the first generation semiconductor material, can be well compatible with the industrial production process [11-12]. Based on the working principles, semiconductor photodetectors can be divided into photoconductive type and photovoltaic type [13-14]. In photoconductive detector, the uniform semiconductor absorbs the incident photons and generates extra free electrons and free holes, which changes the conductivity of the semiconductor. The photoconductive effect can be used to fabricate various kinds of optoelectronic devices, including photoresistors, photocells, etc. In photovoltaic detector, the semiconductor p-n junction or Schottky junction absorbs the incident photons. The photogenerated holes in the valence band and the photogenerated electrons in the conduction band are separated by built-in electric field, resulting in photovoltage or photocurrent. This type of photodetector includes photodiodes, photosensitive transistors, etc.

Semiconductor photodetectors, due to their advantages of small size, low power consumption, fast response speed, high sensitivity and easy integration with other semiconductor devices, are widely used in optical communication, signal processing, sensing system and measurement system, which plays an important role in promoting social development and will continue to occupy the major market of photodetectors for a long time. However, the traditional semiconductor optoelectronic materials are facing many problems, which limits their further large-scale application and development. The doping concentration of

impurities in the monoatomic semiconductor is often limited by the solid solubility of the material itself, while the control of the element types and contents in the multi-component semiconductor is complex. In addition, some semiconductors used for photodetection, such as InGaAs and HgCdTe, are synthesized by molecular beam epitaxy or metal organic chemical vapor deposition with toxic source materials, the complex process and high cost limit the application and development of traditional semiconductor materials.

Graphene is a two-dimensional material composed of a single layer of carbon atoms. Owing to high carrier mobility, stable absorption in wide spectrum, high strength and toughness, graphene was considered to be an ideal material for optoelectronic devices [15-18]. Since the first graphene photodetector was fabricated using mechanical exfoliated graphene by Xia in 2009 [19], graphene photodetectors developed rapidly in the following decade. At the early stage, graphene photodetectors were mainly based on the metal-graphene-metal (MGM) structure [20-24]. This structure makes best use of the high carrier mobility and wide spectral absorption of graphene. The theoretical bandwidth is as high as 500 GHz, and bandwidth in actual test reaches 40GHz under the influence of circuit capacitance [19]. Meanwhile, it also has a wide spectrum detection capability from ultraviolet to infrared, even terahertz [25]. However, the recombination of photogenerated carriers is too fast due to the zero band gap structure of graphene, which makes it difficult to separate them effectively. Moreover, the interaction distance between graphene and incident light is limited by the monoatomic thickness of graphene, which leads to the low optical absorption coefficient (~2.3%) and limits the photoelectric response of the detector. Although some ingenious methods have been proposed to solve this problem, such as combining with optical waveguide [26], reflective microcavity [27], quantum dots [28], etc. To a certain extent these methods can improve the weak interaction between graphene and light, but they also bring new problems such as complex structure and process, limited response speed and so on.

Recently, graphene semiconductor heterojunction photodetectors, as another important part of graphene based photodetectors, have attracted more attention [29-31]. As early as 2010, Li Xinming [32] has proposed the graphene/silicon Schottky junction photodetection structure. The construction of Schottky junction can be realized by simply transferring graphene to silicon substrate.Due to the rectifying behavior of Schottky junction, when the detector works under reverse bias, the dark current is quite small, which makes the on-off ratio much higher than that of metal contact graphene photodetector. Meanwhile, compared with the traditional silicon-based photodetectors, the manufacturing process of graphene/silicon photodetector is simple. There is no need for high-temperature diffusion bonding process during the fabrication. Graphene/silicon Schottky junction photodetectors not only have simple structure and good performance, but also can be modified by various means, including surface modification and interface intercalation. In this context, it is of great significance to carry out the research on graphene/silicon Schottky junction photodetectors and optimize their structure and performance.

1.2 Overview of graphene

1.2.1 Structure and properties of graphene

Graphene was first obtained by mechanical stripping in 2004 [33]. The discovery of graphene formed a complete system of carbon material from zero dimensional fullerene, one-dimensional carbon nanotubes, two-dimensional graphene to three-dimensional graphite and diamond. As shown in Figure 1-1, graphene is the basic unit of other carbon materials: it can be warped into zero dimensional fullerenes, curled to form one-dimensional carbon nanotubes, or stacked to form three-dimensional graphite [34].

In graphene, all carbon atoms are sp2 hybrid, and each carbon atom forms strong covalent bonds with three adjacent carbon atoms. Therefore, each carbon atom can contribute a non-bonding electron which can move freely in the structure to form a π-bond on the graphene plane. This special crystal structure makes graphene have unique band structure. The conduction band and valence band of intrinsic graphene are cones symmetrical about Dirac point, and intersect at Fermi level [35-38], as shown in Figure 1-2, thus electrons and holes in graphene have the same properties. In general semiconductors, the electron is considered to be a particle with a certain effective mass and obeys Newton's law of motion, and its quantum mechanical behavior conforms to the Schrodinger equation. Different from the parabolic dispersion relation of conventional semiconductors, the low-energy electrons in graphene exhibit linear dispersion relation, and their quantum mechanical behavior is more in line with Dirac equation, which indicates that graphene electron is a relativistic particle which can ignore its own mass [39].

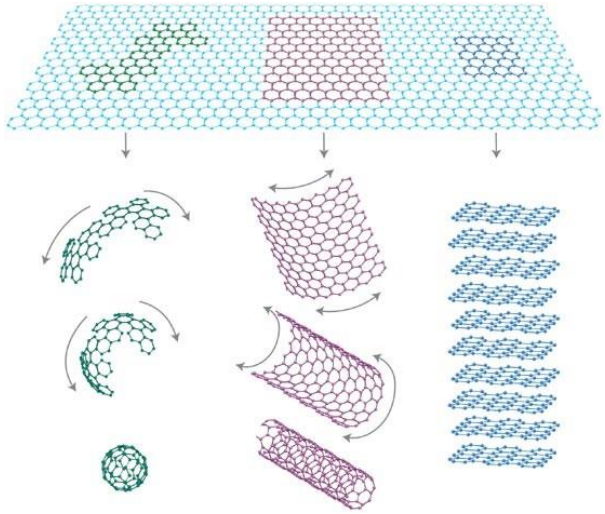

Figure 1-1 Graphene is a 2D building material for carbon materials of all other dimensionalities [34]

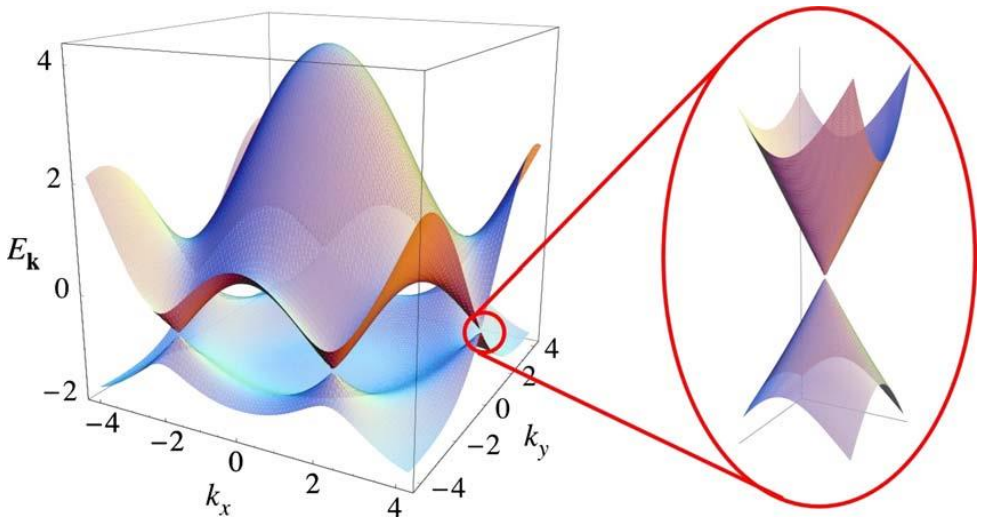

Figure 1-2 Energy band structure of graphene [33]

The effect of phonon scattering on the transmission of electrons in graphene plane is very small, thus the carrier mobility of graphene can reach as high as $2\times10^5 cm^2\cdot V^{-1}\cdot s^{-1}$ at room temperature, the carrier concentration of graphene is up to 10^{13} cm^{-2}, and the resistivity is only 10^{-6} Ω· cm [16, 40]. Graphene has stable optical absorption properties in the wide spectral range from UV to IR, and its absorption ratio is only related to the fine structure constant α [17], but not to the wavelength of incident light. Theoretically, the absorption ratio of single-layer graphene to vertical incident light is 2.3% [39]. In addition, graphene also has many excellent physical and chemical properties, its strength up to 130 GPa [18], thermal conductivity as high as $5300 W\cdot m^{-1}\cdot K^{-1}$ [40]. Due to its unique structure and excellent properties, graphene has attracted extensive attention in the fields of sensors, supercapacitors, high frequency circuits, and flexible devices.

1.2.2 Synthesis of graphene

Graphene was first obtained by micromechanical exfoliation [33]. Before that, researchers have fabricated zero-dimensional fullerenes, one-dimensional carbon nanotubes and three-dimensional graphite. These carbon based materials have their own unique properties, but the fabrication of two-dimensional carbon materials has been unachievable for a long time [50]. Graphite is a three-dimensional material formed by stacking many carbon atom layers, in which the layers are bonded by van der Waals force, a relatively weak interaction force. Geim et al. [33] used tape to peel off the highly oriented pyrolytic graphite layer by layer until a single layer of carbon atom film was obtained, which is known as graphene. The graphene fabricated by this method has good lattice structure and electrical properties, but micromechanical exfoliation is less efficient, and the size of the obtained graphene flake is relatively small, usually tens of microns. Therefore, it is suitable for scientific research in laboratory, but inapplicable to large-scale application. In this context, various methods of graphene synthesis have been explored, which can be divided into two categories: bottom-up growth method and top-down decomposition method. The former includes chemical

vapor deposition (CVD) and epitaxial growth, and the latter includes micromechanical exfoliation, oxidation-reduction method, etc. From the situation of their development in recent years, oxidation-reduction and chemical vapor deposition are the most promising methods.

The oxidation-reduction method is to oxidize graphite with strong oxidant, so that the hydroxyl group, carboxyl group and other oxygen-containing groups are inserted between the graphite layers, which increases the spacing of carbon atom layers and decreases the van der Waals force between the layers. Then subsequent ultrasonic treatment will separate the layers and obtain graphene oxide [51], as shown in Fig. 1-3. Finally, graphene can be obtained by reducing graphene oxide, chemically or thermally. This method does not need high temperature or vacuum conditions, the cost is lower than other methods, and the whole reaction process is carried out in solution, which is suitable for large-scale synthesis. However, strictly speaking, the graphene obtained by oxidation-reduction method should be called as reduced graphene oxide (rGO), which contains a large number of defects and residual functional groups, and its size after ultrasonic treatment is generally small. Because of the above drawbacks of oxidation-reduction method, reduced graphene oxide is widely used in composite materials, but its application in the field of high-performance electronic devices is limited.

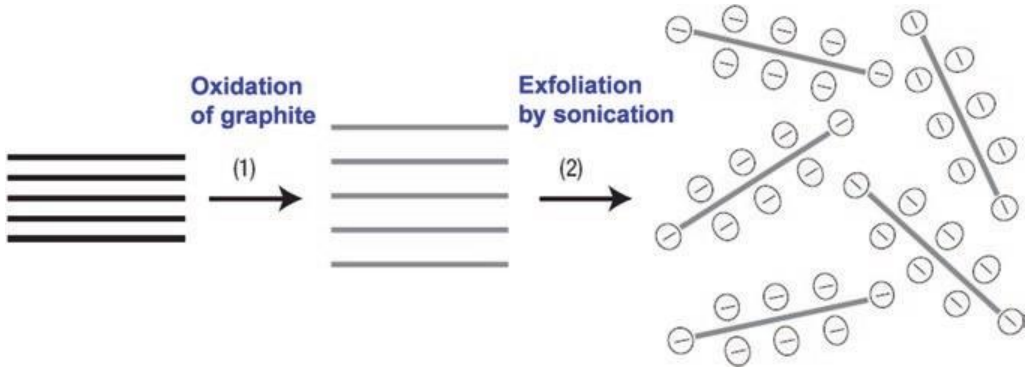

Figure 1-3 Schematic diagram of fabrication process of graphene oxide [51]

In CVD method, carbon source molecules decompose into carbon atoms at high temperature and form graphene films on the substrate. As early as the 1960s, there were studies on the growth of carbon thin films on metal substrates by CVD, but the purpose of the research at that time was to avoid the formation of graphite structure on metal catalysts such as Pt, so as to avoid the degradation of catalytic activity [52, 53]. Subsequently, Blakely et al. analyzed the carbon segregation on Pt, Pd, Co and other metal surfaces in the 1970s, and focused on the "single-layer carbon film" grown on Ni Substrate [54, 55]. With the global upsurge caused by the discovery of graphene, this method has attracted extensive attention and has been tried to grow graphene films. The follow-up studies show that Ni, Co, Pt, Ru, Cu and many other metal materials can be used as substrates for CVD growth of graphene, among which Ni and Cu are the most widely used. However, the growth mechanism of graphene on different metal substrates is different [56]. As shown in Fig. 1-4, the growth of graphene on Ni substrate is mainly based on the mechanism of carbon bulk diffusion. Due to the relatively high carbon solubility

of Ni, the carbon atoms generated by carbon source decomposition diffuse into Ni substrate at high temperature, and form graphene on the surface during the cooling step; as for Cu substrate, the growth of graphene is mainly based on the surface migration mechanism. Due to the low carbon solubility of Cu, the carbon atoms generated by the decomposition of carbon source at high temperature directly adsorb on the surface of Cu substrate, nucleate and form graphene films.

There are many kinds of carbon sources for the synthesis of graphene by CVD. The gaseous carbon sources are most commonly used, including methane, ethane [57], acetylene [58], etc., and there are also solid and liquid carbon sources such as polystyrene [59], toluene [60], ethanol [61]. Different kinds of carbon sources have different effects on the growth of graphene. For example, the hydrocarbon bond of polystyrene is relatively weak, which makes polystyrene has a lower decomposition temperature. Ethanol as a carbon source at high temperature will produce oxides and etch amorphous carbon. Ethylene has more stable carbon-carbon double bond structure, so it is more difficult to crack and rearrange. Methane is more pure and has lower dehydrogenation energy, which is better for the quality of graphene.

In addition, the growth of graphene will be influenced by CVD process parameters, such as gas flow rate, growth temperature, gas pressure, growing time, cooling rate, etc. [62]. In order to obtain large area and high quality graphene films, the CVD process parameters need to be well optimized. In the CVD synthesis of graphene, argon is usually used as carrier gas, and a certain amount of hydrogen is introduced into it. The existence of hydrogen can remove the oxidation pollution on the surface of metal substrate and etch the weak carbon-carbon bond, which can remove the amorphous carbon produced in the growth process; but it also etches graphene at the same time, destroys the crystal lattice and leads to more defects in graphene. Higher temperature can activate the reaction gas, enhance the catalytic ability of the substrate, and promote the movement of carbon atoms on the surface of the substrate, so that the quality of graphene is higher, the defects and multilayer regions in graphene are reduced. The gas pressure influences the average free path of carbon atoms. When the growth pressure is low, the carbon atoms have a good arrangement, so it is easy to obtain high-quality graphene. With the growth pressure gradually increasing, the average free path of carbon atoms gradually decreases, the carbon atoms consume a lot of energy in the continuous collision. When they reach the substrate surface, their ability of rearrangement is decreased due to their low energy, so it is easy to form irregular graphene. Similarly, the choice of growth time is also important for the growth of graphene. When the growth time is too short, graphene is still in the initial stage of nucleation and growth, only small-size island-like graphene microcrystals can be obtained, which have not grown to form continuous graphene film. However, long growth time will lead to a large number of carbon atoms, forming multilayer graphene and even graphite thin membrane.

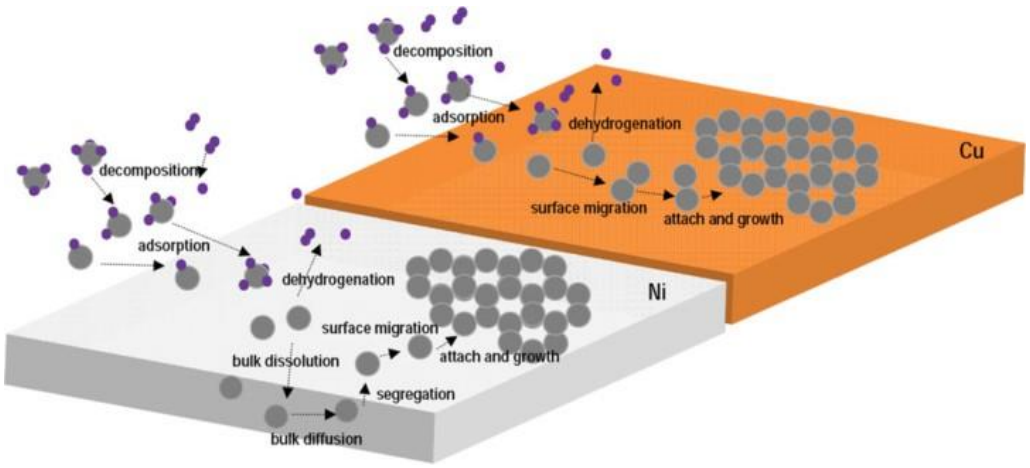

Figure 1-4 Growth mechanism of CVD graphene on Ni and Cu Substrate[56]

Deokar et al. has obtained high-quality graphene on copper foil substrate by optimizing CVD growth process parameters [63]. By using the fast annealing furnace, the cooling time of CVD is greatly reduced, and the whole growth process is controlled within 30 minutes. Moreover, by adjusting the growth temperature and gas flow ratio, the catalytic effect and etching effect of hydrogen was well balanced, and the proportion of multi-layer region in graphene film is significantly reduced. As shown in Fig. 1-5, the growth temperature of Fig. (a) is 1070 ℃, and the gas flow rate of $Ar/CH_4/H_2$ is 10/2/1 sccm. When the growth temperature is reduced to 1060 ℃, the multilayer region is obviously reduced, but still exists, as shown in Fig. (b); while further reducing the hydrogen flow rate, a large area of single-layer graphene film can be obtained, with almost no multilayer region, as shown in Fig. (c).

Due to the nucleation growth mechanism of graphene synthesized by CVD, when the carbon islands grow and finally form a continuous graphene film, there is obvious boundaries in graphene, called grain boundary. The lattice dislocation at the grain boundary will hinder the carrier transport in graphene, which is the main reason why the quality of CVD graphene is inferior to that of mechanically exfoliated graphene. Mohsin et al. [64] first melted the copper foil substrate and then solidified it again to reduce the defect density on the surface, thus reducing the nucleation density of graphene. Single crystal hexagonal graphene with millimeter size was obtained by this method, as shown in Fig. 1-6.

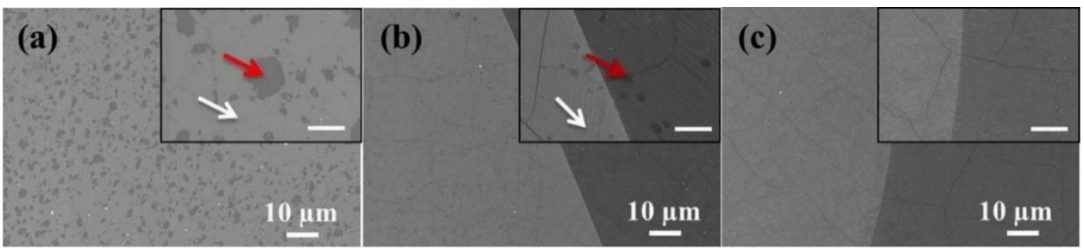

Figure 1-5 Optimization of the parameters for CVD growth of graphene [63]

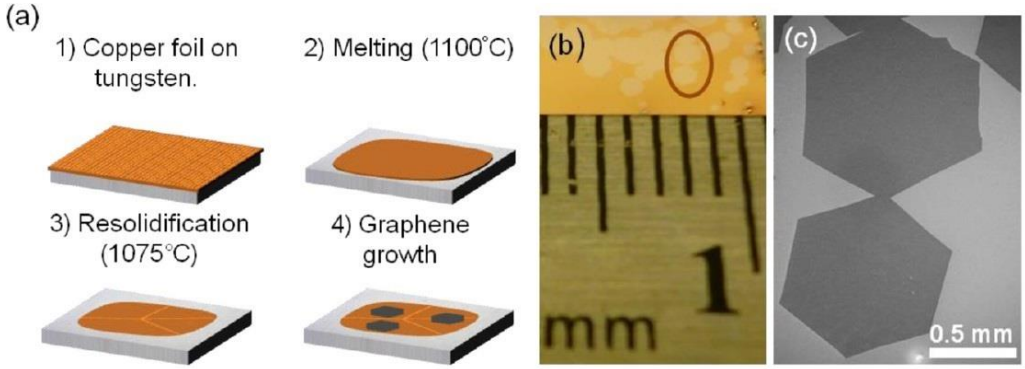

Figure 1-6 Single crystal hexagonal graphene with millimeter size grown on solidified Cu foil [64]

Although there have been many attempts to directly grow graphene on insulating substrate by CVD method [65], there is still a significant gap in crystal quality and continuity compared with graphene grown on metal substrate. Therefore, CVD graphene should be transferred from metal substrate to insulating substrate to fabricate electronic devices [66-69]. The most commonly used graphene transfer method is to coat graphene/metal with temporary support layer, such as polymethylmethacrylate (PMMA), then etch away the metal substrate, transfer graphene together with temporary support layer to target substrate, and finally remove temporary support layer with appropriate solvent [70], as shown in Fig. 1-7. However, this simple and easy transfer method has many problems: the graphene is easy to be damaged and wrinkled during the transfer process; the etchant will cause ion residue; the surface residue caused by the temporary support layer material cannot be completely removed [71].

For the structural damage of graphene caused by transfer process, Li et al. [72] found that the surface of metal substrate recrystallized at high temperature is no longer smooth, which will influence the graphene conformally grown on the substrate and the temporary support layer coated on the substrate. Therefore, when the graphene was transferred to the flat target substrate, there will be a gap between them. In this regard, they proposed a method of redepositing PMMA on the PMMA/graphene to release the internal stress by partially or completely dissolving the PMMA temporary support layer which has been completely cured, so that the graphene attached to the target substrate can form better contact with the flat surface. The water between graphene and the target substrate is also considered to be one of the causes of wrinkles. Using of a target substrate with good hydrophilicity and thermal drying is conducive to the diffusion and evaporation of water [73], and using volatile liquid with lower surface tension (such as heptane) to replace water [74] also helps to improve the graphene transfer process.

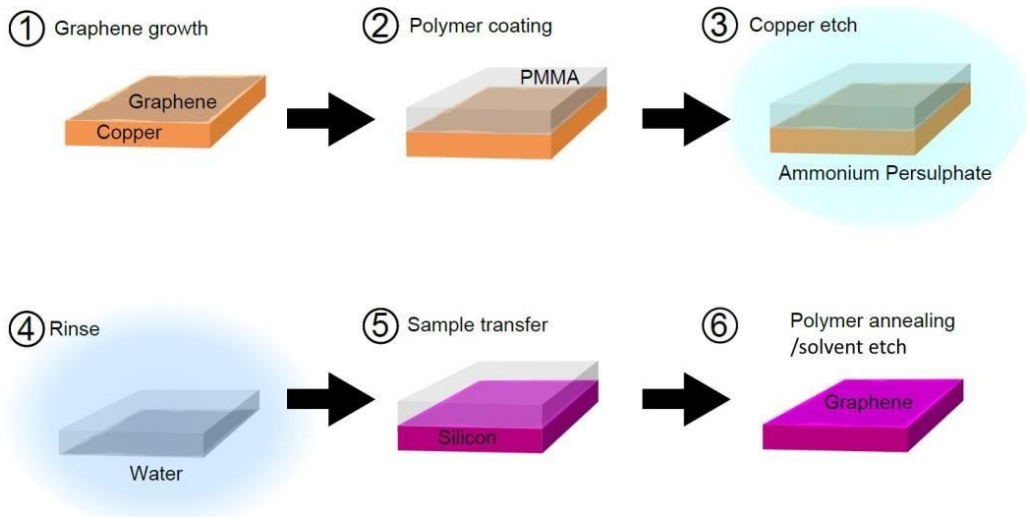

Figure 1-7 The graphene transfer process with temporary support layer [70]

Since $FeCl_3$ solution is the most frequently used etchant of metal substrate, the obtained PMMA/graphene laminated structure always shows pale yellow because a small amount of etchant will remain on the surface of graphene, showing light yellow color. Although the graphene can be rinsed to be transparent by deionized water, the residual metal iron ions can not be removed completely. The use of ammonium persulfate ($(NH_4)_2S_2O_8$) instead of $FeCl_3$ as the etchant of metal substrate can reduce the surface pollution caused by the transfer process [63,75]. The improved RCA cleaning method can further remove the residual etchant on graphene surface, and solve the problem of insufficient etching of metal substrate [73].

There are many kinds of materials that can be used as temporary support layer, including PMMA, epoxy resin and even metal, among them PMMA is the most widely used. As a temporary support layer, PMMA is difficult to be completely removed, which is the most serious problem in traditional graphene transfer methods and will greatly affect the performance of graphene. The surface residue of graphene will become the scattering center and degrade the carrier transport performance, which will affect the electronic devices based on graphene. Generally, PMMA can not be completely remove by acetone immersion. Michael et al. [76] used acetic acid instead of acetone to obtain cleaner graphene. Lin et al. [77] promoted the separation of different functional groups adsorbed on graphene surface by low-temperature annealing in air and in argon hydrogen mixed atmosphere. Suhail et al. [78] reduced the PMMA residue on graphene surface by deep ultraviolet irradiation. Although these methods can reduce the residual of temporary support layer materials on graphene surface to a certain extent, they increase the process complexity of graphene transfer at the same time. Therefore, the transfer methods without temporary support layer have attracted the attention of relevant researchers. Lin et al. [79] realized the direct transfer of CVD graphene film with the aid of carbon mesh. Zhang et al. [80] placed graphene at the interface of hexane and etchant aqueous solution, graphene was supported by the surface tension of two immiscible liquids, as shown in Fig. 1-8. Although these methods can avoid the pollution of temporary support layer materials on graphene and

obtain graphene with cleaner surface, the lack of stable support will make the structure of graphene more vulnerable to damage, which increases the difficulty of transfer process.

In conclusion, CVD method can realize the growth of graphene with large area and high quality, but the growth parameters need to be accurately controlled and optimized. Chapter 2 introduces the experimental details of monolayer graphene growth on copper foil substrate by CVD with methane as carbon source and hydrogen as dilution gas. Chapter 5 proposes a new method of directly transferring CVD graphene and fabricating graphene/silicon Schottky junction photodetectors by two-step hot-embossing.

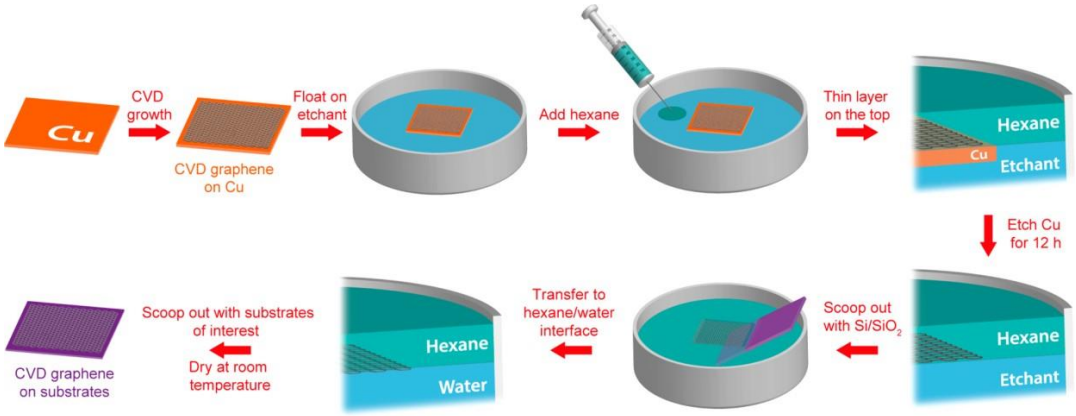

Figure 1-8 The graphene transfer process without temporary support layer [80]

1.3 Overview of graphene photodetectors

1.3.1 Metal contact graphene photodetectors

The first graphene photodetector fabricated by Xia et al. in 2009 is metal-graphene-metal structure [19], which is also the simplest graphene photodetector structure so far. In this structure, graphene contacts with metal electrodes (source and drain) to form detector structure, as shown in Fig. 1-9, the channel width is 0.62 μm and the channel length is 1.45 μm. In graphene metal contact, due to the different work functions of graphene and metal, the Fermi level of graphene in the contact region bends and gradually recovers with the increase of distance away from the contact area [24]. This will lead to the electric potential gradient in the range of 100 ~ 200 nm near the metal contact area, and form the built-in electric field. When graphene absorbs the incident light and excites the photogenerated electron-hole pairs, the photogenerated electrons and holes will be separated by the built-in electric field. When the external circuit is open, the detector outputs optical voltage signal; when the external circuit is closed, the detector outputs photocurrent signal. Due to the very high electron saturation velocity of graphene, the detector is able to realize ultrafast photoelectric detection up to 40 GHz, and its intrinsic bandwidth was expected to reach 500 GHz. However, the responsivity of the detector is only 0.5 mA/W due to the low optical absorptivity of graphene.

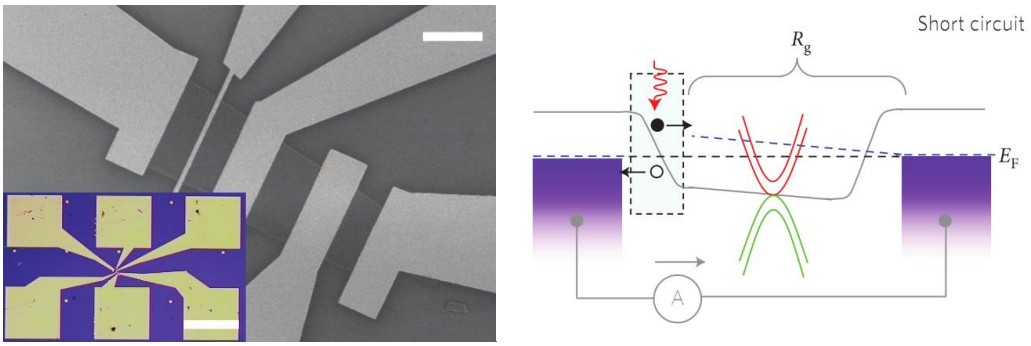

Figure 1-9 The first graphene photodetector. (a) SEM and optical (inset) images of the photodetector. (b) Potential profile of the photodetector. [19]

It should be noted that, in the photodetector shown in Fig. 9, the built-in potentials generated by metal contact on two sides have opposite direction, and the photoelectric signals generated by them will cancel each other and weaken the performance of the detector. To solve this problem, Mueller et al. [22] used two different metal materials as the source and drain electrodes to form an asymmetric potential distribution. The built-in potentials generated by metal contact on both sides have the same direction, and the generated photocurrent by them are enhanced instead of canceling each other, thus improving the photoelectric response of the detector.

At the same time, interdigitated metal fingers are used to increase the metal contact area, as shown in Fig. 1-10. The built-in electric fields only exist near the metal contact interfaces with a width of 100 ~ 200nm, and the photo carriers generated by the incident light in other regions recombine rapidly due to the absence of built-in potential, which does not contribute to the photocurrent of the detector. The interdigitated electrode structure provides a lager light-detection region and increases the detector's responsivity to 6.1 mA/W. Due to relatively large circuit capacitance, the 3dB bandwidth of this photodetector is 16 GHz. When it is applied to the actual 10 Gbps optical data transmission test, a clear eye diagram can be obtained.

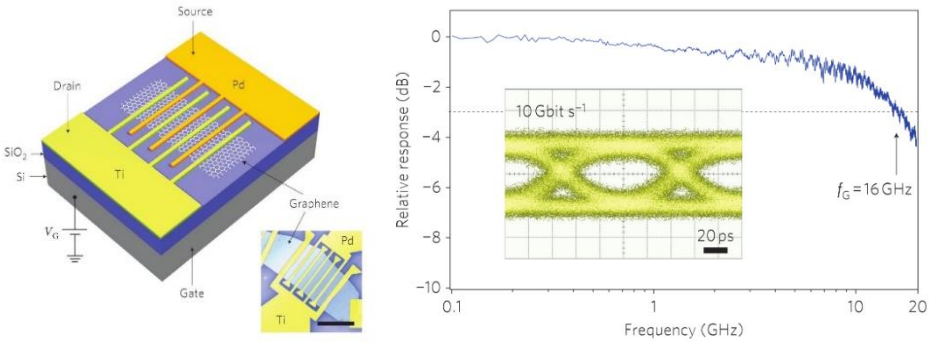

Figure 1-10 Metal–graphene–metal photodetectors with interdigitated metal fingers and asymmetric metal contacts. (a) Photodetector schematics. (b) Relative photoresponse versus light intensity modulation frequency [22]

Because graphene is a single atomic layer, the interaction distance between graphene and the incident light is very short, thus the optical absorption coefficient is only 2.3%, which greatly limits the photoelectric response of the

detector. Surface plasmon polaritons (SPPs) are an electromagnetic excitation existing on the surface of a good metal. By coupling sub-wavelength metallic nanostructures to graphene surface, the local surface plasmon can enhance the intensity of local near-field light field and improve the light absorption efficiency of graphene [81-83], as shown in Fig. 1-11, changing the configuration (shape, size, thickness, etc.) of nanostructures can also realize wavelength selective photodetection.

In 2011, Liu et al. [84] coupled gold nanoparticles with graphene to achieve efficient plasmon resonance enhanced photodetection, as shown in Fig. 1-12. By using the local surface plasmon enhanced effect of gold nanostructures, the device can obtain an external quantum efficiency of up to 1500%, increase the responsivity of the detector to 6.1 mA/W, and realize wavelength selective detection. It demonstrated the feasibility of improving the performance of graphene photodetectors by using the surface plasmon near-field enhancement effect of metal nanoparticles.

Furchi et al. [27] proposed a more direct method to increase the light absorption of graphene. As shown in Fig. 1-13, multilayer Bragg reflectors are arranged above and below the graphene photodetector to form a Fabry Perot reflection microcavity. The incident light is reflected back and forth in the microcavity and passes through the graphene film in the center of the microcavity for many times. The reflective microcavity has a specific resonance wavelength, which is determined by its geometry and the material of the reflector. When the incident light wavelength is close to the resonance wavelength, the enhancement effect of the reflection microcavity is stronger, which makes the photodetector show obvious wavelength selectivity. For the incident light with wavelength of 850 nm, the light absorption rate of the microcavity enhanced graphene photodetector can reach 60%, and the responsivity of the graphene photodetector reaches 21 mA/W.

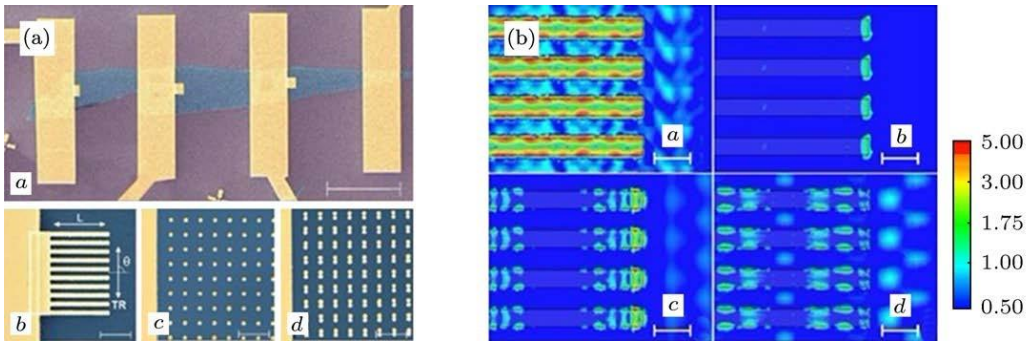

Figure 1-11 Plasmonic enhancement of graphene by sub-wavelength metallic nanostructures. (a) SEM micrograph of contacts with various plasmonic nanostructures. (b) Numerical finite difference time domain simulations for different excitation wavelengths and polarizations [81]

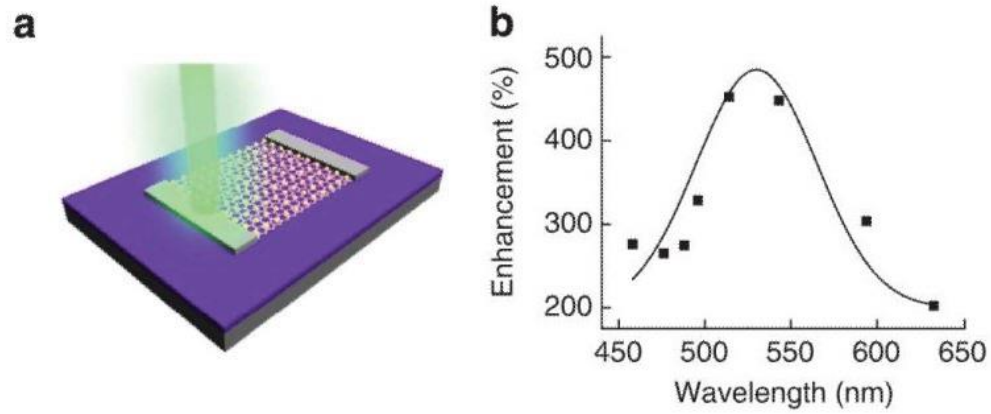

Figure 1-12 Graphene photodetector coupled with gold nanoparticles. (a) Photodetector schematics. (b) Photocurrent enhancement as a function of laser wavelength. [84]

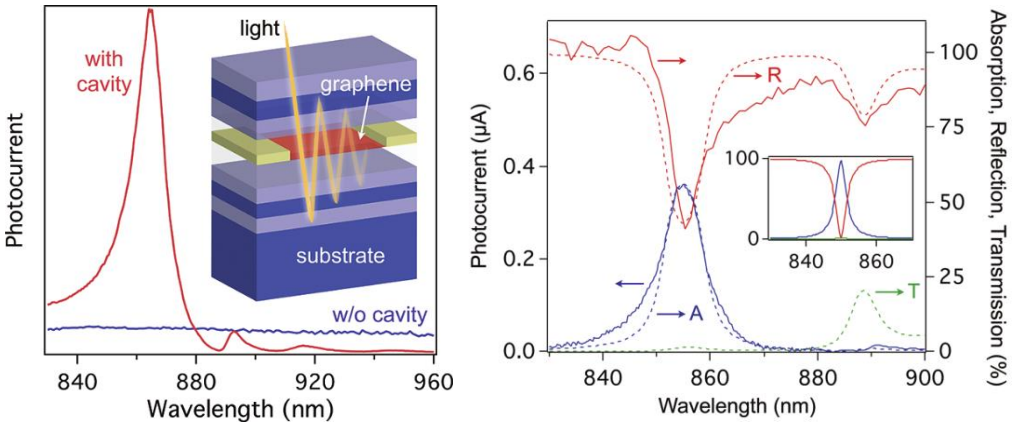

Figure 1-13 Graphene photodetector coupled with microcavity. (a) Photodetector schematics. (b) Spectral response of the photodetector. [27]

The optical waveguide integrated on chip can increase the light absorptivity by controlling the optical transmission mode, thus improving the performance of photodetectors. Wang et al. [26] designed the graphene photodetector combined with silicon waveguide, as shown in Fig. 1-14, the silicon waveguide was fabricated on the silicon on insulator (SOI) substrate. The silicon oxide layer under the waveguide was removed by wet etching, and the suspended silicon waveguide was obtained to reduce the transmission loss of light in the waveguide. Graphene was placed on the surface of the silicon waveguide, and the metal electrodes were deposited fabricate photodetector. When the light transmits in the waveguide by total reflection, the evanescent wave will be generated near the surface of the waveguide and absorbed by graphene, which changes the output current of the photodetector and realizes detection to the incident light. Because the propagation direction of the evanescent wave is parallel to the waveguide plane, the interaction distance between the evanescent wave and graphene is longer than that of the normal incident light. The photoelectric responsivity of 0.13 A/W can be obtained by this method.

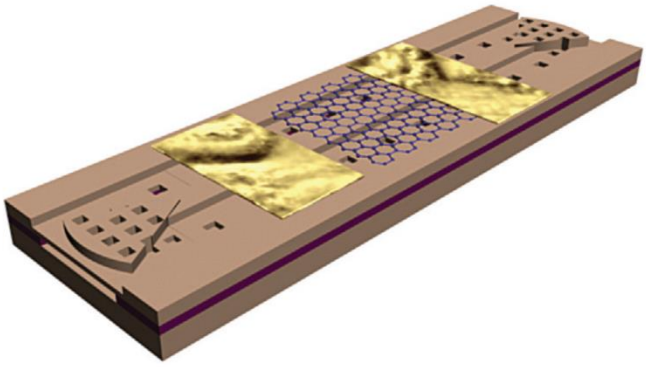

Figure 1-14 Graphene photodetector integrated with optical waveguide [26]

In addition, the combination of semiconductor quantum dots is also an effective method to increase the responsivity of graphene photodetector [85]. Gerasimos et al. [28] designed a graphene photodetector modified by PbS quantum dots, as shown in Fig. 1-15, the incident light was absorbed by the PbS quantum dots, the photogenerated electrons were trapped in quantum dots, and the photogenerated holes were injected into graphene, which reduced the recombination of photogenerated carriers and increased the lifetime of photogenerated carriers. Benefitting from the high carrier mobility of graphene, photogenerated carriers can pass through the circuit many times before recombination, which makes the photodetector have a large photocurrent gain. With this method, the responsivity of graphene photodetectors can reach as high as 10^7 A/W, which has significant advantages for the detection of weak optical signals, but there are also many shortcomings. When the incident light power increases, the photocurrent will be saturated rapidly. Moreover, the dark current of the detector is large and cannot be turned off effectively, resulting in the increase of power consumption, which is not suitable for large-scale integration and imaging equipment. The switch ratio of the device is less than 1, which makes it difficult to be applied to optical switch. The response speed of the detector is greatly limited due to the binding of quantum dots to photo generated carriers.

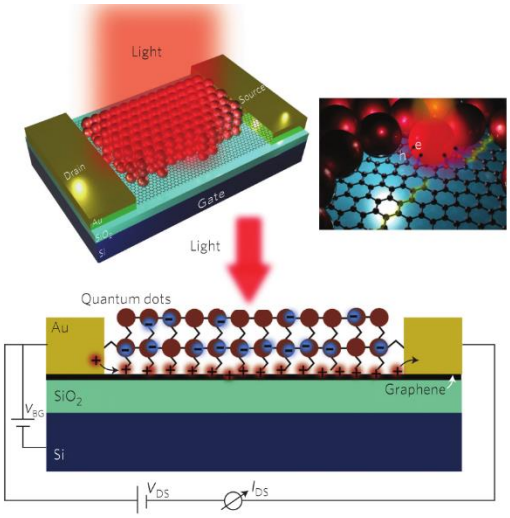

Figure 1-15 Graphene photodetector combined with quantum dots [28]

In conclusion, the graphene detector based on metal contact can make good use of the advantages of high carrier mobility of graphene to realize high-speed

optical detection. However, due to the low optical absorptivity of graphene, the responsivity of the graphene photodetector is generally low. There has been some improvements, such as increasing the times of light passing through graphene, increasing the interaction distance of light and graphene, and even using modified materials instead of graphene to absorb radiation. By these methods, the responsivity of the detector can be improved to a certain extent, but they also increase the structural complexity and manufacturing difficulty, and the response speed of the detector is degraded. Moreover, the graphene detector based on metal contact is a junction free photodetector, the dark current is generally large under a bias voltage, which lowers the on/off ratio and increases the power consumption of the detector [26].

1.3.2 Graphene/silicon Schottky junction photodetectors

When graphene contacts with silicon, germanium, gallium nitride and other semiconductor materials, due to their different work functions, carriers in the contact region redistribute and form Schottky junction. Silicon, as the first generation semiconductor material, has a complete set of mature processing and manufacturing processes, rich reserves and stable performance. It is the most widely used semiconductor material in the world. At present, the vast majority of optoelectronic devices are still silicon-based devices [86]. The combination of graphene with unique photoelectric properties and silicon with mature process foundation has attracted a large number of scholars' research interest, graphene/silicon Schottky junction can be used in photodetectors [21, 26, 87-94], solar cells [32, 95-100], diodes [101-103], and sensors [104-107]. Both photodetector and solar cell absorb radiation energy and convert them into electrical output, they have many similarities in research contents and methods, only the performance parameters concerned are different. For photodetectors, researchers pay more attention to the parameters such as responsivity and detectivity; for solar cells, photoelectric conversion efficiency is more important. In the actual research process, they are often linked together, many research groups have carried out research on both sides at the same time. Zhu et al. even measured and analyzed the performance of graphene/silicon Schottky junction as photodetector and solar cell at the same time [93]. In addition, different from solar cells as energy conversion and output devices, the graphene/silicon Schottky junction photodetectors can reach a larger photoelectric response gain with suitable bias voltage. Due to the rectifying characteristics of Schottky junction, the dark current of graphene/silicon photodetectors is lower than that of metal contact photodetectors.

In 2010, Li Xinming et al. fabricated the first graphene/silicon Schottky junction solar cell [32] by simply transferring graphene to the SiO_2/Si substrate with pre-etched window, as shown in Fig. 1-16. The work function of graphene is about 4.8 eV ~ 5.0 eV, and the work function of n-type silicon substrate is about 4.25 eV. When graphene contacts with n-type silicon, electrons in silicon will enter graphene to form a new thermal equilibrium. At this time, the energy band

of silicon side will bend upward, forming the built-in potential from silicon to graphene. When the detector receives the incident light, the incident photons are mainly absorbed by silicon to excite electron hole pairs. With the built-in potential, photogenerated electrons and holes are pulled to silicon and graphene, respectively, thus generate photocurrent. Because this Gr/Si structure was originally designed as a solar cell, its photocurrent responsivity is only about 65 mA/W, which is not superior to the metal contact graphene detector.

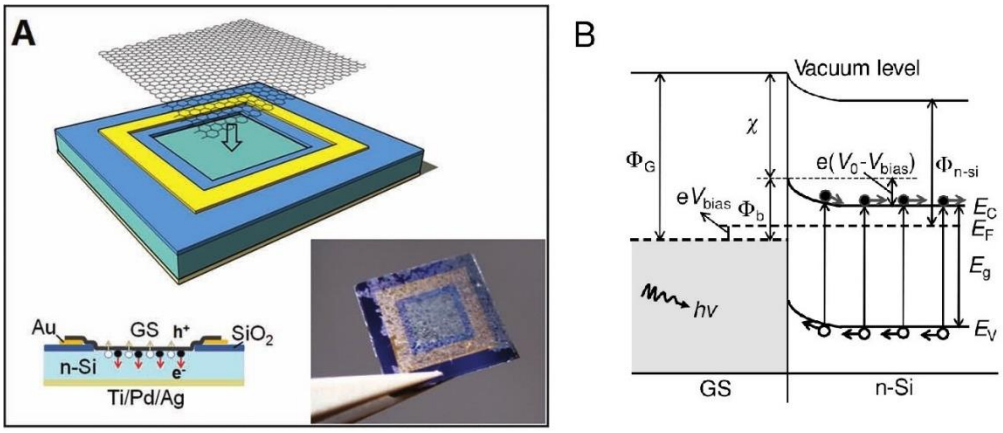

Figure 1-16 The first graphene/silicon Schottky photoelectric device. (a) Schematics of the device. (b) Band profile of the device. [32]

In 2013, An et al. [87] systematically studied the photoelectric detection performance of graphene/silicon Schottky junction, as shown in Fig. 1-17. As graphene only works as a transparent electrode and high-speed carrier transmission channel, the absorption of incident light is mainly carried out by silicon, so the spectral response range of the detector is limited by the silicon band gap. The spectral response measurement showed that the graphene/silicon Schottky junction photodetector responded from near ultraviolet to near infrared. The detector could work in two modes of photovoltage and photocurrent. It had low dark current and high photoelectric response, the noise equivalent power (NEP) reached 1 pW/Hz$^{1/2}$. At the same time, with a wide dynamic measurement range, it could effectively detect the incident light from picowatt level to milliwatt level. For the weak incident signal, the voltage responsivity of the detector was as high as 10^7 V/W, but it decreased rapidly with the increase of the incident light power. However, in photocurrent mode, the photoelectric response of the detector always kept good linearity for the incident light signal whose power dynamic range spans six orders of magnitude. By tunning the quasi Fermi level by bias voltage, the detector has a tunable responsivity, up to 435 mA/W at 850 nm. The response speed of the detector was limited by the carrier mobility of silicon, but it was still in the order of milliseconds. Considering its excellent weak signal detection ability and good linear photoelectric response, graphene/ silicon Schottky junction photodetectors have good application prospects in imaging devices, metering equipment and analytical instrument.

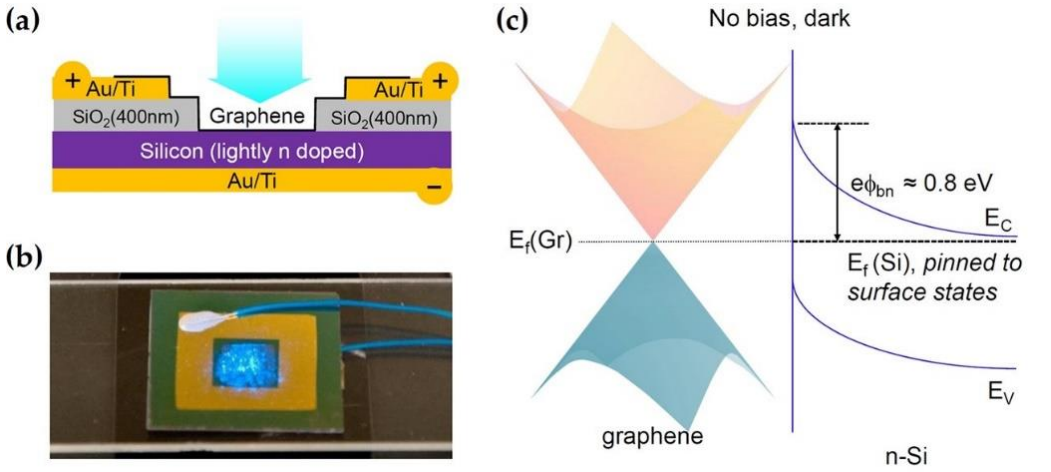

Figure 1-17 Graphene/silicon heterojunction for ultrasensitive photodetection [87]

As mentioned above, graphene/silicon Schottky junction photodetectors have significant advantages over metal contact graphene photodetectors in terms of responsivity, dark current and switching ratio, but there is still a certain gap compared with commercial silicon photodetectors. Therefore, it is necessary to continue to optimize the detector to improve its performance. The performance improvement methods of graphene/silicon Schottky junction photodetectors can be divided into three categories: the improvement of silicon structure, the optimization of graphene/silicon interface and the modification on graphene surface.

The surface of polished silicon substrate usually has nano or sub-nano roughness, the smooth silicon surface has high reflectivity in visible frequency range. In the production process of traditional crystalline silicon solar cells, the first process is silicon surface texturing, as shown in Figure 1-18 [108]. The pyramidal or pit like textured surface can be obtained by etching silicon with alkaline or acidic corrosive solution. The effective textured structure can make the incident light reflect and refract many times in silicon, thus improve the trapping effect of silicon wafer and its absorption for incident light, so as to improve the photoelectric conversion efficiency of crystalline silicon solar cells. However, this method is not suitable for graphene/silicon Schottky junction photodetectors. Monocrystalline silicon substrate is usually used to ensure the performance of graphene/silicon Schottky junction photodetectors. The anisotropic etching of monocrystalline silicon surface by alkaline etching solution will form micron scale tetrahedral pyramidal structure [109], and graphene is easy to be damaged when transferred to the surface.

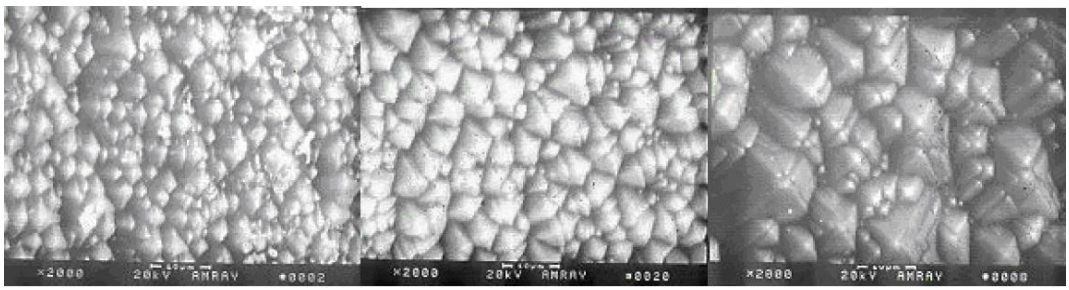

Figure 1-18 Surface texturing of silicon [109]

Although the surface with micro scale structure obtained by the traditional silicon texturing process is not suitable for graphene transfer, using this idea for reference, nano scale texturing treatment on silicon surface by appropriate methods could enhance the performance of graphene/silicon Schottky junction photodetectors [110-113]. In 2014, Kim et al. obtained high-density nano porous structure on silicon surface by metal assisted chemical etching method, which was used to enhance the response of graphene/silicon Schottky junction photodetector in ultraviolet range, as shown in Fig. 1-19. They first deposited a layer of silver nanoparticles on the surface of silicon substrate as a catalyst for chemical etching, and then used a mixture of hydrofluoric acid and hydrogen peroxide to etch the silicon surface. Due to the catalysis of silver, the silicon in contact with silver nanoparticles will be selectively etched. Finally, the porous silicon surface can be obtained by removing the silver nanoparticles with nitric acid. The density and depth of nanopores changed with etching time. When the etching time was 3 seconds, the transverse size of the nanopores obtained by this method was less than 10 nm, and the depth was about 20 nm. The porous silicon structure showed higher optical absorptivity and increased the band gap of silicon, which improved the responsivity and quantum efficiency of the detector in ultraviolet range. The detector had a peak quantum efficiency of 60% and the responsivity of about 0.2 A/W with the incident light wavelength of 400 nm ~ 500 nm. Similar to other Gr/Si detectors, the maximum photocurrent responsivity of about 0.35 A/W was obtained at 950 nm. It is worth mentioning that in 2017, the research group used the same method to prepare graphene/porous silicon solar cells [114], and continued to study the influence of graphene layer number and doping in 2018 [115, 116], which also reflects the close connection between the Gr/Si photodetectors and Gr/Si solar cells.

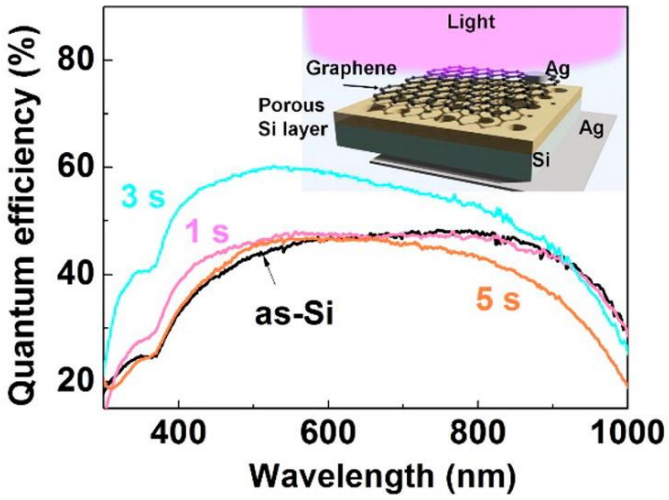

Figure 1-19 Graphene/Porous Silicon Photodetector [92]

Using silicon quantum dots (QDs) instead of bulk silicon to contact with graphene is another effective method to enhance the performance of Gr/Si photodetectors. Shin et al. [117] prepared graphene/silicon quantum dots photodetector, as shown in Fig. 1-20. The Si QDs with a band gap about 1.4 eV ~ 1.8 eV can effectively enhance the absorption of high energy photons. Moreover,

by adjusting the size of Si QDs, the photodetector can realize wavelength selective response. When the wavelength of incident light was 600 nm, the photo detector reached maximum responsivity of 0.35 A/W. With near ultraviolet incident light of 400 nm, the responsivity decreased due to the less light absorption, but was still higher than 0.1 A/W. Because of the short lifetime of photogenerated carriers excited in silicon quantum dots, the response time of the detector was shortened to ~10 μs, which was obviously superior to that of the conventional Gr/Si photodetectors.

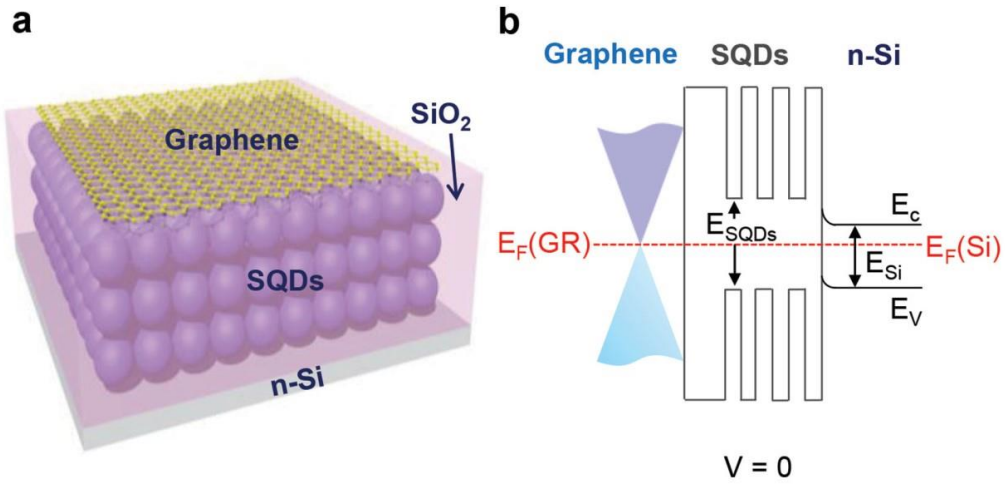

Figure 1-20 Graphene/Si-Quantum-Dot Photodetector. (a) Photodetector schematics. (b) Band diagram of the photodetector [117]

Antonio et al. [118, 119] fabricated the graphene/silicon nanotip photodetector, as shown in Fig. 1-21. The structure of silicon nanotip was beneficial to the absorption of incident light. With the decrease of the contact area, the electric field intensity at the tip of the silicon nanotip was enhanced, which also improved the separation effect of photogenerated carriers and internal gain. Compared with the traditional Gr/Si photodetectors, the current responsivity of the device was improved by an order of magnitude, reaching 3 A/W. The numerical simulation results showed that the nanotip greatly enhanced the intensity of the local electric field, which modulated the Fermi level of graphene, and the change of graphene Fermi level further affected the barrier height of Schottky junction. Therefore, the dark current of graphene/silicon nanotip photodetectors is higher than that of graphene/planar silicon photodetectors at reverse bias voltage. At the same time, the research group also studied the influence of silicon doping on Gr/Si photodetectors [120, 121]. They constructed Gr/n-Si and Gr/p-Si Schottky junctions respectively by contacting n-type silicon and p-type silicon with graphene. They found that Gr/n-Si Schottky junctions had higher Schottky barrier height and larger rectification factor. This was because graphene was slight p-type doped due to the influence of chemical reagents in the transfer process and PMMA residues, as well as oxygen and water vapor in the air environment [122, 123]. Compared with Gr/p-Si Schottky junction, Gr/n-Si has lower reverse saturation current and higher detectivity, so it is more suitable for photodetectors.

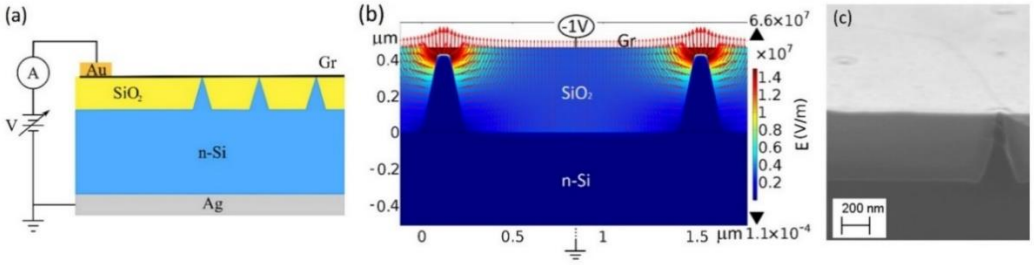

Figure 1-21 Graphene/Si-nanotip photodetector. (a) Layout and measurement setup of the Gr/nSi-tip device. (b) The electric field in the region between two Si-tips. (c) SEM cross-section image of the Si-tip. [118]

As a Schottky contact device, the performance of Gr/Si photodetector is largely determined by the interface quality of graphene and silicon. However, the Gr/Si interface usually has a high surface density of states, which results in Fermi level pinning effect and large leakage current, increases carrier recombination at the interface, and further affects the performance of Gr/Si Schottky photodetectors. Similar to the metal/insulator/semiconductor (MIS) structure in traditional Schottky junction devices, adding an interfacial layer in the Gr/Si Schottky junction photodetector can effectively reduce the dark current and improve the detectivity [124]. One of the most commonly used methods is to oxidize the silicon surface to obtain a thin layer of silicon dioxide as the interfacial layer of Gr/Si Schottky junction. Li et al. exposed silicon substrate to air at room temperature for two weeks to grow a SiO_2 thin film with a thickness of ~2 nm, and transferred graphene on it to fabricate graphene/insulator/silicon Schottky photodetector, as shown in Fig 1-22. In this structure, the interfacial silicon oxide thin film worked as a barrier layer to suppress the dark current of the photodetector, which reduced the dark current from 9.35 nA to 0.1 nA. At the same time, the rectification characteristics and photoelectric response characteristics of Gr/Si Schottky junction were still intact after adding silicon oxide layer. The rise time and fall time of photoelectric response were 0.32 ms and 0.75 ms, respectively. The current responsivity of the photodetector was 0.73 A/W , which remained unchanged after inserting oxide layer. The open circuit voltage of the photodetector increased from 0.453 V to 0.528 V, which indicated that the existence of SiO_2 interfacial layer could enhance the barrier height of Gr/Si Schottky junction. When the incident wavelength was 890 nm, the detector reached maximum detectivity of 4.08×10^{13} Jones, and the equivalent noise power was 0.0078 $pW/Hz^{1/2}$, which was comparable to commercial silicon photodetectors [125].

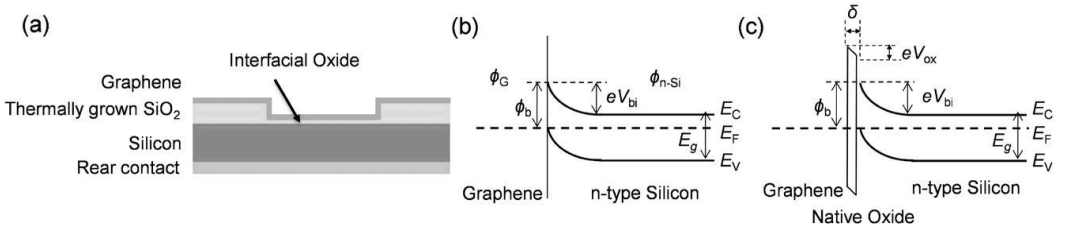

Figure 1-22 The schematics and energy-band diagrams of the Gr/Si heterojunction with SiO_2 interlayer. [125]

Aaesha et al. [126] used atomic layer deposition technology to insert Al_2O_3 thin film at the interface of Gr/Si Schottky junction. As shown in Fig. 1-23, the presence of Al_2O_3 thin film reduced the carrier recombination at the Gr/Si interface, and at the same time, promoted the transmission of photogenerated carriers, thus significantly improved the performance of the photodetector. The barrier height of the Gr/Si Schottky junction increased from 0.843 eV to 0.912 eV, the open circuit voltage increased from 0.45 V to 0.48 V, and the photoelectric conversion efficiency increased from 7.2% to 8.7%. In addition, the photocurrent of Gr/Si Schottky junction was slightly enhanced by Al_2O_3 interfacial layer, the photocurrent responsivity increased from 277 mA/W to 286 mA/W. The Al_2O_3 interfacial layer also improved long-term stability of the device. After four weeks of storage, the performance of the Gr/Si Schottky photodetector with Al_2O_3 interlayer had no obvious change compared with that when the device was just fabricated. Although the naturally grown SiO_2 interlayer was also able to improve the device performance, but the thickness of the SiO_2 layer would gradually increase due to continuous natural oxidation, resulting in gradually degradation of the photodetector over time. The natural oxidation of silicon surface could be prevented by using Al_2O_3 interlayer instead of SiO_2, so the Gr/Al_2O_3/Si exhibited long-term stability.

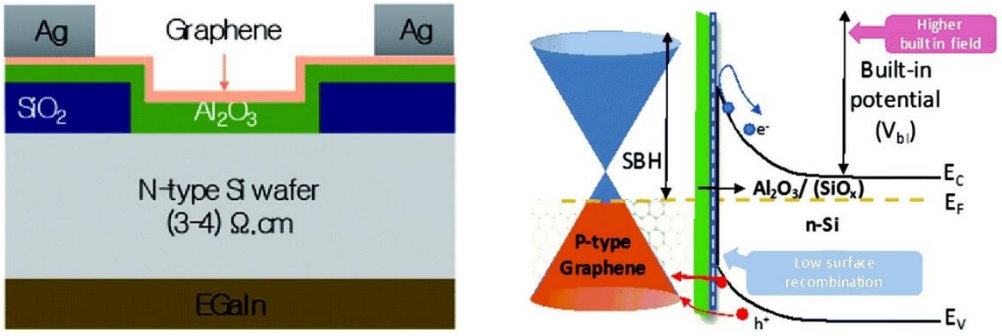

Figure 1-23 Graphene/silicon photodetector with Al_2O_3 interlayer. (a) Photodetector schematics. (b) Band diagram of the photodetector [126]

Zhang et al. [112] inserted P3HT into the Gr/Si Schottky junction as an interface layer to enhance its photoelectric response. As shown in Fig. 1-24, the thickness of P3HT interface layer was ~10 nm, which promoted the transmission of holes from silicon to graphene and blocked the transmission of electrons from silicon to graphene, thus reducing the recombination of carriers in graphene. The lowest unoccupied molecular orbital (LUMO) of P3HT is 3.2 eV, which is much higher than the bottom of conduction band of silicon (4.05 eV), so it worked as an electron barrier layer to inhibit electron transport from silicon to graphene. The highest occupied molecular orbital (HOMO) of P3HT is 5.1 eV, which is close to the top of valence band of silicon (5.17 eV), so it does not block the transmission of photogenerated holes from silicon to graphene. With the insertion of P3HT interlayer, the photocurrent responsivity of Gr/Si Schottky photodectector increased from 235 mA/W to 285.6 mA/W and the photoelectric conversion efficiency increased from 6.85% to 8.71%.

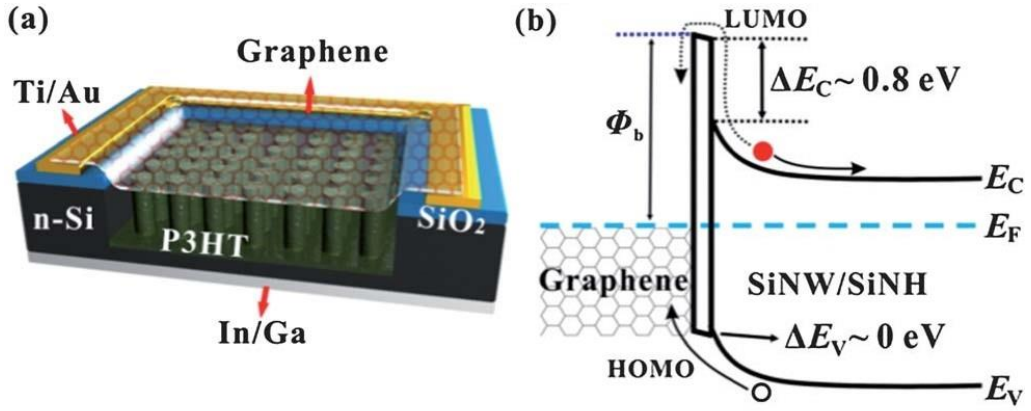

Figure 1-24 Graphene/silicon photodetector with P3HT surface modification. (a) Photodetector schematics. (b) Band diagram of the photodetector [112]

Surface modification of graphene can also improve the performance of Gr/Si Schottky photodetectors, including the chemical doping by Bis(trifluoromethane sulfonimide) (TFSA) [127], $SOCl_2$ [99, 128], HNO_3 [96, 97, 99, 128], $AuCl_3$ [110, 129], and nanostructure modifications such as silver nanowires [116], gold nanoparticles [130, 131], and titanium dioxide nanoparticles. Surface modifications usually lead to the doping of graphene, changing the Fermi level of graphene can adjust the built-in potential of Gr/Si Schottky junction. At the same time, the doping effect reduces the resistance of graphene and improves the performance of Gr/Si Schottky photodetector. In fact, the chemical doping of graphene, as an effective means to enhance the photoelectric response, has been widely used in various Gr/Si Schottky optoelectronic devices. As early as 2012, Miao et al. [127] improved the photoelectric response of Gr/Si Schottky junction by p-type doping graphene with TFSA, as shown in Fig. 1-25. The results showed that the barrier height of Gr/Si Schottky junction increased from 0.79 eV to 0.89 eV after TFSA doping, so the open circuit voltage of the device increased from 0.43 V to 0.54 V, and the photocurrent responsivity increased from 142 mA/W to 253 mA/W due to the increase of built-in potential. In addition, the series resistance of Gr/Si Schottky junction decreased from 14.9 Ω to 10.3 Ω due to the higher carrier concentration of doped graphene, which reduced the ohmic lose inside the device.

The p-type doping of graphene with HNO_3 is a more widely used method. Nitrate ions can effectively reduce the resistance of graphene and increase the work function of graphene, thus promoting the separation and transmission of photogenerated carriers [99]. In Gr/Si Schottky junction photodetectors, the built-in potential and Schottky barrier height are directly related to the difference of graphene work function and silicon electron affinity. Therefore, increasing the work function of graphene by chemical doping can increase the Schottky barrier height and improve the device performance. Li et al. [99] demonstrated that, compared with $SOCl_2$, HNO_3 doping can more effectively improve the open circuit current and the photoelectric conversion efficiency of Gr/Si Schottky junction optoelectronic devices. Due to the simple operation, low cost and remarkable effect, HNO_3 doping of graphene is widely used in various Gr/Si Schottky junction optoelectronic devices, and is usually used together with other

methods to further improve the device performance [93, 97, 131]. However, chemical doping methods are not stable; the device performance generally degrades significantly in a few days, which limits its practical application [132, 133].

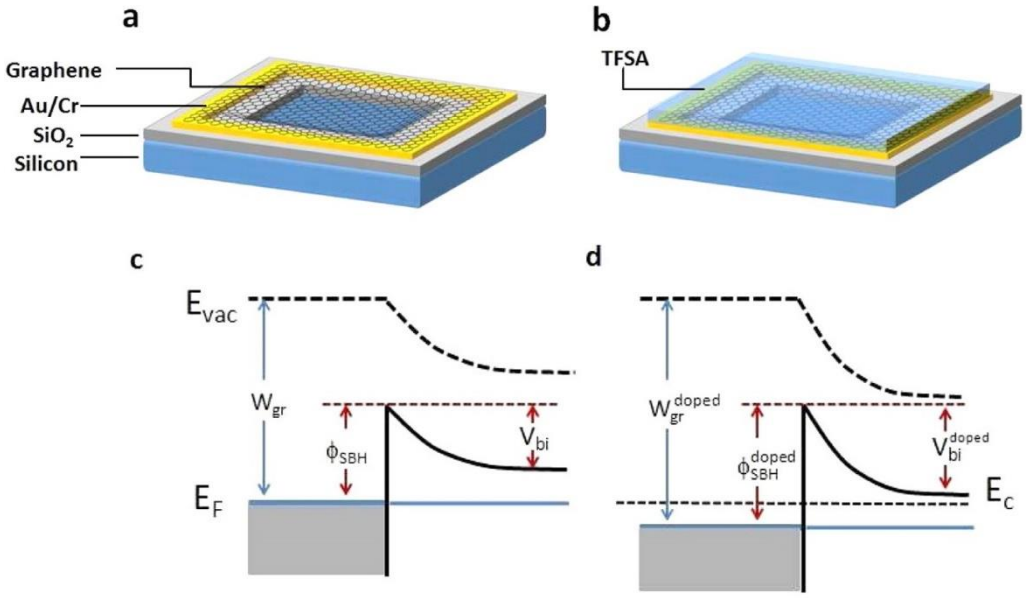

Figure 1-25 Graphene/silicon photodetector with TFSA doping. (a)(b) Photodetector schematics before and after the doping. (c)(d) Band diagram of the photodetector before and after the doping [127]

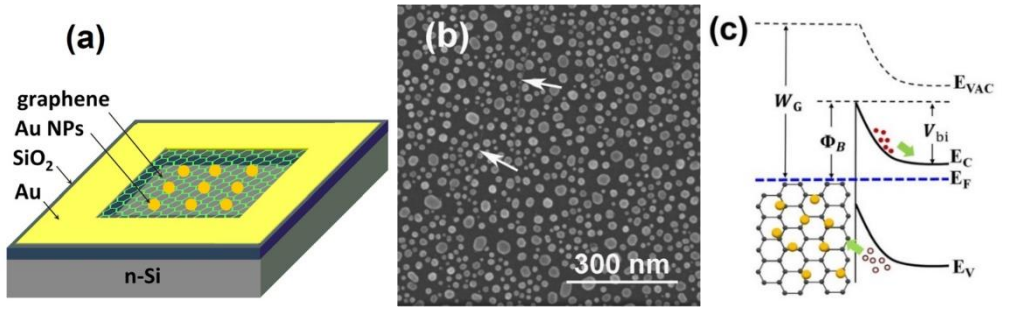

Figure 1-26 Graphene/silicon photodetector with Au nanoparticles. (a) Schematiscs of the photodetector. (b) SEM image of Au NPs on graphene. (c) Band diagram of the photodetector [130, 131]

Shin et al. [116] studied the effect of silver nanowire modification with different concentrations on the photoelectric properties of Gr/Si Schottky junction devices. The electron in silver nanowires injected into graphene due to the work function difference and lead to the doping of graphene. With the concentrations increase of silver nanowire, the resistance of graphene decreased rapidly, which made the device show low series resistance and high photocurrent, but it led to the decrease of carrier mobility in graphene in the meantime. The work function of graphene decreased from 4.52 eV to 4.33 eV with the increase of doping concentration, which led to the decrease of Gr/Si Schottky barrier height and hindered the separation and collection of photogenerated carriers. Liu et al. [130, 131] used gold nanoparticles to modify the surface of graphene, as shown in Fig. 1-26. The gold nanoparticles were obtained by gold thin film annealing. As the work function of gold is 5.3 eV, which is higher than that of graphene (4.6 eV ~ 4.8 eV),

the electrons in graphene flows into gold when they contact with each other, which makes graphene p-type doping. Thus the barrier height of Gr/Si Schottky junction increased from 0.76 eV to 0.81 eV, and the current responsivity of the device increased from 274 mA/W to 314 mA/W. Liu et al also proposed that the local surface plasmon excited by gold nanoparticles might enhance the local light field intensity and improve the device performance, but they did not discuss in depth.

Huang et al. [133] used 2D fractal platinum nanoparticles to modify the surface of Gr/Si Schottky junction. As shown in Fig. 1-27, the average diameter of 2D fractal platinum nanoparticles was 30 nm, the width and thickness of the branch was about 5 nm. Compared with the common spherical nanoparticles, the fractal structure had large ratio of shaped corner and generated more intensive local surface plasmon, thus the near field light intensity was five times more than the background and the modified Gr/Si Schottky junction absorbed more incident light energy. Due to the high work function (5.7 eV) of Pt, holes in Pt transferred into graphene, which induced p-type doping of graphene and increased its work function. As a result, Gr/Si Schottky barrier height increased, which strengthened the built-in electric field and promoted the separation and collection of photogenerated electron hole pairs. The photocurrent responsivity reached 26 A/W with the combination of plasmonic effect and physical doping effect.

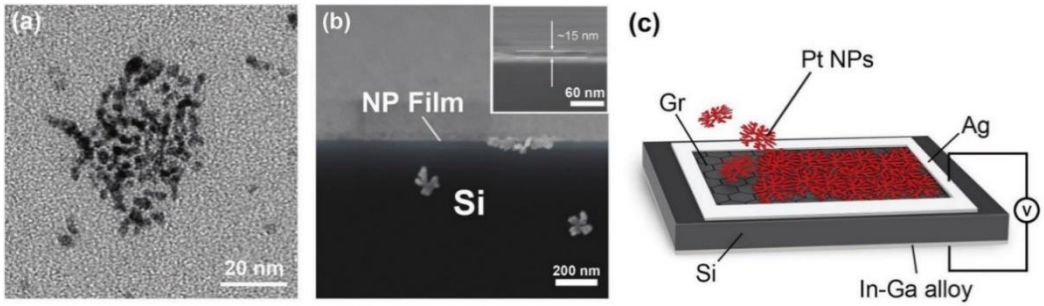

Figure 1-27 Graphene/silicon photodetector coupled with 2D fractal platinum nanoparticles. (a) TEM image of single 2D fractal platinum nanoparticles. (b) Section SEM image of the photodetector. (c) Schematic diagram of the photodetector [133]

Semiconductor nanomaterials can also be used to enhance the performance of graphene/silicon Schottky junction, but the mechanism is different from that of metal nanomaterials. Zhu et al. [93] spin-coated titanium dioxide (TiO_2) nanoparticles on the surface of Gr/Si Schottky junction to enhance its ultraviolet absorption and photoresponse, as shown in Fig. 1-28. TiO_2 nanoparticles were synthesized by sol–gel method and well-dispersed with an average size of 3 nm~5 nm. As the band gap of nanoparticles was relevant to their sizes, the band gap was 3.0 eV ~ 3.2 eV, corresponding to the wavelength of 388 nm ~ 413 nm. Ag, Au, Pt and other metal nanomaterials mentioned above always change the Fermi energy level of graphene through doping effect to enhance the performance of graphene/silicon Schottky junction. However, there are two built-in potentials in the TiO_2 nanoparticles modified graphene/silicon Schottky junction. As shown in

Fig. 1-28, one lied at the TiO_2/graphene interface and another lied at graphene/silicon interface. The incident photons with energy higher than the band gap of TiO_2 were absorbed to generate electron hole pairs. As TiO_2 is a wide band gap dielectric material with poor conductivity, the photogenerated electrons remained in the TiO_2, while the photogenerated holes can be transported to graphene together with the current generated from graphene/silicon side to the external circuit. As a result, the responsivity of the TiO_2/Gr/Si photodetector increased from 60.6 mA/W to 71.9 mA/W under the incident light with 420nm wavelength.

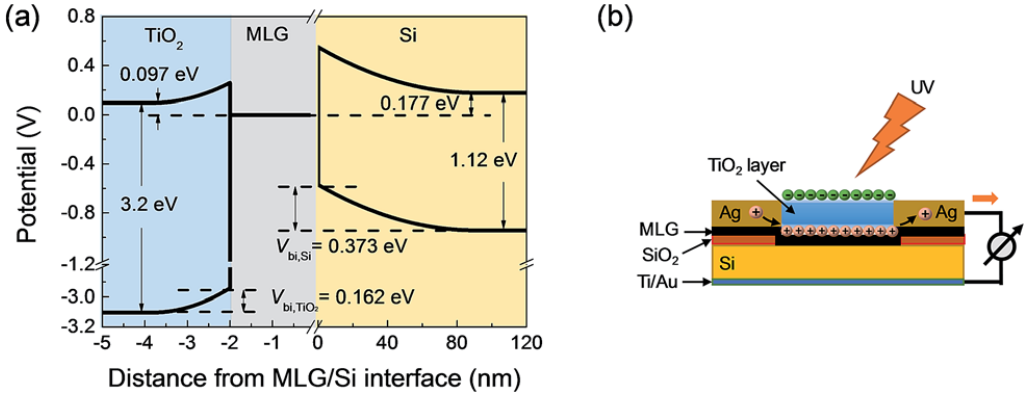

Figure 1-28 Graphene/silicon photodetector enhanced by titanium dioxide nanoparticles. (a) Band diagram. (b) Schematic diagram. [93]

This subsection introduces the development of graphene/silicon Schottky junction photodetector, as well as the research status of its performance enhancement by improving the silicon structure, optimizing the graphene/silicon interface and modifying the graphene surface. These three methods can effectively enhance the performance of Gr/Si Schottky photodetector by improve its different part: silicon, graphene/silicon interface and graphene. In Gr/Si Schottky photodetector, silicon absorbs light and excites electron hole pairs, and the photo generated carriers are separated by built-in potential and collected by graphene and silicon respectively to form photocurrent in external circuit. The absorption of incident light in a specific band can be improved by surface texturing of silicon, or by using silicon nanorods/holes, silicon quantum dots and other materials instead of bulk silicon materials to construct Gr/Si Schottky junction. Inserting an interface layer between graphene and silicon can reduce the interface density of states and suppress the dark current of the detector. If the interface layer is hole conductive material, the electrons transmission from silicon to graphene will be blocked, which can reduce the recombination of electrons and holes and enhance the photoelectric response of the detector. In the third chapter, graphene oxide film is inserted as the interface layer to suppress the dark current and increase the photocurrent of the graphene/silicon detector. The conductivity of graphene can be increased by chemical treatment or nanomaterial modification of graphene surface. Meanwhile, the doping effect influences the Fermi level of graphene, increases the barrier height and built-in potential of Gr/Si Schottky junction, and improve the device performance. If the graphene surface is modified by noble metal nanostructures, the local surface plasmon effect will enhance the

light field intensity near the surface, and improve the photoelectric response of the detector together with doping effect. In the fourth chapter, gold nanoparticles and gold nanodisks are fabricated by thin film annealing method and electron beam lithography method, respectively. By optimizing the structural parameters, the gold nanoparticles and nanodisks can effectively improve the performance of graphene/silicon Schottky photodetector.

1.4 Parameters of photodetectors

In order to evaluate the performance of photodetectors, various paramaters are generally used in the industry, including responsivity, dark current, spectral response, quantum efficiency, response speed, equivalent noise power, detectivity, on/off ratio.

(1) Responsivity

Responsivity is a physical quantity that directly reflects the photoelectric conversion ability of the detector. According to the type of output electrical signal, it falls into two categories: current responsivity and voltage responsivity. The definition of responsivity is the ratio of output photocurrent or photovoltage to incident light power. For voltage output photodetectors, the voltage responsivity can be expressed by the following formula:

$$\mathrm{R} = \frac{V_{ph}}{P} \tag{1-1}$$

where V_{ph} is the photovoltage of the detector, P is the light power incident on the effective working area of the detector, which can be expressed as:

$$P = P_{in} \times A \tag{1-2}$$

where P_{in} is the power density of incident light, and A is the effective working area of the detector. For current output photodetectors, the current responsivity can be expressed by the following formula:

$$\mathrm{R} = \frac{I_{ph}}{P} \tag{1-3}$$

where I_{ph} is the photocurrent of the detector. Dark current is the electric current flowing in a photoelectric device when there is no incident illumination. The generation of dark current is complicated and affected by many factors, including leakage current, reverse diffusion current, generation-recombination current, tunneling current, ohmic current. When calculating the photocurrent of the detector, the dark current should be deducted from the total current, as shown in the following formula:

$$I_{ph} = I_l - I_d \tag{1-4}$$

where I_l is the measured current passing through the detector under illumination, and I_d is the dark current of the detector. In the industrial production and scientific research, the current responsivity is an important parameter to evaluate the performance of photodetectors. In addition, some literatures use the photocurrent density (J_{ph}) to describe the incident light instead of photocurrent I_{ph}, and the current responsivity of the detector can be expressed as follow:

$$\mathrm{R} = \frac{J_{ph}}{P_{in}} \tag{1-5}$$

(2) Spectral response

Most photodetectors have spectral selectivity and their responsivity varies with the wavelength because of the absorptivity difference of the materials that construct the detectors in different wavelength range. Spectral responsivity refers to the ratio of the photovoltage or photocurrent to the incident light power under the illumination of different wavelength:

$$R(\lambda) = \frac{V_{ph}(\lambda)}{P(\lambda)} \text{ or } \frac{I_{ph}(\lambda)}{P(\lambda)} \tag{1-6}$$

Different type of detectors have different detection spectral range due to their structure and material. The photoelectric performance of the detector in the whole detection spectrum range can be obtained by measuring the responsivity as a function of wavelength.

(3) Quantum efficiency

Quantum efficiency is the ratio of the number of electrons in the external circuit produced by an incident photon, including external quantum efficiency and internal quantum efficiency. The external quantum efficiency is the ratio of the number of collected carriers and the number of incident photons:

$$\eta_e = \frac{N_c}{N_e} = \frac{I_{ph}/e}{P/hv} = \frac{I_{ph}}{P} \cdot \frac{hc}{e\lambda} \tag{1-7}$$

where N_c is the number of photo generated carriers that contribute to photocurrent, N_e is the number of photons incident on the photosensitive surface of the detector, e is electron charge (1.6×10^{-19} C), h is Planck constant (6.626×10^{-34} J·s), v is the frequency of incident light, c is vacuum light speed (3×10^8 m/s), and λ is the wavelength of incident light. There is a constant relationship among frequency, wavelength and light speed, v=c/λ.

Quantum efficiency is a very important parameter for the photodetectors dominated by photovoltaic effect. In ideal photodetector, all photons are absorbed and the photogenerated carriers are collected, then its quantum efficiency is equal to 1. However, in actual, not all incident photons can be absorbed to excite electron hole pairs and generate photoelectric signals. Moreover, due to the recombination or trapping of carriers before they are collected, the external quantum efficiency of photodetectors in zero bias state is always less than 1. When the external energy is provided, such as applied bias voltage, the photodetectors with internal gain mechanism like photomultiplier tubes and avalanche diodes can get additional gain to make the external quantum efficiency lager than 1.

In contrast, the internal quantum efficiency is the ratio of the number of collected carriers and the number of absorbed photons:

$$\eta_i = \frac{\eta_e}{1-R^*-T^*} \tag{1-8}$$

where R* and T* are the reflectivity and transmittance of the detector, respectively. Since there are always reflection and transmission when light is incident on the detector, the value of internal quantum efficiency η_i is always greater than external quantum efficiency η_e.

(4) Response speed

Photoelectric system uses light to perform a variety of functions in both industrial and commercial applications, such as measuring distance or detecting the presence or absence of one or more objects. Photodetector is the core component of the photoelectric system and its performance directly influences the quality of the photoelectric system. The response of the photodetector to the incident light signal has a certain delay, that is, the output electrical signal lags behind the input optical signal on the time axis. When the optical signal to be measured changes rapidly with time, the output signal will be seriously distorted due to the delay of the photodetector. Therefore, the evaluation of the response speed of photodetectors is very important for the selection of detectors in practical applications. There are two methods to evaluate the response speed of photodetector: amplitude frequency characteristic method and pulse response method.

Due to the time delay of photodetectors, the photoelectric responsivity is not only related to the wavelength of incident light, but also related to the modulation frequency of incident light. The amplitude frequency characteristic of the photodetector can be obtained by measuring the response amplitude of the photodetector to the incident light signals with different modulation frequencies. Under the incident light with a certain power density and variable modulation frequency, when the output signal is attenuated by 3dB, the corresponding frequency is cut-off frequency. The bandwidth of the detector can be defined as:

$$\Delta f = f_2 - f_1 \tag{1-9}$$

where f_1 and f_2 are the lower and upper cut-off frequencies of the detector respectively. In addition, if the whole amplitude frequency characteristic spectrum of the photodetector is known, its bandwidth can also be calculated by the following formula:

$$\Delta f = \int_0^\infty \left|\frac{R(f)}{R_{max}}\right|^2 df \tag{1-10}$$

where R(f) is the responsivity as a function of modulation frequency of the incident light, and R_{max} is the maximum value of R(f).

In addition, the response time of the photodetector can be measured by pulse response method. When the incident light is switched on or off suddenly, the electrical signal output of the photodetector takes some time to rise and fall. Generally, the time to rise from 0 to 90% of the maximum value is defined as the rise time, and the time to decrease from the maximum value to 10% is defined as the falling time. The sum of rise time and fall time reflects the response speed of the device.

Both the amplitude frequency characteristic method and pulse response method reflect the response speed of the detector, and widely used in related scientific research and practical application. In most cases, the faster the detector responds, the better. An effect method to improve the response speed of the photodetector is reducing the defect density by improving the quality of the material and interface in the photodetector.

(5) Noise equivalent power

When the incident light power is very low, the photoelectric response of the photodetector will be submerged by its noise, which makes it difficult to recognize the response to the incident light from the mixed signal. The average value of random noise signal is zero, but its root mean square is not zero. The noise equivalent power (NEP) refers to the minimum power of the incident light that allows to determine the noise component of the photodetector, which can be expressed by the following formula:

$$\mathrm{NEP} = \frac{P}{I_s/I_n} \text{ or } \frac{P}{V_s/V_n} \tag{1-11}$$

where I_s and I_n are response current and noise current respectively, V_s and V_n are response voltage and noise voltage respectively. Only when the incident light power is greater than the noise equivalent power of the photodetector, the response signal and noise can be distinguished from the output signal of the detector.

(6) Detectivity

Detectivity is an important parameter to evaluate photodetectors. It describes the ability of the detector to produce an observable output signal under the influence of noise. That is, the larger the detectivity of a photodetector, the more it is suitable for detecting week signals which compete with the detector noise. The detectivity and noise equivalent power are reciprocals each other:

$$D = \frac{1}{NEP} \tag{1-12}$$

It should be noted that the detectivity is related to the bandwidth and active area of the photodetector. The specific detectivity D* is the detectivity normalized to a unit detector area and detection bandwidth, which can calculate by the following formula:

$$D^* = \frac{\sqrt{A\Delta f}}{NEP} \tag{1-13}$$

The specific detectivity eliminates the influence of the bandwidth and active area, which is useful for comparing the performance of different detector technologies. The unit specific detectivity of is $m\sqrt{Hz}/W$ or $cm\sqrt{Hz}/W$, the latter is more commonly used, also known as *Jones*. In practical application, the specific detectivity of photodetector can be calculated more conveniently by the following formula [116, 134]:

$$D^* = \frac{A^{1/2}R}{\sqrt{2eI_d}} \tag{1-14}$$

(7) On/off ratio

For photodetectors, the on/off ratio refers to the ratio of photocurrent to dark current. With the same incident light power, the higher the on/off ratio of a photodetector, the smaller the dark current.

$$r_{on/off} = \frac{I_{ph}}{I_d} \tag{1-15}$$

1.5 Research route and main content

In this thesis, monolayer graphene was synthesized by chemical vapor deposition and used to fabricate graphene/silicon Schottky photodetectors. The

photoresponse of the Gr/Si photodetector was improved by graphene oxide interlayer and gold nanoparticles surface modification. Besides, a new method to directly transfer graphene and fabricate graphene/silicon Schottky photodetector by two-step hot-embossing process was proposed.

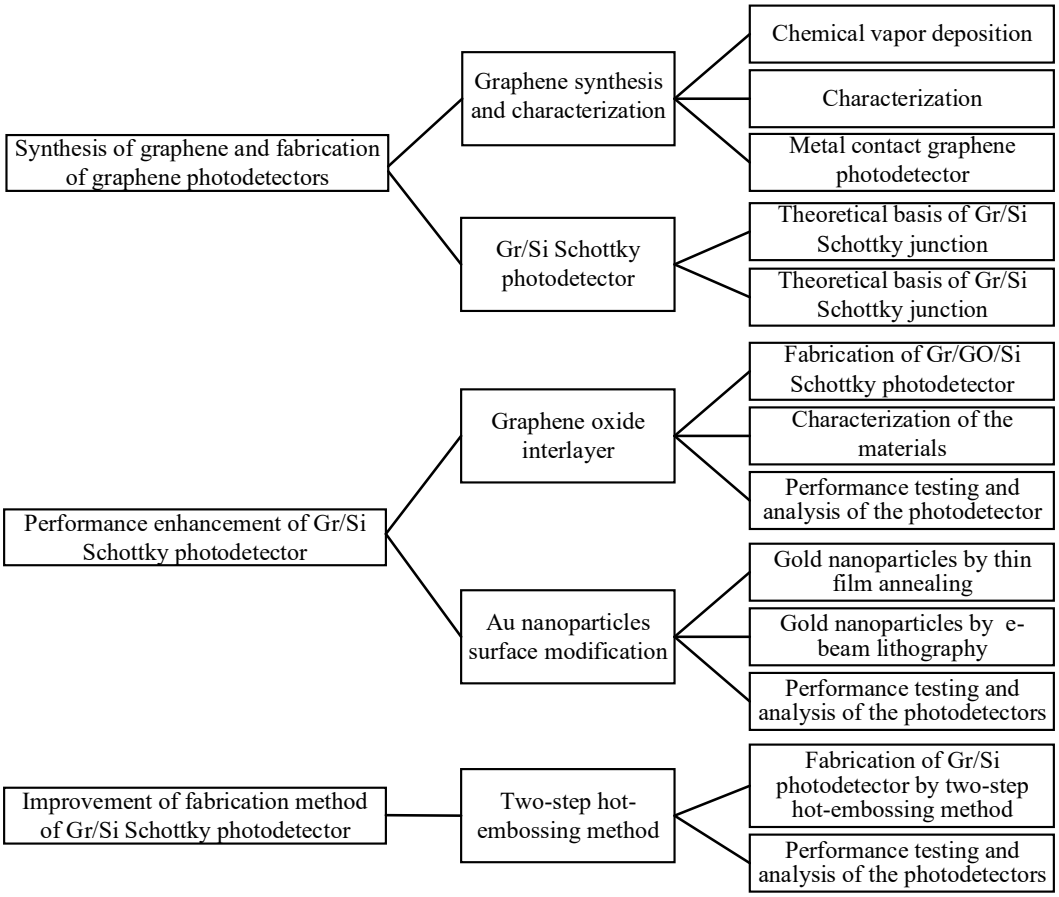

Figure 1-29 Research route of the thesis

The main content of this thesis is as follows:

Chapter 1 is the introduction to the research background and significance of this thesis, the properties and synthesis methods of graphene, the development status of graphene photodetectors and the important parameters of photodetectors. The first section of this chapter introduces the present situation of photodetectors, the problems faced by traditional semiconductor photodetectors. The second section introduces the unique properties of graphene, the development trend of graphene synthesized by chemical vapor deposition, and its advantages in the field of photodetectors. The third section introduces the metal contact graphene photodetectors and graphene heterojunction photodetectors, and the performance enhancement methods of graphene/silicon Schottky junction photodetectors. The forth section introduces the parameters to evaluate the performance of photodetectors. Finally, the fifth section introduces the research content and purpose of this thesis.

In Chapter 2, single layer graphene was synthesized by chemical vapor deposition, and PMMA was used as temporary support layer to transfer graphene from the catalytic substrate to target substrate. Graphene was characterized by Raman spectroscopy, scanning electron microscopy and atomic force microscopy.

The results showed that the graphene was monolayer with good integrity and continuity in a large range. The thickness of PMMA residual on the surface of graphene was about 5nm. The metal graphene metal structure was fabricated to verifie the photoelectric detection performance of the graphene. While the responsivity was about 4 mA/W, and the high dark current seriously affected the performance of the photodetector. This chapter introduces the theoretical basis of graphene/silicon Schottky junction, including its formation mechanism, working principle and analysis methods of electrical characteristics. The graphene/silicon Schottky photodetector was fabricated by using the as-prepared graphene, and its photoelectric response was characterized. The current responsivity of the Schottky photodetector was 0.23 A/W and the on/off ratio was 3.7×10^3 under the incident light with the wavelength of 633 nm. The Gr/Si photodetector responded correctly and quickly to the incident light with different power density, and the response time was about 1 ms. In order to analyze the performance of the Schottky junction, the series resistance, ideal factor and Schottky barrier height of were extracted from the current-voltage characteristic by thermal electron emission theory, Cheung equation and Norde equation.

In Chapter 3, the graphene/silicon Schottky photodetector was enhanced by inserting graphene oxide thin film as the interface layer. The Gr/GO/Si photodetector with graphene oxide interface layer was fabricated, and its photoelectric response and electrical characteristics were measured and analyzed. The results showed that the dark current of the photodetector reduced by one order of magnitude and the photocurrent increased by 2.73 times due to the insertion of GO interface layer. The responsivity of Gr/GO/Si photodetector reached 0.65 A/W and the on/off ratio reached 2.73×10^5 under the 633 nm incident light. The photocurrent of the device was proportional to the incident light intensity. The photodetector responded accurately and quickly to the periodic light signal, which showed its good stability and reliability. The rise/fall time of the Gr/GO/Si photodetector was about 1 ms, which was essentially the same with Gr/ Si photodetector. In addition, based on the thermal electron emission theory, Cheung equation and Norde equation, the key parameters of Schottky junction were extracted from the current-voltage characteristic, and the mechanism of GO interlayer to improve the detector performance was discussed.

In Chapter 4, gold nanoparticles and gold nanodisks were fabricated by thin film annealing and electron beam lithography, respectively, to modify the graphene/silicon Schottky photodetectors to further improve the photodetection ability. The morphology and distribution of gold nanoparticles were tuned by changing the deposition thickness and annealing parameters, and the optical field distribution was calculated by finite difference time domain (FDTD) method. For the gold nanodisks, the influence of disk diameter, thickness and distance on the local light field was analyzed by FDTD method, and a set of optimal structural parameters were obtained. The gold nanodisks were fabricated on the surface of graphene/silicon Schottky photodetector by electron beam lithography, metal deposition and lift-off process. By the photoelectric and electrical characterization

of the device, the influence of gold nanodisk array on the detector performance were analysed and compared to that of disordered gold nanoparticles.

In Chapter 5, the two-step hot-embossing method was proposed to transfer graphene and fabricate graphene/silicon Schottky photodetector. Firstly, the CVD graphene was transferred directly from the original copper foil substrate to the COC film substrate by hot-embossing process; then, the graphene on the COC film substrate was embossed together with the pre-fabricated silicon substrate by hot-embossing process, and the graphene/silicon Schottky contact was formed in the silicon window area. Under the irradiation of 633nm light source, the photocurrent of the detector increased linearly with the incident light power density, and its responsivity was 0.73 A/W. The key parameters of Schottky junction were extracted from the current-voltage characteristic. The results showed that the graphene/silicon Schottky junction photodetectors fabricated by the two-step hot-embossing method had the same or slightly higher photoelectric response ability than those fabricated by traditional methods, which provided a simple and reliable approach for the preparation of graphene based devices.

Chapter 6 is the conclusion and prospect, which summarizes the conclusions, the innovations and the prospects of this thesis.

Chapter 2

Preparation and characterization of graphene and graphene photodetectors

2.1 Introduction

In the past decade, graphene has attracted extensive attention in the field of photoelectric detection due to its unique electrical and optical properties. Materials scientists first successfully separated graphene from graphite by mechanical exfoliation. This method can obtain high quality graphene, but it is inefficient and difficult to produce on a large scale. With the development of technology, chemical vapor deposition (CVD) is the most promising method for the production of graphene. Graphene photodetectors based on metal graphene metal (MGM) structure take the advantages of high carrier mobility and wide spectrum absorption of graphene, which can achieve high-speed and wide spectrum detection. However, the responsivity and on/off ratio of the photodetectors are limited by the lower optical absorption coefficient of graphene.

In this chapter, single-layer graphene film was grown on copper foil substrate by CVD with methane as carbon source, and MGM photodetector was fabricated to verify the photoelectric detection performance of graphene. As the metal contact graphene photodetector is a junction-free device, the dark current of the photodetector is large when the bias voltage is applied, and the low light absorption rate of graphene leads to the low responsivity and on/off ratio of the photodetector. Then the graphene/silicon (Gr/Si) Schottky junction photodetector was fabricated. This chapter describes the fabrication process of graphene/silicon Schottky photodetector in detail, and tests its photoelectric response and spectral response. When the Gr/Si photodetector works in the reverse bias state, the built-in potential increases, which promotes the separation of photogenerated carriers. Due to the suppression of dark current by Schottky barrier, the Gr/Si

photodetector showed higher responsivity and on/off ratio. This chapter theoretically analyzes the formation and working principle of graphene/silicon Schottky junction, introduces three methods to calculate the key parameters of Gr/Si Schottky junction through current-voltage characteristics, including hot electron emission equation, Cheung equation and Norde equation.

2.2 Preparation and characterization of graphene

2.2.1 Synthesis of graphene

In this paper, graphene thin film was synthesized by CVD method. Methane (99.99%) was used as carbon source and hydrogen (99.9%) was used as auxiliary gas. Graphene was grown on copper foil substrate (Alfa aesar, 25 μm). The equipment used is CVD growth system (Anhui, BEQ), which consists of vacuum tube furnace, gas supply system and vacuum system.

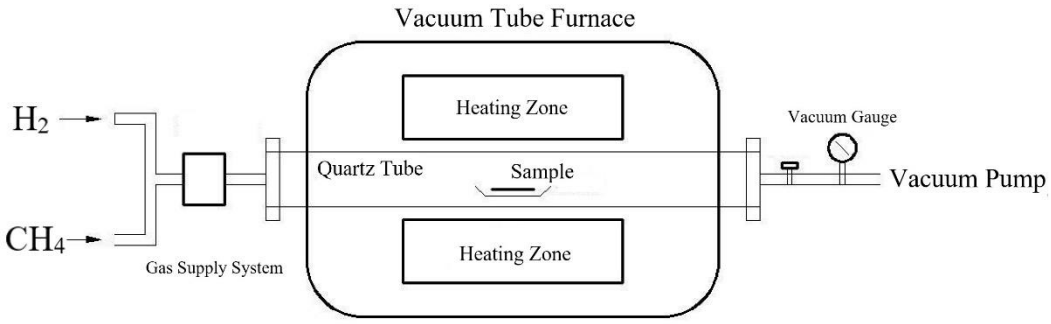

Figure 2-1 Schematics of CVD system

The detailed process is as follows:

1) Prepare the substrate. The copper foil was cut into 2cm × 5cm rectangular pieces, placed on the quartz carrier and fed into the center of the heating area of the tube furnace.

2) Exhaust the air. After sealing the tube furnace, vacuum the furnace cavity, and then introduce argon into the furnace. Repeat for three times to ensure that there is no residual oxygen in the furnace cavity.

3) Heating stage. With the hydrogen flow of 100 sccm, maintain the pressure of furnace cavity at 0.15 kPa through the baffle valve on the vacuum system. The temperature in the furnace cavity was increased from room temperature to 1060 ℃ in 26 minutes.

4) Annealing stage. Maintain the gas flow rate and pressure, keep the furnace temperature at 1060 ℃ for 30 minutes. The main purpose was to remove the oxide on the surface of copper foil and improve the surface morphology of copper foil.

5) Growth stage. Keep the furnace temperature at 1060 ℃ and inject 30 sccm of methane and 70 sccm of hydrogen simultaneously for 20 minutes. In this stage, methane decomposed into carbon atoms at high temperature and deposited on the surface of copper foil to form graphene film.

6) Cooling stage. Turn off the heating system, make the furnace cavity cool to room temperature, and take out the sample.

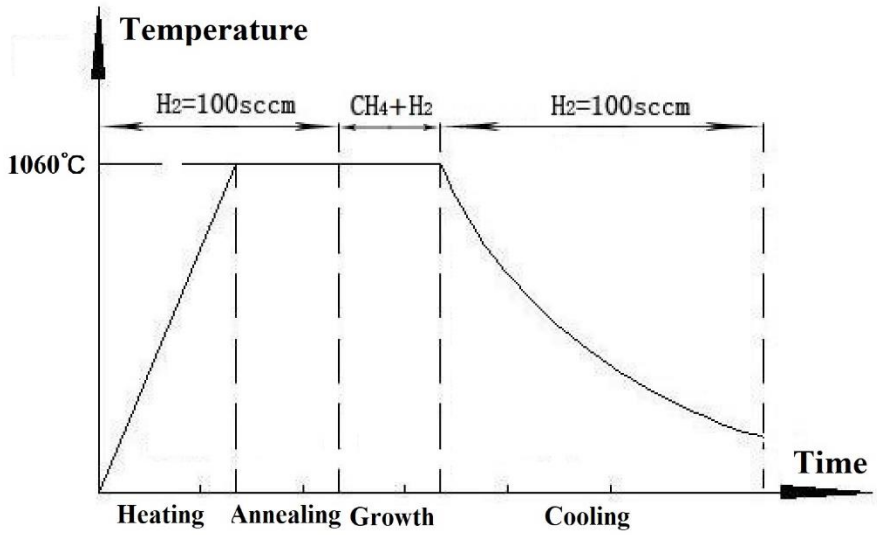

Figure 2-2 Schematic presentation of graphene growth process

2.2.2 Graphene transferring

In order to use the CVD graphene to fabricate photodetector, it is necessary to transfer graphene from copper foil substrate to SiO_2/Si substrate. Here, PMMA was used as temporary support layer to transfer graphene. The detailed process is as follows:

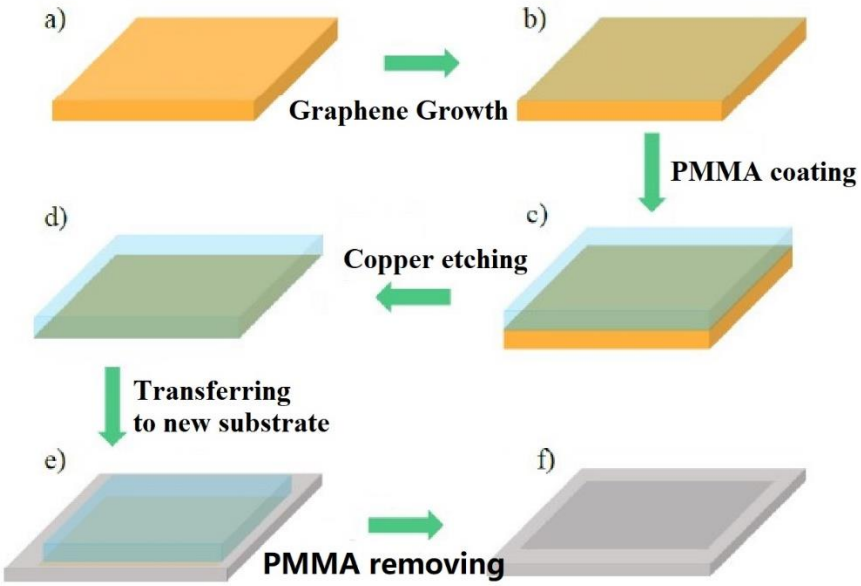

Figure 2-3 Graphene transfer process

1) The 6% PMMA solution was spin coated on the surface of graphene/ copper with the speed of 2000 rpm for 30 seconds.

2) The spin coated PMMA/graphene/copper sample was baked on a 170 ℃ hot plate for 10 minutes to remove the solvent in PMMA layer.

3) The sample of PMMA/graphene/copper was placed on $FeCl_3$ solution (100 mg/ml), and the copper foil was completely etched after 4 hours. Then the PMMA/graphene was rinsed twice with deionized water.

4) The PMMA/graphene was picked up by target substrate, and baked on a 70 ℃ hot plate for 30 minutes, and then on a 95 ℃ hot plate for 30 minutes to completely remove the water between graphene and target substrate.

5) The samples were immersed in acetone sequentially for 10 minutes, 20 minutes and 30 minutes to remove PMMA on graphene to the greatest extent and reduce the impact of PMMA residue on graphene property.

2.2.3 Characterization of graphene

1) Raman spectrum

Raman spectroscopy is a kind of spectral technology based on the inelastic scattering of monochromatic light. Its principle is to use the interaction between the incident light and the lattice vibration of the material to excite the electron in the material from the ground state to a virtual state, and then the virtual state electron jumps to the lower level and releases a new photon. If the energy of the released photon is different from that of the incident photon, the scattering light will have different spectral line from the incident light, which is Raman line. The spectral line whose frequency is less than that of the incident light is called Stokes line, while the spectral line whose frequency is higher than that of the incident light is called anti Stokes line.

In the Raman spectrum with wave number as variable, Stokes line and anti Stokes line are symmetrically distributed on both sides of Rayleigh scattering line, which is due to the energy gain or loss of a vibrational quantum in the above two cases respectively. Due to the Boltzmann distribution, the number of particles in the vibrational ground state is much larger than that in the vibrational excited state, so the intensity of Stokes line is generally higher than that of anti Stokes line. The information of lattice vibration can be obtained by collecting the energy loss photons in Stokes process and analyzing the frequency and distribution.

Raman spectroscopy is a very effective tool in the study of various carbon materials and two-dimensional materials. Since 2006, Ferrari et al. [135] first used Raman spectroscopy to characterize the structure of graphene, Raman spectroscopy has become the most popular characterization technology of graphene in laboratory and industry production. There are three most important peaks in the Raman spectrum of typical single layer graphene: D peak at 1350 cm^{-1} caused by defects, G peak near 1584 cm^{-1} caused by E_{2g} vibration, and 2D peak near 2680 cm^{-1}. It is worth noting that the positions and relative intensities of Raman peaks in graphene synthesized by different methods are also different due to their different structures. For example, the D peak of graphene oxide is very strong due to many defects, while the 2D peak is relatively weak; for high-quality graphene obtained by mechanical exfoliation or chemical vapor deposition, the D

peak is weak and the 2D peak is very strong. Raman spectroscopy is an effective method to characterize graphene films. By analyzing the peak intensity ratio of 2D and G peaks in Raman spectroscopy, the structure and layer number of graphene films can be obtained quickly, sensitively and non-destructively. In this paper, the Raman spectrum of the graphene was measured by HR 800 Raman spectrometer (Horiba jobin Yvon). The light source wavelength is 633nm, the scanning wave number is 1000 ~ 3000 cm^{-1}, and the focusing area is 1 μm × 1 μm.

Figure 2-4 shows the Raman spectrum of the prepared graphene film. D, G and 2D peaks were located at 1335 cm^{-1}, 1584 cm^{-1} and 2662 cm^{-1}, respectively. The FWHM of G and 2D peaks were 16 cm^{-1} and 26 cm^{-1}, respectively. The intensity ratio of 2D and G peaks was $I_{2D/G}$ = 2.7. Single layer graphene always has shape peaks, and the 2D peak is a symmetric Lorentzian line-shape with the FWHM of about 30 cm^{-1}. With the increase of the number of graphene layers, the 2D peak splits into multiple overlapping peaks. The 2D peak of double-layer graphene is the superposition of four Lorentz peaks, and the 2D peak of three-layer graphene is the superposition of six Lorentz peaks [136]. $I_{2D/G}$ is closely related to the number of layers of graphene film [137, 138]. It is generally considered that $I_{2D/G} > 1.3$ is single-layer graphene, $0.7 < I_{2D/G} < 1.3$ is double-layer graphene, and $I_{2D/G} < 0.7$ is multi-layer graphene. The results show that the graphene film grown in this chapter has sharp peaks, the 2D peak is a single and symmetric peak, and the intensity ratio of 2D peak to G peak is $I_{2D/G}$ = 2.7, indicating that the graphene film is single layer.

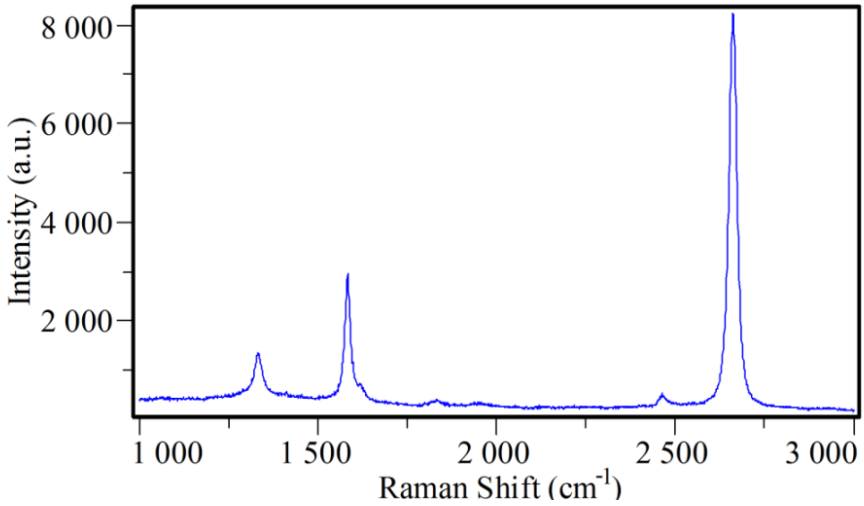

Figure 2-4 The Raman spectrum of the CVD graphene

In general, the shift of Raman lines is independent of the wavelength of the incident light, but only related to the vibration and rotational level of the sample. However, for graphene, the energy of laser source will affect the position of peaks in Raman spectrum [139, 140]. This phenomenon is caused by many factors, including laser-induced electron hole pair excitation, momentum exchange in electron phonon scattering, defect scattering and electron hole recombination [141]. With the increase of laser energy, the 2D peak of monolayer graphene shifts to high frequency and increases with a slope of 88 cm^{-1}/eV, which has a highly

linear relationship with the laser energy. In literatures, 514 nm laser is usually used as the excitation source of Raman spectrum. Therefore, the position of 2D peak of graphene measured by 633nm light source in this chapter is slightly shifted to lower wavenumber (red shift).

In addition, we can see that the Raman spectrum of CVD graphene has obvious D peak, which is due to the lattice dislocation at the grain boundary during the multinucleation growth of graphene. Because the copper foil is produced by calendering method, its surface has deep calendering wrinkles. Although the copper foil substrate has been heat-treated before the growth of graphene in the CVD process, the surface morphology has been improved to a certain extent, but it still has a high defect density, which leads to high nucleation density of graphene in the initial growth stage. After the graphene grains are grown and bridged into thin films, there will be many defects and grain boundaries. The ratio of D peak intensity to G peak intensity can be used to estimate the average size of graphene grains L_a [142],

$$L_a = (2.4 \times 10^{-10})\lambda^4 (I_D/I_G)^{-1} \quad (2\text{-}1)$$

where λ is the wavelength of Raman excitation source, and I_D/I_G is the intensity ratio of D peak to G peak, which is about 0.34. According to formula 2-1, the grain size of CVD grown graphene is about 112 nm.

2) Scanning electron microscope

The scanning electron microscope (SEM) focuses the electron beam emitted by the electron gun on the surface of the sample through the magnetic lens system under the action of the accelerating voltage. Under the action of the deflection coil, the electron beam does grating scanning on the sample to excite the sample to produce various physical signals, such as secondary electron, backscattered electron, Auger electron, etc. The corresponding detectors receive these signals to obtain the surface morphology and composition information of the sample.

The secondary electrons are the extranuclear electrons bombarded by the incident electrons. Because the binding energy between the nucleus and the outer valence electrons is very small, when the outer electrons get more energy than the binding energy from the incident electrons, they can break away from the nucleus and become free electrons. If this process occurs on the surface of the sample, the free electrons with energy greater than the work function of the material can escape from the surface of the sample and become the free electrons in vacuum, that is, the secondary electrons. Because the secondary electrons come from the surface of the sample, the incident electrons have not been scattered many times, and the area of the secondary electrons is approximately equal to the irradiation area of the incident electron, so the secondary electrons have high resolution. The resolution of scanning electron microscope is usually the resolution of the secondary electrons, which can reach 5 nm ~ 10 nm. The generation of secondary electrons is not sensitive to the change of atomic number, but very sensitive to the surface morphology of the sample. Because of the low energy of the secondary electrons, only the secondary electrons generated on the surface of the sample can

escape from the surface, and the escape depth is only a few nanometers. The image formed by collecting the secondary electrons can effectively display the surface morphology of the sample. The electron microscope image is generally the image formed by the conversion of the secondary electron signal. In this thesis, the surface morphology of the samples was measured by Hitachi su-8010 field emission scanning electron microscope. The electron beam accelerating voltage was 5 kV.

Figure 2-5 shows the image of graphene film transferred to SiO_2/Si substrate under scanning electron microscope, indicating the integrity and continuity of graphene film after transfer. Because the copper foil substrate is produced by calendering process, there are obvious calendering wrinkles on the surface. Although the copper foil substrate has been annealed for 30 minutes before graphene growth, the effect of calendering wrinkles cannot be completely eliminated. As shown in Figure 2-5, since graphene was conformally grown on copper foil, obvious wrinkles can be observed after transfer. In addition, the surface of copper foil will recrystallize in the annealing stage, forming a large area of single crystal region, which is conducive to the growth of graphene. However, there are obvious grain boundaries between the copper single crystal regions, so the graphene grown on the copper foil substrate will wrinkle in the corresponding region after transfer. As shown in Figure 2-5 (b), the wrinkle size is micron, which does not damage the continuity of the graphene.

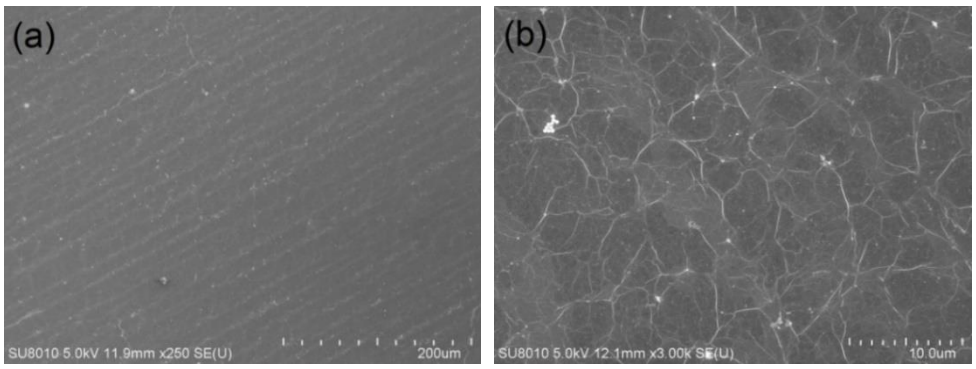

Figure 2-5 SEM images of the CVD graphene transferred to SiO_2/Si substrate with the magnification of (a) 250 and (b) 3000.

3) Atomic force microscope

Atomic force microscope (AFM) is an analytical instrument used to detect the surface morphology and atomic structure of materials. An elastic microcantilever with a nano probe at one end is used to detect the surface morphology of samples. When the tip moves above the sample, the cantilever will deform or move due to the force between the probe and the sample surface. The laser beam on the cantilever will deflect, and the corresponding detector can detect the deflection value of the cantilever. By scanning the sample horizontally, recording the offset and the corresponding position of the sample, the force distribution can be obtained, so as to obtain the surface morphology of the sample.

AFM can sense and amplify the force between the tip probe on the cantilever and the atoms on the sample surface to realize the measurement, which has high

resolution reaching nanometer level even atom level. As an important means to characterize graphene, AFM can obtain the surface morphology of graphene, as well as thickness. The atomic force microscope used in this thesis is Innova AFM developed by Veeco Instruments.

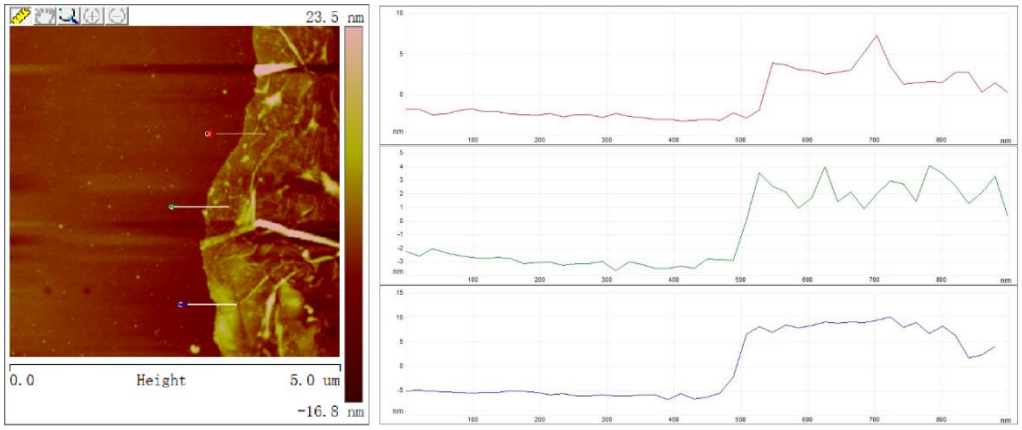

Figure 2-6 The morphology of the CVD graphene measured by AFM.

As shown in Figure 2-6, the graphene film transferred to the SiO_2/Si substrate was scanned by AFM. The selected area is the edge part of graphene, where graphene and substrate form obvious steps, which is convenient to measure the thickness of graphene. The graphene sample is monolayer that has been confirmed by Raman spectroscopy. Theoretically, the thickness of single-layer graphene is about 1 nm, but the height difference between graphene and substrate is about 5 nm, as shown in Figure 2-6, and it is close to 10 nm in the thicker region. It shows that the residual PMMA on the surface of graphene cannot be completely removed even after three times of acetone immersion treatment.

2.3 Fabrication and characterization of metal-graphene-metal photodetector

2.3.1 Fabrication of metal-graphene-metal photodetector

In order to verify the photoelectric detection capability of the as-prepared graphene, the metal-graphene-metal (MGM) structure was fabricated, as shown in Figure 2-7, and its photoelectric response was tested with a 532nm light source.

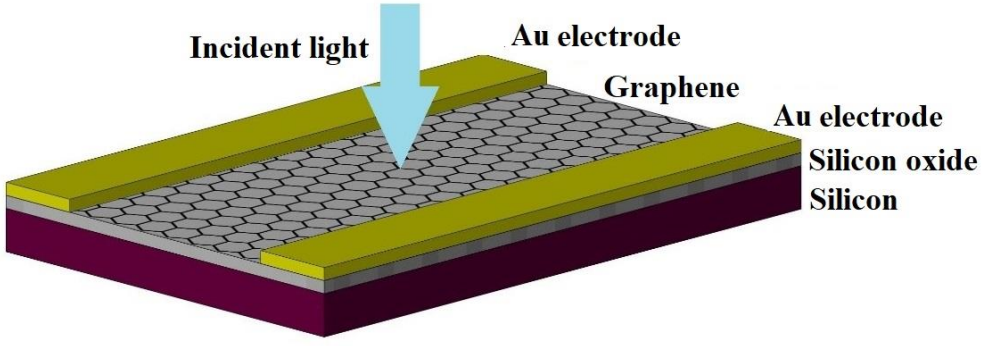

Figure 2-7 The schematics of metal-graphene-metal structure

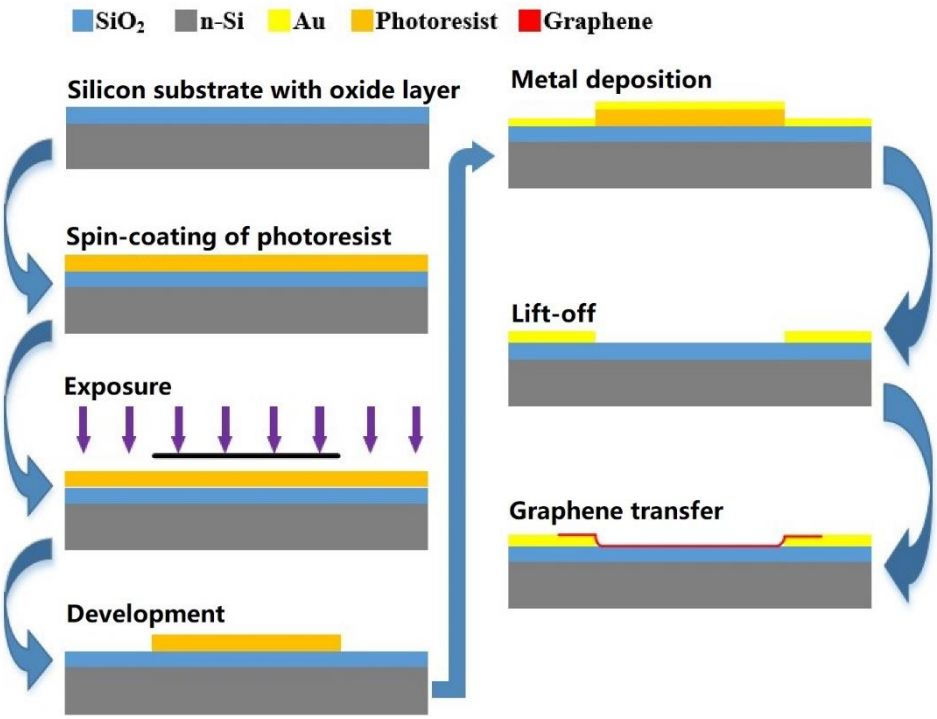

Figure 2-8 The fabrication process of metal-graphene-metal structure

The detailed fabrication process is as follows:

1) Preparation. SiO_2/Si (n-type heavily doped, 300 nm thick oxide layer) was used as substrate. The surface was cleaned by ultrasonic treatment sequentially in isopropanol, acetone and deionized water for 15 minutes for each, and then dried by nitrogen.

2) Spin coating. The positive photoresist (EPG535) was spin coated on the surface of the sample. The spin coating speed and time were 500 rpm for 5 seconds followed by 2500 rpm for 40 seconds. Then the sample was placed on a hot plate at 85 ℃ for 5 minutes to perform soft bake.

3) Lithography. The mask aligner (ABM6/350NAV13SV/M) was used to carry out the lithography. The mask with interdigital electrode pattern was placed on the sample, and the sample was exposed by UV light for 7 seconds.

4) Development. The exposed sample was developed with 0.5% NaOH solution for about 15 seconds. The photoresist in the exposed area dissolved in the solution, thus the pattern transferred from the mask to the sample.

5) Metal deposition. Au thin film with the thickness of 100 nm was deposited on the sample by magnetron sputtering system (explorer 14, Denton vacuum).

6) Lift-off. The sample was immersed in acetone for 4 hours to remove the photoresist layer and the metal film adhered on the photoresist. In the area without photoresist, the Au thin film directly contacts with the substrate so as to be retained.

7) Graphene transfer. The CVD graphene film was transferred to SiO_2/Si substrate with the assistance of PMMA temporary support layer. The transfer process is the same as the subsection 2.2.2. Finally, the metal-graphene-metal structure was obtained, as shown in Figure 2-8.

Multi-finger electrodes are used to increase the contact area between graphene and metal. As shown in Figure 2-9, the gap and width of interdigital electrodes are 80 μm and 20 μm, respectively. The electrodes on both sides connects with the 3mm × 3mm contact pads, and the conductive silver paste is used for external lead. In graphene-metal contact photodetector, the photocurrent mainly originates from the metal-graphene interfaces, where charge transfer between the metal and graphene leads to band bending. This built-in electric field is responsible for the separation of the photo-generated carriers. Multi-finger electrodes increase the area of metal-graphene interfaces, which leads to enlarged light-detection region.

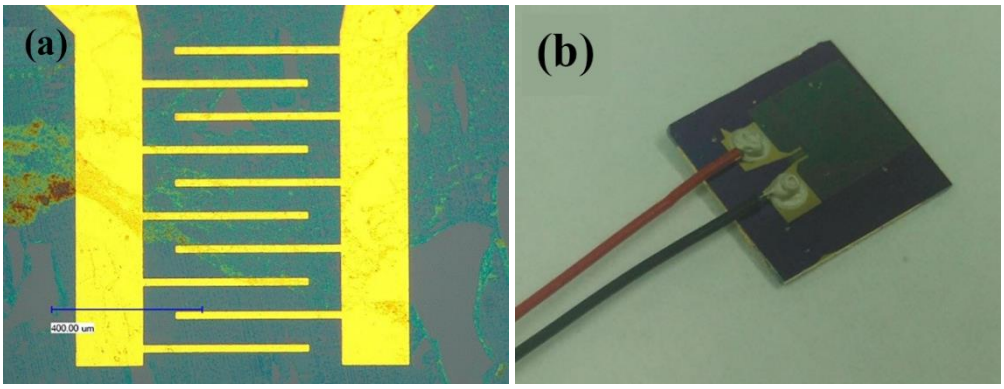

Figure 2-9 The configuration and photograph of the metal-graphene-metal structure. (a) The configuration of the interdigital electrodes. (b) The photograph of the metal-graphene-metal structure

2.3.2 Characterization of metal-graphene-metal photodetector

Current–voltage (I–V) and current-voltage-time (I-V-t) measurements were performed using a semiconductor device analyzer (Keysight B1500A) and 532 nm laser. The typical room-temperature I–V and I-V-t characteristics of the metal-graphene-metal photodetector under dark and illuminated conditions at 532 nm are depicted in Figure 2-10, the power of incident light is 25 mW. The fabricated photodetector shows linear behaviour, suggesting that the contact between Au electrodes and monolayer graphene is ohmic contact. When the bias voltage between the electrode is 3 V, the photocurrent is ~0.1mV, and the responsivity of this multi-finger metal-graphene-metal photodetector is 4mA/W.

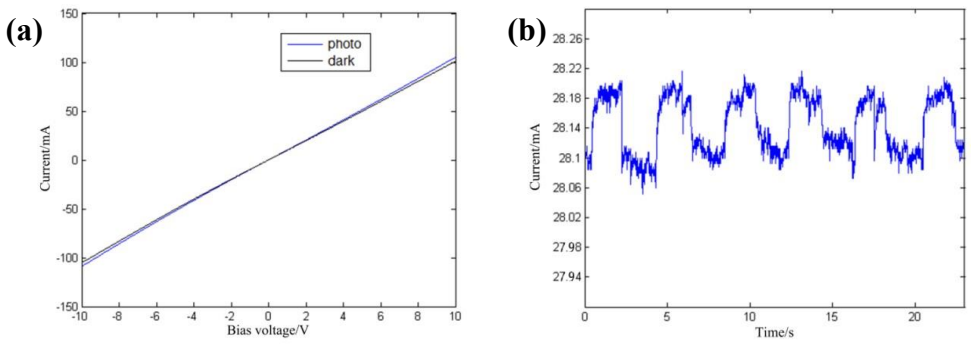

Figure 2-10 The photoelectrical response of metal-graphene-metal structure. (a) I-

V characteristics in dark and under illumination. (b) The photoresponse to periodic light signal.

The photocurrent originates from photovoltaic effect. When the metal contacts with graphene, due to the different work functions (graphene is 4.6 eV, gold is 5.1 eV), electrons flow from graphene to gold until they reach new equilibrium, and form a built-in potential field from graphene to gold. Under the action of built-in electric field, the electron hole pairs excited by incident photons are separated to form photocurrent. Figure 2-11 shows the energy band diagram of graphene between two neighboring fingers. When there is no bias voltage applied to the detector, the built-in electric field profile in the channel between two neighboring fingers is symmetric, and the two junctions have the same properties and represent symmetric photocurrent, thus the total photocurrent is zero. When applying a bias voltage on the detector, the symmetric built-in electric field is broken, which leads to asymmetrical photocurrent in two neighboring graphene-metal junctions, thus the detector produce photocurrent under bias voltage, which is consistent with the previous test results.

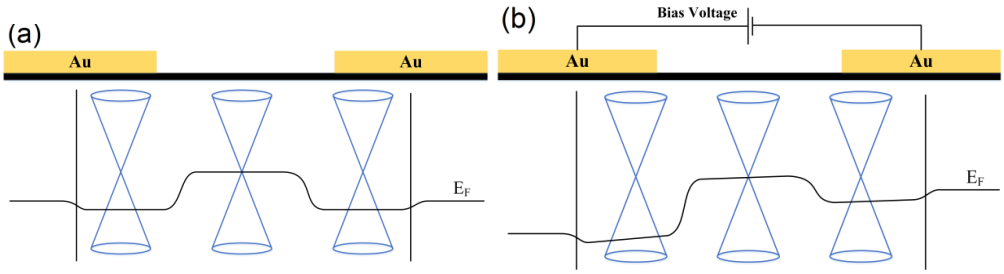

Figure 2-11 The energy band diagram of the metal-graphene-metal structure. (a) without bias voltage and (b) with bias voltage.

In summary, we synthesized monolayer graphene on Cu foil by CVD, and fabricated metal-graphene-metal multi-finger photodetector based on the transferred graphene on SiO_2/Si substrate. The responsivity of this detector is 4mA/W under a bias voltage of 3V. However, the metal-contact graphene photodetector is a nonjunctional device, the dark current increases linearly with the bias voltage. The low light absorption of graphene also limits the responsivity and on/off ratio of the photodetector. The following content of this thesis mainly focuses on the graphene/silicon Schottky photodetector.

2.4 Theoretical basis of graphene/silicon Schottky junction

2.4.1 Formation and working principle of graphene/silicon Schottky junction

Metals and semiconductors have different work functions. The value of work function is the minimum energy required for electrons at Fermi level to jump into vacuum. When metal and semiconductor contact, they will form a unified electronic system, and the interface charges will redistribute. The contact between

metal and semiconductor has two different types, ohmic contact and Schottky contact.

Ohmic contact has very low contact resistance. Ideally, the current of ohmic contact is a linear function of applied voltage. Semiconductor device ultimately needs to use metal to contact with it and lead out through the metal wire, so it is very necessary to obtain good ohmic contact in this circumstance. For n-type semiconductor, it needs metal materials with smaller work function to form ohmic contact. In the graphene/silicon photodetectors fabricated in this thesis, Ti/Au thin film were deposited on the back of the substrate to form contact with silicon, which was used as the back electrode of the device.

In contrast, in Schottky contact, the bending of semiconductor band at the interface forms Schottky barrier, which makes it have nonlinear impedance characteristics (rectification characteristics). For n-type semiconductor, if its work function is less than that of the metal material in contact with it, electrons flow from the semiconductor to the metal, and form a space charge region composed of donor impurity ions with positive charges near the contact interface. In the space charge region, there is an electric field from the semiconductor to the interface, which will cause the band bending and form the built-in potential between the semiconductor and the metal. The existence of the built-in potential prevents the further flow of electrons and makes the electronic system eventually become electrically neutral.

The formation process of graphene/silicon Schottky junction is shown in Figure 2-12. Before silicon and graphene contact, the Fermi energy level of silicon is higher than that of graphene. When they contact to each other, the electrons in silicon flow to graphene, make the Fermi energy level of both reach new thermal equilibrium, and form a space charge region composed of positively charged and immovable impurity ions on the surface layer of silicon, also known as depletion layer. The height of the Schottky band Φ_B is determined only by the Fermi level height of graphene Φ_G and the Si electron affinity energy χ.

$$\Phi_B = \Phi_G - \chi \tag{2-2}$$

After reaching the new thermal equilibrium, there is a potential barrier in the space charge region, which prevents the further flow of electrons form silicon to graphene. The built-in potential of Schottky junction can be calculated by the following equation,

$$V_{bi} = \Phi_B - \Phi_n \tag{2-3}$$

where Φ_n is the potential difference between Fermi level and conduction band of n-type doped silicon.

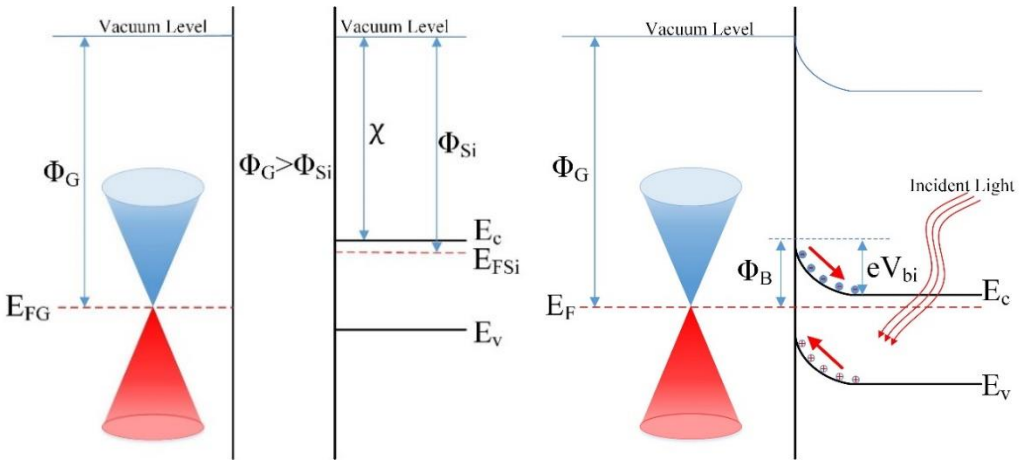

Figure 2-12 The energy band diagram of the graphene/n-Si contact.

The performance of graphene/silicon Schottky photodetectors is strongly influenced by the built-in potential. Unlike metal-contact graphene photodetectors that have many mechanisms such as photovoltaic effect, photothermoelectric effect and radiative heat effect, the response of graphene/silicon Schottky photodetectors to incident light is dominated by photovoltaic effect. In the presence of incident light, the Gr/Si Schottky junction absorbs the incident photons and excites electron hole pairs. Due to the weak interaction between graphene and incident light, the theoretical light absorbance of monolayer graphene is only 2.3%, so the light absorption mainly occurs in silicon part. The photogenerated electron hole pairs are separated under the action of built-in potential and flow to graphene and silicon respectively, thus generating photoelectric response signals in the external circuit. When the external circuit is open circuit, the photovoltage response can be obtained; when the external circuit is short circuit, the photocurrent response can be obtained.

After applying a bias voltage on the Gr/Si Schottky junction, the Fermi levels of graphene and silicon are no longer same, and the difference between them is equal to the potential difference caused by applied voltage. As shown in Figure 2-13, in the circumstance of forward bias, the height of built-in potential in silicon decreases, and electrons as majority carriers are easier to flow from silicon to graphene, thus forming a net current in the electrical circuit, which increases with the increase of bias voltage. For reverse bias, the height of built-in potential in silicon increases, which prevents electrons from flowing from silicon to graphene. At this time, a few electrons with higher energy in graphene can cross the Schottky barrier and flow into silicon, forming reverse current. The reverse current is smaller than the forward bias current, which makes the Schottky junction shows rectification characteristics.

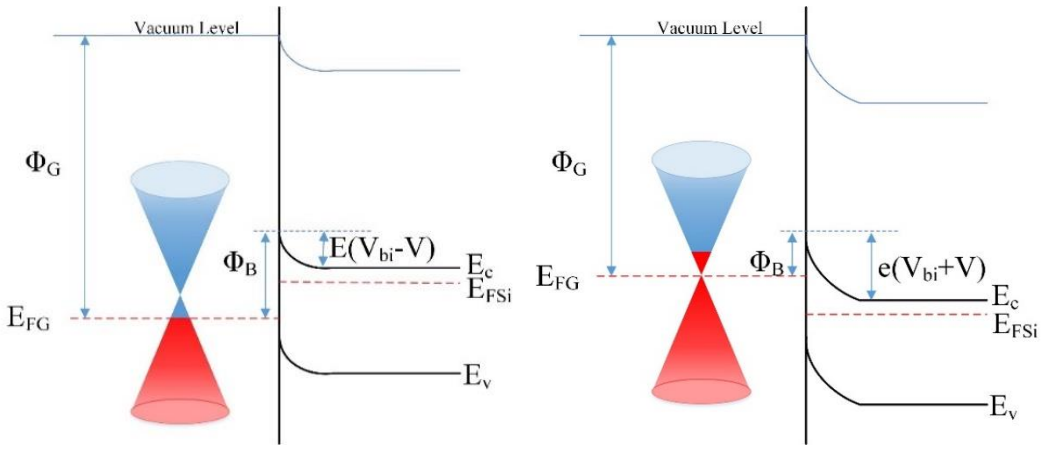

Figure 2-13 The energy band diagram of graphene/silicon Schottky junction with forward bias and reverse bias.

2.4.2 Electrical properties of graphene/silicon Schottky junction

The electrical properties of Schottky junction can be described by two different theories. When the mean free path of electrons is far less than the barrier width, multiple collisions will occur when electrons pass through the barrier region. For such a thick barrier, the diffusion theory is more applicable. The Poisson equation of space charge region is as follow,

$$\frac{d^2V}{dx^2} = \begin{cases} -\frac{qN_D}{\varepsilon_r\varepsilon_0}, & (0 \le x \le x_d) \\ 0 \quad , & (x > x_d) \end{cases} \tag{2-4}$$

where V is the electric potential, x is the distance from the interface, q is electron charge, N_d is the doping concentration of semiconductor, ε_r and ε_0 are the relative permittivity and vacuum permittivity, respectively, and x_d is the width of depletion layer. Considering the diffusion current and drift current, the current density of the diffusion model is as follow,

$$J = qn_0\mu_0\sqrt{\frac{2qN_D}{\varepsilon_r\varepsilon_0}(V_D - V)}e^{-\frac{q\Phi_B}{kT}}\left(e^{\frac{qV}{kT}} - 1\right) \tag{2-5}$$

where n_0 is electron concentration, μ_0 is vacuum permeability, V_D is built-in potential of semiconductor, K is Boltzmann constant, T is Kelvin temperature. Base on this equation, the total current density is related to the applied bias voltage. The current changes with the voltage under reverse bias, but it will not saturate.

On the contrary, when the mean free path of electrons is much larger than the barrier width, the collision of electrons in the barrier region can be ignored. The shape of the barrier will no longer affect the electrons, while the height of the barrier is the decisive factor. As long as the electrons in the semiconductor have enough energy to surmount the potential barrier, they can enter the metal freely. Similarly, the electrons with enough energy in the metal can also cross the barrier and enter the semiconductor. Based on this theory, the current of Schottky junction is related to the energy distribution of electrons in the junction. The current can be obtained by calculating the number of carriers that cross over the

potential barrier. The relationship between the number of electrons N and the energy E is as follow,

$$dn = 4\pi \left(\frac{\sqrt{2m_n^*}}{h}\right)^3 \sqrt{E - E_c} e^{-\frac{E-E_F}{kT}} dE \tag{2-6}$$

where m_n^* is the effective mass of the electron at the bottom of the band, and h is Planck constant. By integrating the number of electrons per unit volume whose energy ranges from the height of the barrier to infinity, the current density based on thermal emission theory is as follow,

$$\mathrm{J} = A^* T^2 e^{-\frac{q\Phi_B}{kT}} \left(e^{\frac{qV}{kT}} - 1\right) \tag{2-7}$$

where A* is the effective Richardson constant. From this equation we can know that, when the Schottky junction is under reverse bias, the current tend to saturation with the increase of bias voltage, and the saturation current density is independent of the applied bias voltage, its value is more temperature dependent.

For Si, Ge, GaAs and other semiconductor materials with high carrier mobility, when they contact with metal and form Schottky junction, the mean free path of electrons is much larger than the barrier width due to the high mobility. The thermal emission theory is better suited to describe the carrier transport process. It is generally believed that at low voltage, the dark current of Schottky junction conforms to the thermal emission model, and the current equation of ideal Schottky diodes without any defects is as follow [143-147]:

$$\mathrm{I} = \mathrm{I}_0 \left(e^{\frac{qV}{kT}} - 1\right) \tag{2-8}$$

where q is electron charge (1.6×10^{-19} C), K is the Boltzmann constant (1.3806505×10^{-23} J/K), T is the Kelvin temperature, and I_0 is the reverse saturation current,

$$I_0 = AA^* T^2 e^{-\frac{\Phi_B}{kT}} \tag{2-9}$$

where A is the junction area, for the Gr/Si Schottky junction detector fabricated in this chapter, the value is 2.56 mm^2; Φ_B is the Schottky barrier height at zero bias; A* is the Richardson constant, the value for n-type silicon is 112 $A\cdot cm^{-2}\cdot K^{-2}$. In practical Schottky junctions, the influence of surface effect and barrier recombination current need to be taken into account, and the equation is modified as:

$$\mathrm{I} = \mathrm{I}_0 \left(e^{\frac{qV}{\eta kT}} - 1\right) \tag{2-10}$$

where η is the ideal factor of Schottky junction. When the forward bias V>3kT/q, the equation (2-10) can be approximated as:

$$\mathrm{I} = \mathrm{I}_0 e^{\frac{qV}{\eta kT}} \tag{2-11}$$

Taking the natural logarithm of it, we can get the following equation:

$$\ln(\mathrm{I}) = \ln(\mathrm{I}_0) + \frac{qV}{\eta kT} \tag{2-12}$$

Through the linear fitting of ln(I)-V curve, the ideal factor and reverse saturation current of Schottky junction can be extracted from the slope and intercept of the fitting line respectively, and the Schottky barrier height can be further calculated by equation (2-9).

Due to the joint influence of interface defects and other factors, the I-V characteristic curve of Gr/Si Schottky junction will deviate from the ideal model under higher forward bias voltage, and the results obtained by linear fitting of curves in different ranges will be different. According to the Cheung's functions, the series resistance, ideal factor and Schottky barrier height of Gr/Si Schottky junction can be extracted from the I-V characteristic curve [148]. Considering the influence of series resistance R_s and ideal factor η on the Schottky junction, the ideal diode equation can be modified as:

$$\mathrm{I} = \mathrm{I}_0 \left(e^{\frac{q(V - R_S I)}{\eta kT}} - 1 \right) \tag{2-13}$$

Take approximation, logarithm and differential of it, we can get the following equation:

$$\frac{\mathrm{dV}}{\mathrm{d(lnI)}} = \frac{\eta kT}{q} + \mathrm{R_s I} \tag{2-14}$$

After calculating and plotting dV/dlnI - I curve, the series resistance R_s and ideal factor η of Schottky junction can be extracted from the slope and intercept of the linear fitting of the curve. Cheung's functions also define the equation:

$$\mathrm{H(I)} = \mathrm{IR}_s + \eta \Phi_B \tag{2-15}$$

The value of H(I) can be calculated by the following formula:

$$\mathrm{H(I)} = \mathrm{V} - \eta(\frac{kT}{q})\ln(\frac{I}{AA^*T^2}) \tag{2-16}$$

After calculating and plotting H(I) - I curve, the series resistance R_s and Schottky barrier height Φ_B of Schottky junction can be extracted respectively from the slope and intercept of the linear fitting of the curve.

Furthermore, another method proposed by Norde for the determination of R_s and Φ_B values [149]. The modified function of this method is defined as

$$F(V) = \frac{V}{\gamma} - \frac{k_B T}{q}\ln(\frac{I}{AA^*T^2}) \tag{2-17}$$

where γ is the first integer number greater than ideal factor η. The barrier height of Schottky diode is given by:

$$\Phi_b = F(V_{\min}) + \frac{V_{\min}}{2} - \frac{k_B T}{q} \tag{2-18}$$

where $F(V_{min})$ is the minimum value taken from the plot of F(V) - V, and V_0 is the corresponding voltage. In conclusion, the three methods of thermal emission equation, Cheung's function and Norde's function can be used to extract the key characteristic parameters of Gr/Si Schottky junction to evaluate its property.

2.5 Fabrication and characterization of graphene/silicon Schottky photodetector

2.5.1 Fabrication of graphene/silicon Schottky photodetector

Due to the half-metallic behavior of graphene, the dark current of photodetectors based on metal-graphene contact is relatively large, which affects the performance of photodetectors. In this subsection we use graphene and n-type silicon to fabricate Schottky photodetector, as shown in Figure 2-14. When reverse bias is applied, the built-in potential height increases, which suppresses the dark current and promotes the separation of photogenerated carriers. Therefore, the Gr/Si Schottky junction photodetector has relatively high responsivity and on/off ratio.

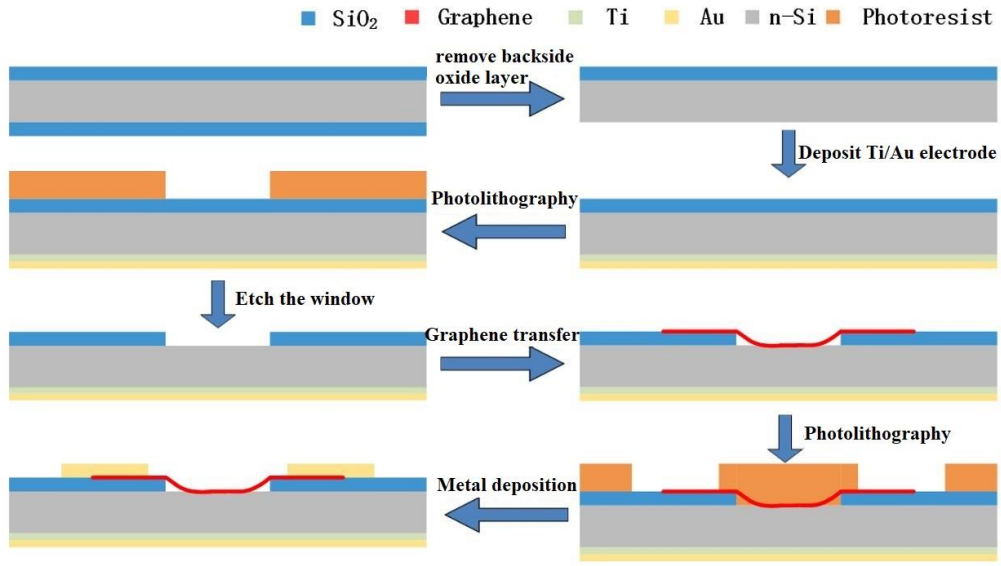

Figure 2-15 The fabrication process of Gr/Si Schottky photodetector

The detailed fabrication process is as follows:

1) Synthesis graphene, the process is the same as above.

2) Deposition of ohmic contact electrode on the backside. Ti with smaller work function (4.33 eV) is used to form ohmic contact with n-type Si on the back. The utilized substrate was double-side oxidized and front-side polished silicon wafer. The oxide layer on the backside was removed by 40% HF solution, and then Ti/Au (20nm/80nm) was deposited on the back by electron beam evaporation.

3) Patterning of silicon window. A square area of 1.6mm×1.6mm was obtained by UV lithography. The process of spin coating, soft baking, exposure and development in lithography are same as foregoing paragraphs.

4) Fabrication of silicon window. The sample was put into buffer oxide etching solution (BOE, 49% HF aqueous solution: 40% NH_4F aqueous solution = 1:6) to etch the silicon oxide layer in the exposed square area.

5) Transfer of graphene. After removing the residual photoresist by acetone, graphene was transferred to the square window in the same way as before.

6) Patterning of front side electrode by lithography. The shape of the front electrode is a square frame with the inner side length of 1.8 mm and the outer side length of 2.2 mm, which surrounds the silicon window. The process of spin coating, soft baking, exposure and development in lithography are same as foregoing paragraphs.

7) Fabrication of front side electrode. Au thin film with 100 nm thickness was deposited by electron beam evaporation, and then the photoresist and Au adhered to the photoresist were removed by acetone.

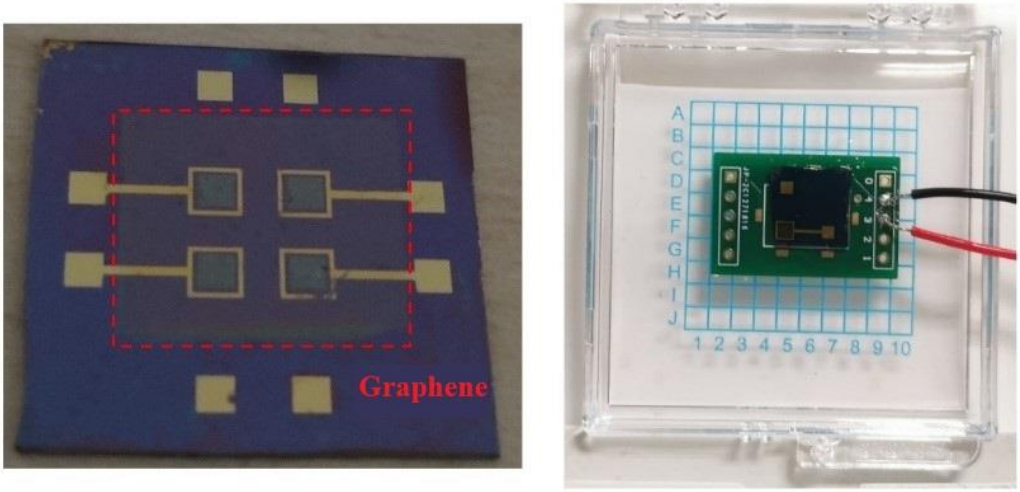

Figure 2-16 The fabricated Gr/Si Schottky photodetectors. (a) Photograph of the photodetector. (b) Photoelectrical characterization layout on a PCB test board.

2.5.2 Characterization and analysis of graphene/silicon Schottky photodetector

The photoelectric response of the Gr/Si photodetector were tested by a semiconductor device analyzer (keysight B1500A). The sample and the analyzer were connected by a probe station, and a 633nm laser was used as the incident light source.

Figure 2-17 shows the current-voltage response curves of the Gr/Si Schottky photodetector at room temperature under dark and illumination, where the incident light power density is 160 mW/cm^2. From the figure, we can see that the open circuit voltage (V_{oc}) of the detector under illumination is 0.25 V, and the photocurrent of the detector under zero bias (I_{sc}) is 20.7 μA. As the reverse bias voltage increases, the photocurrent response of the detector increases. The dark current of the detector is 256 nA and the photocurrent increases to 0.94 mA under 2 V reverse bias voltage. Based on equation (1-3) and equation (1-15), the photocurrent responsivity of the detector is 0.23 A/W and the on/off ratio is 3.7 × 10^3. The relevant performance parameters of Gr/Si photodetectors are summarized in Table 2-1.

Table 2-1 The performance parameters of Gr/Si Schottky photodetector

Structure	V_{oc} (V)	I_{sc} (μA)	I_d (nA)	I_{ph} (mA)	R (A/W)	$r_{on/off}$
Gr/Au	0.25	20.7	256	0.941	0.23	3.7×10^3

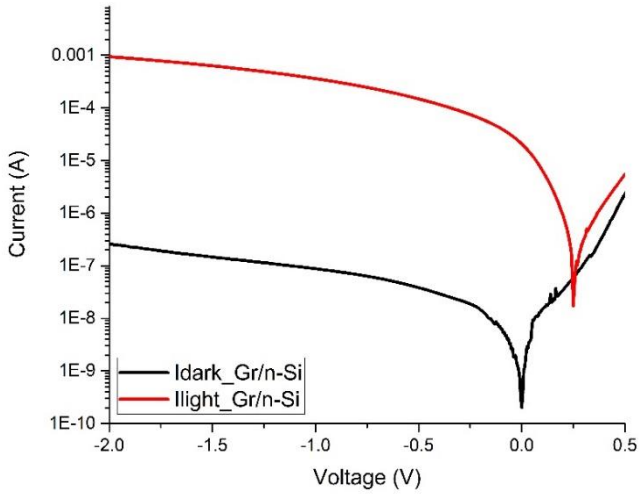

Figure 2-17 The I-V characteristics of Gr/Si Schottky photodetector

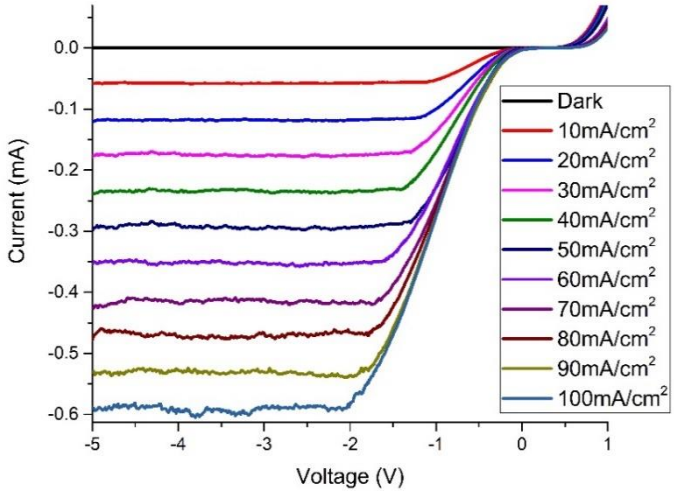

Figure 2-18 The I-V curves of Gr/Si Schottky photodetector under various incident light power intensity.

The I-V curves of the Gr/Si Schottky photodetector under various power density of incident was measured by changing the supply voltage of the semiconductor laser to adjust its output light power. As shown in Fig. 2-18, as the optical power density increases from 0 to 100 mW/cm^2, the photocurrent of the detector also increases with good linearity, and the detector has a stable response in a wide range of optical power. For a certain incident light power density, when the reverse bias voltage is low, the photocurrent of the detector increases rapidly with the increase of the reverse bias voltage, and tends to a stable value when the bias voltage is high. This is because the height of the built-in potential of the Gr/Si Schottky junction is directly related to the applied bias voltage. The built-in

potential can be increased by adjusting the applied bias voltage. When the built-in potential field is powerful enough that almost all the photogenerated carriers are separated and flow to graphene and silicon respectively, the photodetector reaches saturation current.

A mechanical chopper is used to generate periodic pulse light signal, which is utilized to measure the response speed of Gr/Si photodetector, and the current response of the detector is recorded by the semiconductor device analyzer (Keysight B1500A). The wavelength of the light source is 633nm, the optical power density is about 100mW/cm^2, and the sampling interval of the semiconductor device analyzer is 100 μs. As shown in Figure 2-19, the Gr/Si photodetector has a stable response to the incident light signal and shows good repeatability in multiple pulse cycles. The response time of the detector can be obtained from the figure. The rise time and fall time are both about 1 ms, which is in the same order of magnitude as that of the similar devices reported in the literature [125].

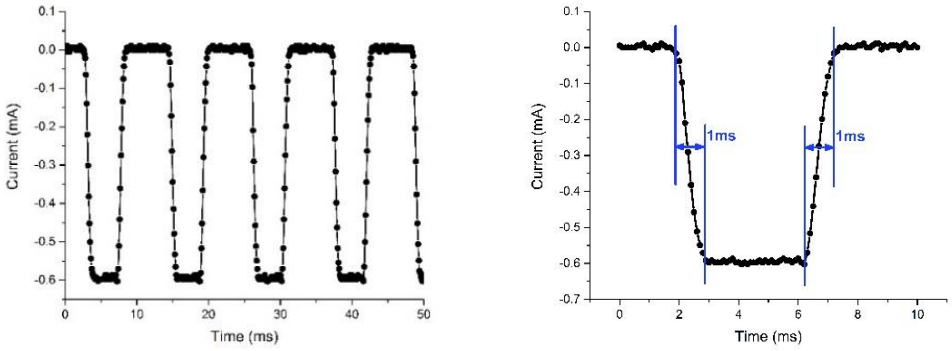

Figure 2-19 The photoreponse of Gr/Si Schottky photodetector. (a) Photoresponse to periodic light signal. (b) Rise time and fall time.

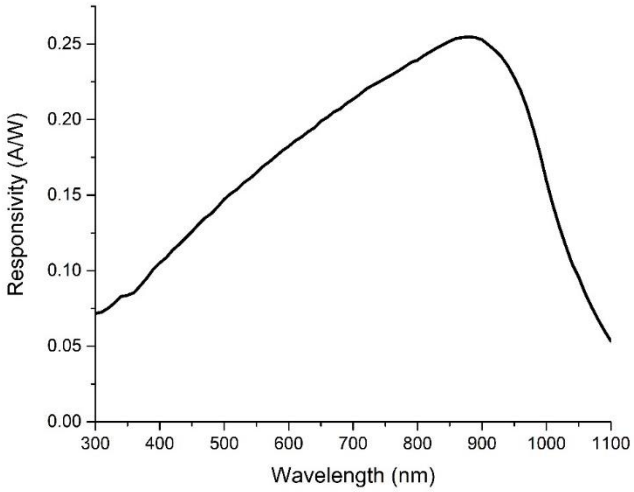

Figure 2-20 The spectral response of Gr/Si Schottky photodetector

A Xenon lamp (Spectral Products, ASB-XE-175-BFEX) combined with a monochromator (Spectral Products, CM110) was used to generate the output light

with the wavelength of 300 nm ~ 1100 nm, and the spectral response of the Gr/Si Schottky photodetector was measured. The source measure unit (Keithley 2450) is connected with the photodetector through the probe station to apply bias voltage and record the current flow of the detector. As shown in Figure 2-20, the responsivity of the detector reaches the maximum at about 880 nm, and there is an obvious cut-off at 1100 nm, which proves that the absorption of incident light is mainly carried out by silicon in the Gr/Si Schottky photodetector.

As shown in Figure 2-21, we calculate and plot the semi-log current-voltage curve of Gr/Si photodetector in dark, as well as its linear fitting. The slope and intercept of fitting line are 16.89 and -21.43, respectively. Based on the thermal emission theory, the ideal factor η, reverse saturation current I_0 and Schottky barrier height Φ_B of Gr/Si detector can be calculated as 2.29, 4.93×10^{-10} A and 0.88 eV respectively from equation (2-9) and equation (2-12).

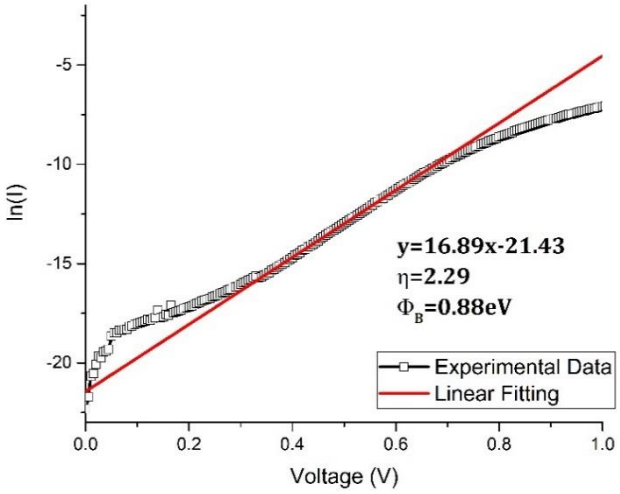

Figure 2-21 The semilogarithmic I-V curves of Gr/Si Schottky photodetector

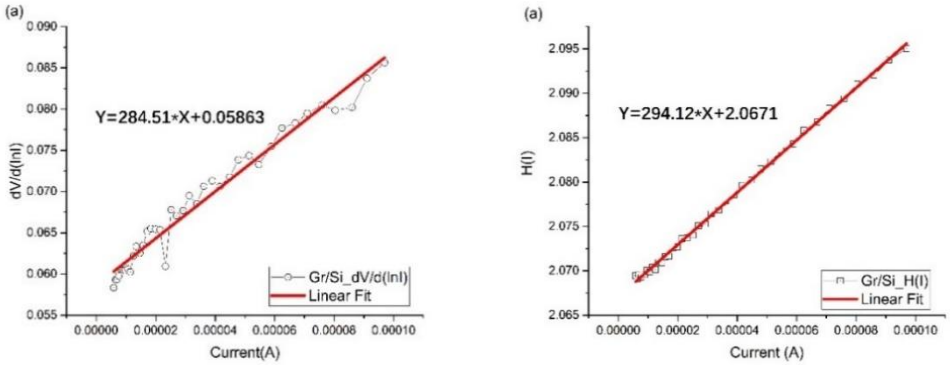

Figure 2-22 The dV/dlnI - I and H(I) - I curves of Gr/Si Schottky photodetector

Based on Cheung's function, we calculate and plot the curves of dV/dlnI - I curve and H(I) - I, as well as their linear fitting. The series resistance, ideal factor and Schottky barrier height of Schottky junction can be extracted from the slope and intercept of fitting line by equation (2-14) and equation (2-15). As shown in

Figure 2-22 (a), the slope and intercept of dV/dlnI - I fitting line are 285 and 0.05863, respectively. The series resistance R_s of Gr/Si Schottky junction is 285 Ω, and the ideal factor η is 2.26. As shown in Figure 2-22 (b), the slope and intercept of the H (I) - I fitting line are 285 and 0.05863, respectively. The series resistance R_s of the Gr/Si Schottky junction is 294 Ω, and the Schottky barrier height Φ_B is 0.91 eV.

Based on Norde's function, we calculate and plot the F(V) - V curve of Gr/Si Schottky junction by equation (2-17), as shown in Figure 2-23. When the bias voltage is 0.055 V, function F(V) reaches the minimum value of 0.8537, and the barrier height of Gr/Si Schottky junction can be calculated as 0.86 eV by equation (2-18).

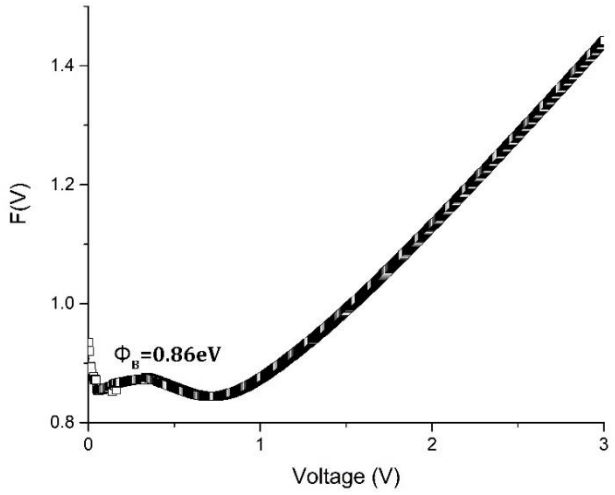

Figure 2-23 The F(V)-V curve of Gr/Si Schottky photodetector

There are some differences between the key parameters of Gr/Si Schottky junction extracted by the three methods of thermal emission equation, Cheung' function and Norde's function, the reason is that they use different data segments for calculation [150]. As shown in Figure 2-24, the logarithmic I-V curve of Gr/Si Schottky junction can be obviously divided into three linear regions. When the forward bias voltage is low (V < 0.3V), the voltage and current have a good linear relationship, and the current transport characteristics of Schottky junction conform to Ohm's law [151]. When the forward bias voltage is slightly higher (0.3 < V < 0.9V), the current increases exponentially with the increase of voltage, which is dominated by space-charge-limited-current (SCLC) conduction mechanism. When the forward bias voltage is larger (V > 0.9V), the slope of I-V curve decreases, and the trap-filling effect strongly influences the current of Schottky junction [153]. In this paper, all of these three methods are used to extract the key parameters of Gr/Si Schottky junction, in order to analyze its performance comprehensively.

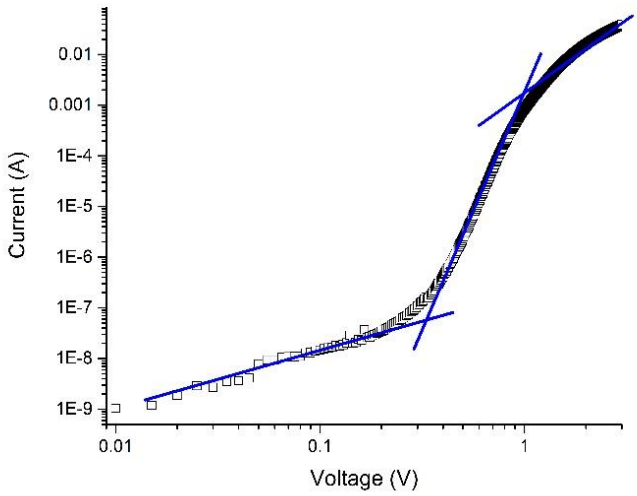

Figure 2-24 The logarithmic I-V curve of Gr/Si Schottky photodetector

2.6 Summary

In this chapter, we synthesized single-layer graphene film by chemical vapor deposition, and PMMA was used as temporary support layer to transfer graphene. Graphene was characterized by Raman spectroscopy, scanning electron microscopy and atomic force microscopy. The results show that graphene is single layer with good integrity and continuity. PMMA remains on the surface of graphene with a thickness of about 5nm. The photoelectric detection performance of graphene was verified by fabricating metal-graphene-metal structure photodetector, its responsivity is about 4 mA/W under the illumination of 532 nm light source, but it suffers from a relatively high dark current, which seriously affects the performance of the detector.

This chapter also analyzes the formation and working principle of Gr/Si Schottky junction theoretically, and introduces three methods of extracting the key parameters of Gr/Si Schottky junction by current-voltage characteristics, which are thermal emission equation, Cheung's function and Norde's function. The fabrication process of graphene/Silicon Schottky junction photodetector is described in detail, and its photoelectric response and spectral response characteristics are tested. The current responsivity of the Gr/Si photodetector is 0.23 A/W and the on/off ratio is 3.7×10^3 for the incident light of 633 nm. The detector responds steadily to the incident light and periodic light pulse signals with different power density, and the response time is about 1 ms. The spectral response shows that the responsivity of the detector reaches the maximum at about 900 nm, and there is an obvious cut-off at 1100 nm, which proves that the absorption of incident light in the Gr/Si Schottky photodetector is mainly carried out by silicon. The ideal factor and Schottky barrier height based on thermal emission equation are 3.44 and 0.82 eV, respectively. The series resistance, ideal factor and Schottky barrier height based on Cheung's function are about 300 Ω,

2.26 and 0.91 eV, respectively. The Schottky barrier height based on Norde's function is 0.86 eV.

Chapter 3

Graphene/silicon Schottky photodetector enhanced by graphene oxide interfacial layer

3.1 Introduction

Graphene has high transparency (monolayer transmittance is 97.7%), and its work function can be tuned by external electric field or chemical doping. Graphene/Silicon Schottky junction provides a good platform for optoelectronic applications, which shows promising prospect compared with traditional metal based Schottky junction devices. However, the responsivity, quantum efficiency and detectivity of Gr/Si Schottky photodetectors are still far behind those of commercial silicon photodetectors. Many researchers are devoted to improve the performance of Gr/Si Schottky photodetector and have proposed many methods as mentioned in the Chapter 1. The insertion of interface layer in Schottky junction is an effective way to enhance the performance of Gr/Si photodetector.

Most of the previously reported graphene/insulator/silicon (GIS) structure Schottky photodetectors use silicon dioxide as insulating layer material, which is due to the mature deposition and growth process of silicon dioxide and its good compatibility with silicon substrate. However, there are few reports on GIS photodetectors using other materials as interlayer [112, 126]. The graphene photodetector based on GIS structure still has the further optimizing space, and its photoelectric detection performance also has the potential to be further improved.

In this chapter, graphene oxide (GO) is utilized as the interlayer of the Gr/Si Schottky photodetector, which can suppress the dark current and increase the photocurrent, so as to further improve the performance of the detector. We fabricate the Gr/GO/Si structure Schottky photodetector and test its photoelectric response and electrical properties. Based on the thermal emission theory and Cheung's function, we compare and analyze the Gr/GO/Si and Gr/Si Schottky

junction, extract the key parameters of Schottky junction from the I-V characteristic curve, and discusse the influence of GO interlayer on the performance of the Schottky photodetector.

3.2 Fabrication of graphene oxide enhanced graphene/silicon Schottky photodetector

3.2.1 Synthesis and pre-transferring of graphene

In this paper, the Gr/Si Schottky photodetectors are fabricated by CVD graphene on silicon substrate. The CVD process of graphene synthesis and the transfer process by using PMMA temporary support layer have been introduced in Chapter 2. Here we use the same methods as above. After the copper foil substrate was etched, the PMMA/graphene structure was obtained for the fabrication of photodetector.

3.2.2 Preparation of graphene oxide thin film

Graphene oxide thin films were prepared by drop coating. Graphene oxide powder (purchased from XFNANO) was dissolved in deionized water to obtain 0.03 mg/ml GO solution, which was used for the interlayer of photodetector, and the diluted GO solution with concentration of 0.002 mg/ml was prepared for the measurement of GO thickness by AFM.

3.2.2 Fabrication of the photodetector

Graphene oxide thin films were prepared by drop coating. Graphene oxide powder (purchased from XFNANO) was dissolved in deionized water to obtain 0.03 mg/ml GO solution, which was used for the interlayer of photodetector, and the diluted GO solution with concentration of 0.002 mg/ml was prepared for the measurement of GO thickness by AFM.

SiO_2/Si substrate (n-type doping, <100> orientation, resistivity of 1~10 Ω cm, oxide thickness of 300 nm) was utilized to contact with graphene to construct Schottky photodetector, the process is shown in Figure 3-1.

Firstly, the silicon dioxide layer on the backside of the wafer was removed by HF etching, followed by the deposition of Ti/Au (20nm/80nm) by e-beam evaporation to form ohmic contact. The 1.6 × 1.6 mm window was defined by standard photolithography for graphene contact on the substrate, and the SiO_2 inside the window was etched by HF solution. Then graphene oxide was coated on the window and the prepared PMMA/graphene membrane was transferred onside to form the Gr/GO/Si Schottky contact, the PMMA was removed by rinsing in acetone. After that, photolithography was utilized again to define the pattern of electrodes, followed by electronic beam evaporation to deposit Ti/Au (20/80 nm) as electrodes. We also fabricated the graphene-silicon photodetector without GO interlayer as a control. on process of Gr/GO/Si Schottky junction is

basically the same as that of Gr/Si without go interface layer, only adding the step of dropping graphene oxide film.

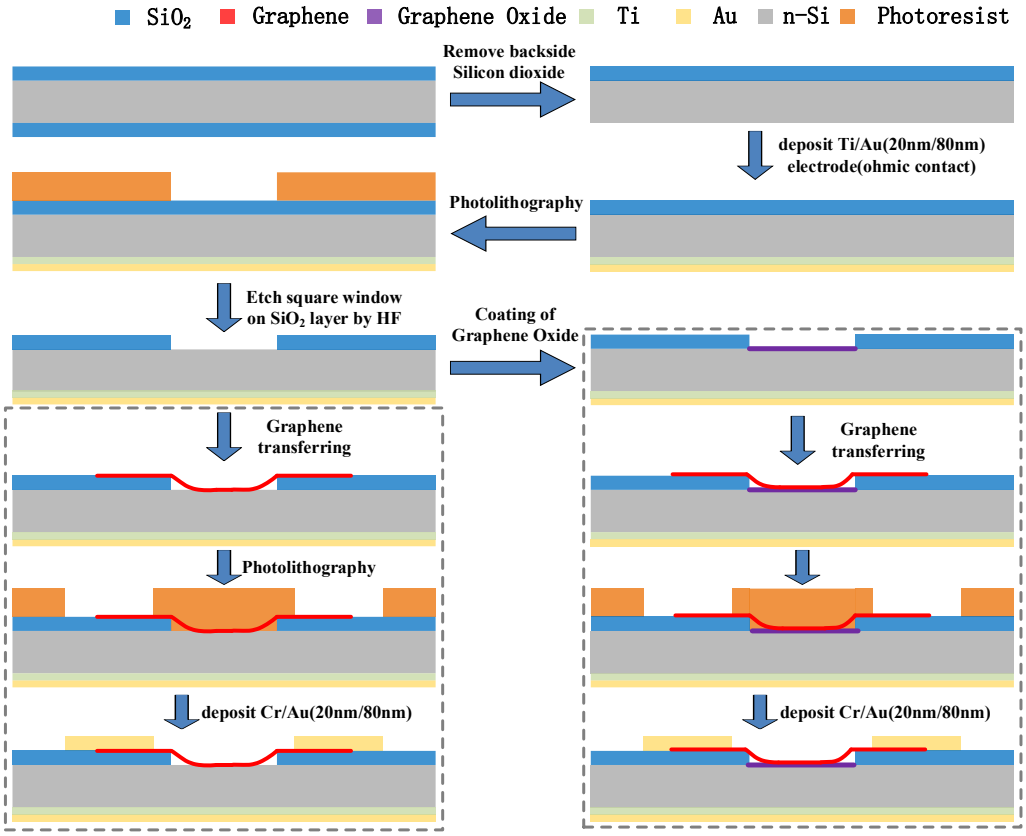

Figure 3-1 Frication process of Gr/Si Schottky photodetector with graphene oxide interlayer (dotted box on the right) and without interlayer (dotted box on the left).

3.3 Characterization and analysis

3.3.1 Characterization of the materials

Raman spectrum is an effective method to characterize graphene films, which can analyze the structure of graphene quickly and non-destructively. The CVD graphene has been characterized by Raman spectrometer in Chapter 2, the 2D peak is a sharp and symmetric Lorentzian line-shape peak with the FWHM of 30 cm^{-1}, and the intensity ratio of 2D peak to G peak is more than 2.5, which indicates that the prepared graphene is single-layer graphene [137, 138]. The SEM images show that there are micro scale wrinkles due to the morphology of copper foil substrate and the transfer process, but it still has good integrity and continuity. The AFM test results show that there are still PMMA residues on the surface of graphene, although it has been soaked in acetone for three times. The thickness of PMMA residues on graphene is about 5nm, which will make graphene slightly p-doped.

The Raman spectrum of graphene oxide is shown in Fig. 3-2. There are two obvious characteristic diffraction peaks near 1345 cm^{-1} and 1590 cm^{-1}, which are D peak and G peak respectively. The D peak originates from the lattice vibration away from the center of Brillouin zone, and its intensity can be used to evaluate the structural disorder of GO. The G peak originates from the first-order E_2G

phonon plane vibration in the center of Brillouin zone, which is the characteristic peak of crystal carbon and represents the content of sp^2 hybrid components in GO, reflecting the symmetry and order degree of GO. The strong D peak in GO Raman spectrum indicates that the oxidation reaction has a great destructive effect on the graphite structure, resulting in a large degree of defects in the GO crystal structure.

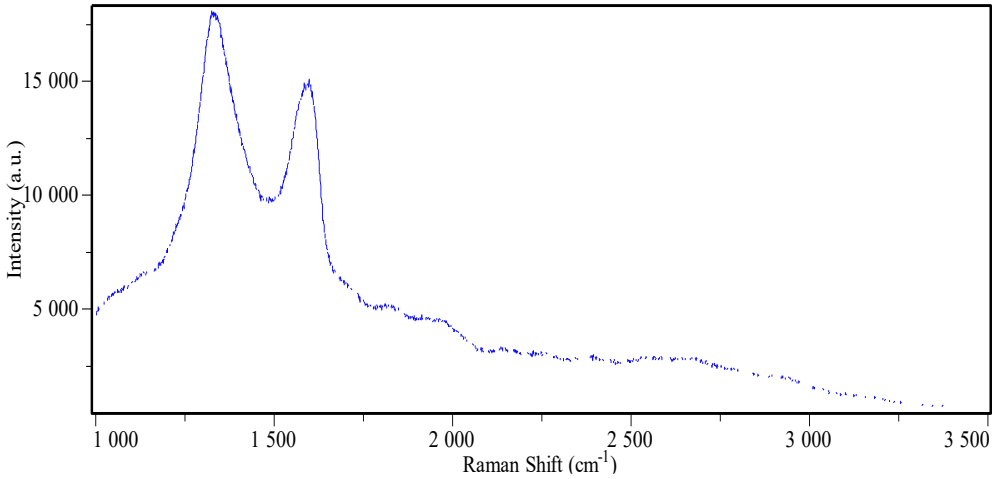

Figure 3-2 Raman Spectrum of graphene oxide

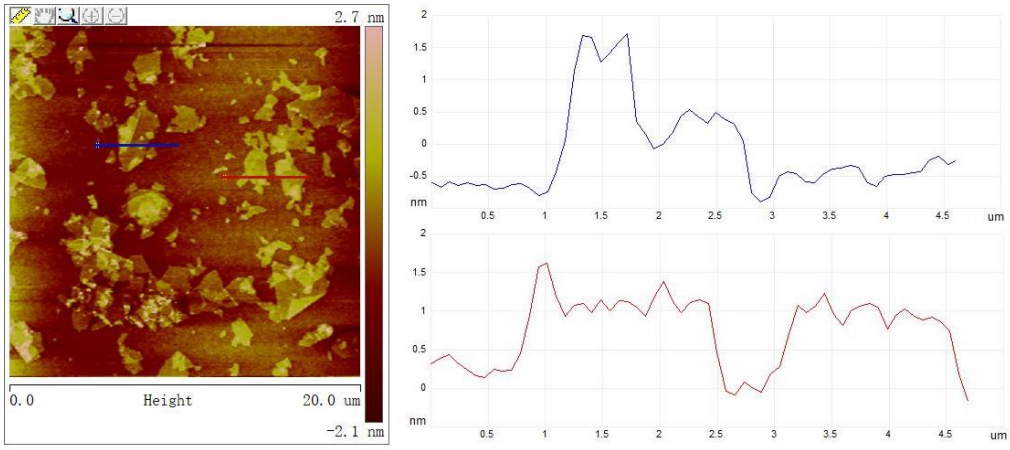

Figure 3-3 AFM image of graphene oxide flakes

For graphene oxide, due to the influence of strong oxidant in the synthesis process, it is rich in a variety of oxygen-containing groups, which makes its Raman spectrum more complex, and it is difficult to identify its layer number. Therefore, AFM is used to directly measure its thickness. In order to show the flake structure of graphene oxide more clearly to measure its thickness and size, the diluted 0.002 mg/mL graphene oxide solution was used to prepare samples for AFM measurement. From Figure 3-3, we can clearly see the flake structure of graphene oxide. The thickness of the single layer is 1.02 nm, indicating the single carbon atom structure, and the flake size is 1 μm ~ 5 μm.

The graphene oxide film as the interlayer in Gr/Si Schottky junction was deposited by drop coating of 0.03 mg/mL graphene oxide solution. As shown in Figure 3-4, flakes of graphene oxide are stacked to form a continuous film with a thickness of about 20 nm. The root mean square roughness Rq and arithmetic mean roughness Ra measured by AFM are 5.57 nm and 3.74 nm, respectively.

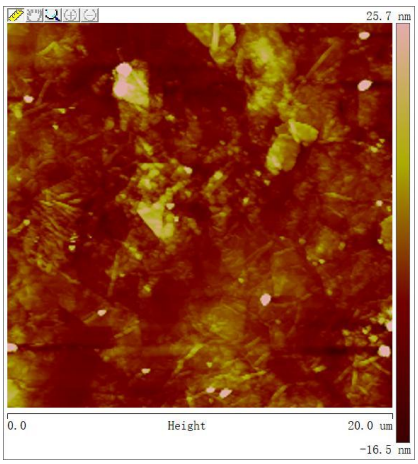

Figure 3-4 AFM image of graphene oxide thin film

Figure 3-5 shows the top view of the photodiode, transferred CVD graphene contacts with n-type silicon through the square window, which is the active photosensitive area, and the gold electrode surrounds this area. The active area of the photodetector is 2.56 mm^2.

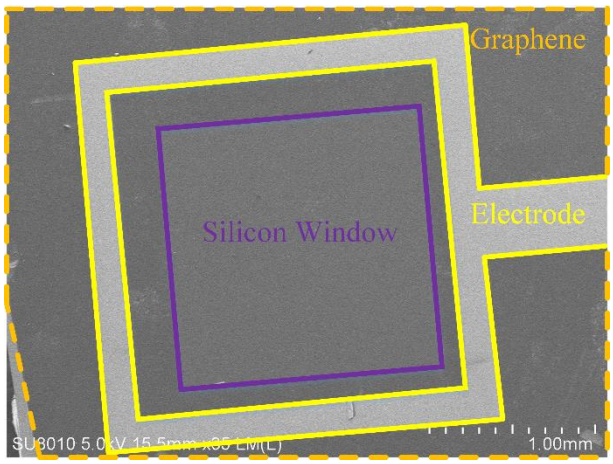

Figure 3-5 Scanning electron micrograph of Gr/Si Schottky photodetector

3.3.2 Measurement and analysis of the photodetectors

Electrical and photoresponse characteristics of the devices were measured using a Keysight B1500A semiconductor device analyzer with probe station under dark and illuminated conditions. The light source was a semiconductor laser with a wavelength of 633nm. Figure 3-6 plots the current-voltage curve of Gr/Si and Gr/GO/Si Schottky photodetector at room temperature under dark and illumination with the incident light intensity of 160 mW/cm^2.

For the Gr/Si Schottky photodetector, the short circuit current is 20.7 μA and the open circuit voltage is 0.25 V. The dark current was 256 nA under a reverse bias voltage of 2V, and the photocurrent is 0.941 mA. According to the equation (1-3) and (1-15), the responsivity and on/off ratio of Gr/Si Schottky were calculated as 0.23 A/W and 3.7×10^3, respectively. After inserting GO interlayer, the short circuit current increased to 224 μA, and the open circuit voltage increased to 0.405 V. Under a reverse bias voltage of 2V, the dark current

decreased to 9.44 nA, and the photocurrent increased to 2.59 mA, thus increased the responsivity to 0.65 A/W. Benefitting from the suppression of dark current and the improvement of photocurrent by GO interlayer, the on/off ratio of Gr/GO/Si Schottky photodetector reached 2.73×10^5.

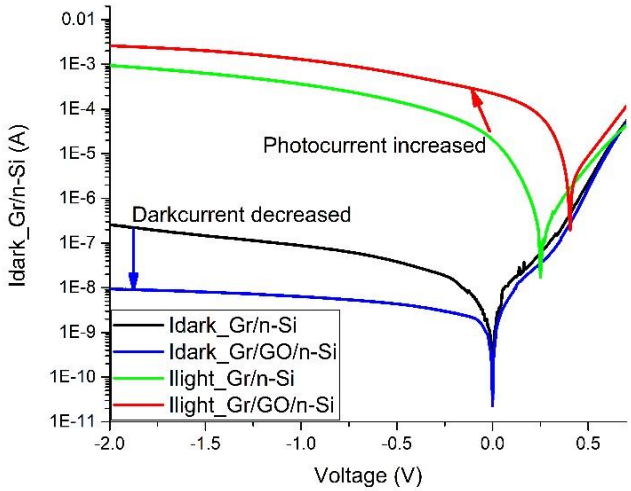

Figure 3-6 The I-V curves of Gr/Si and Gr/GO/Si Schottky photodetector at room temperature under dark and illumination

Table 3-1 The performance paramters of Gr/Siand Gr/GO/Au Schottky photodetector

Structure	V_{oc} (V)	I_{sc} (μA)	I_d (nA)	I_{ph} (mA)	R (A/W)	$r_{on/off}$
Gr/Au	0.25	20.7	256	0.941	0.23	3.7×10^3
Gr/GO/Au	0.405	224	9.44	2.59	0.65	2.7×10^5

We further characterized the current-voltage characteristics of Gr/GO/Si Schottky photodetector under varying incident light power. Figure 3-7 shows the I-V curves of the photodiode under 633nm illumination when the light power intensity increases from 0 to 100 mW/cm^2. The photocurrent increased linearly with the light intensity, which indicates the stable photo sensing performance and reliability.

Figure 3-8 is the multiple cycle photo response of Gr/GO/Si photodetector, which shows stability and repeatability of the device. When inserted with a GO interlayer, the graphene-silicon Schottky photodiode could still respond quickly to the incident optical signal, while the rise time and fall time are about 1 ms.

The Band diagrams of Gr/Si and Gr/GO/Si Schottky junction are shown in Figure 3-9. In ideal Gr/Si Schottky junction, when graphene and silicon contact each other, the electrons in silicon flow into graphene due to the difference of their work functions, making the Fermi energy levels equal again and leaving a depletion region in silicon. On the silicon side of the Schottky junction, the band bends upward and form a built-in electric field. However, in the actual Gr/Si Schottky junction, there is usually a high surface density of states at the interface, which leads to Fermi level pinning effect and increases the carrier recombination

rates at the interface. By inserting GO film as an interlayer, the reverse current of Schottky junction can be effectively suppressed.

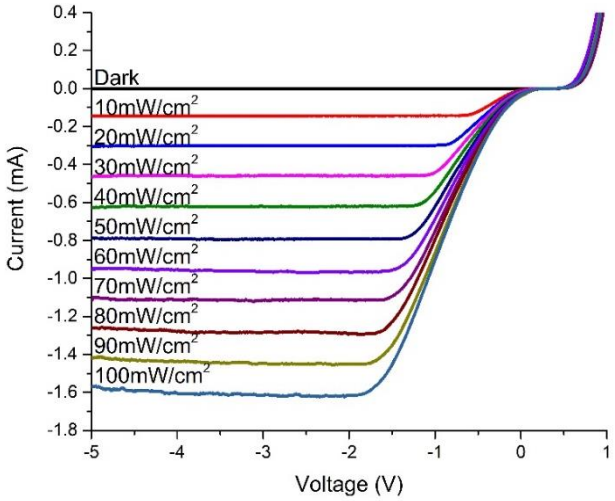

Figure 3-7 The I-V curves of Gr/GO/Si photodetector with varying light power intensity

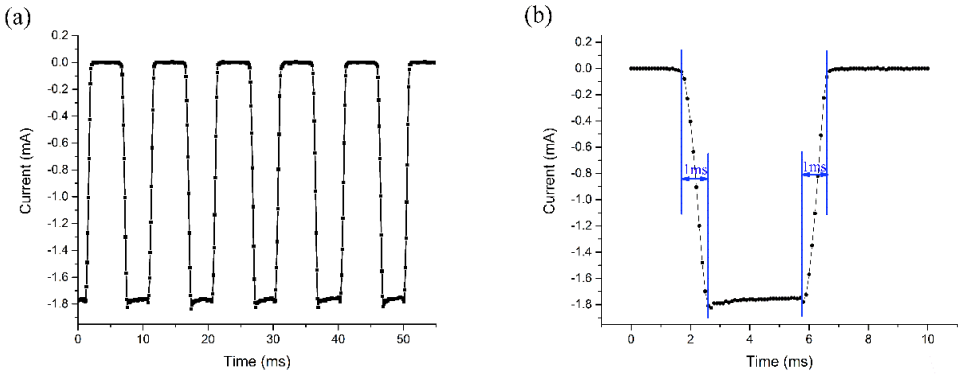

Figure 3-8 The photoreponse of Gr/GO/Si Schottky photodetector. (a) Photoresponse to periodic light signal. (b) Rise time and fall time.

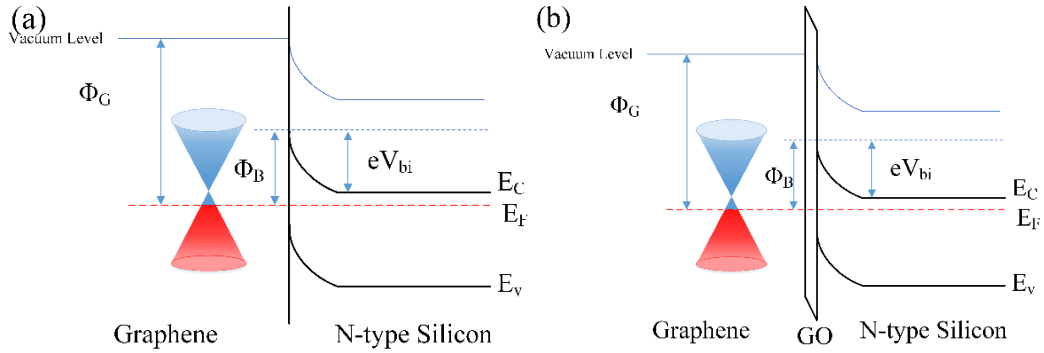

Figure 3-9 Band diagrams of Gr/Si and Gr/GO/Si Schottky junction.

The suppression of reverse current of Schottky junction by graphene oxide interlayer is the main reason for the decrease of dark current of Gr/GO/Si photodetector. Based on the thermal emission theory [154], a correction factor

should be introduced into the equation (2-9) for the reverse saturation current of Gr/Si Schottky junction with an interface layer,

$$I_0 = AA^*T^2e^{-\sqrt{\chi}\delta}e^{-\frac{\Phi_B}{kT}} \quad (3\text{-}1)$$

where χ is mean barrier height presented by the interface film, and δ is the oxide thickness of interlayer. The modified equation clearly shows the inhibition effect of GO interface layer on reverse saturation current of Schottky junction. For the prepared Gr/Si and Gr/GO/Si photodetectors, the reverse current of the Schottky junction is the main component of the dark current when they work under reverse bias. Therefore, the dark current of the photodetector can be effectively suppressed after inserting the GO interface layer, which is 26 times lower than before.

Figure 3-10 shows the ln(I)-V curve of the Gr/Si photodetector under dark condition. The slope and intercept of its fitting are 18.35 and -22.51, respectively. Based on equation (2-12), the ideal factor η, reverse saturation current I_0 and Schottky barrier height Φ_B of the Gr/GO/Si photodetector are calculated to be 2.10, 1.68×10^{-10} A and 0.91 eV respectively. The increase of Schottky barrier height and the decrease of reverse saturation current show the improvement of the interface layer structure on the Schottky photodetector.

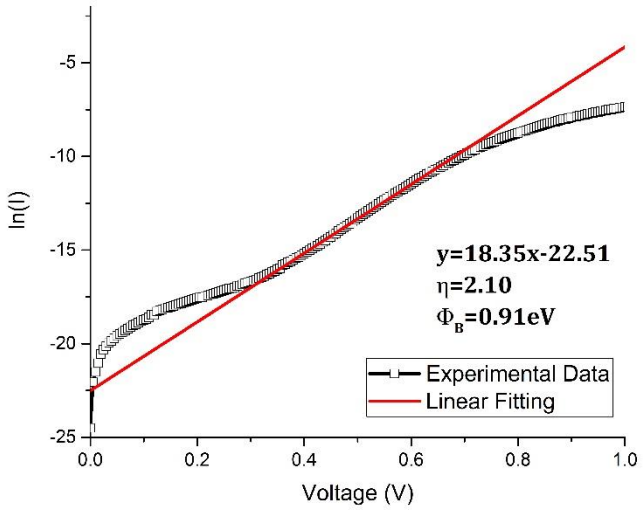

Figure 3-10 The semilogarithmic I-V curves of Gr/GO/Si Schottky photodetector

The key characteristic parameters of Schottky junction can be extracted from the I-V response curve of Gr/GO/Si Schottky photodetector in dark condition based on Cheung's function. As shown in Figure 3-11 (a), we calculated and plotted the dV/dlnI - I curve, as well as its linear fitting. The slope and intercept of the fitting line are 319 and 0.05679, respectively. Based on equation (2-14), the ideal factor η and series resistance R_s of Gr/GO/Si Schottky junction are 2.19 and 319 Ω, respectively. Figure 3-11 (b) shows the H(I) - I curve of Gr/GO/Si Schottky junction, the slope and intercept of its linear fitting are 268 and 2.0759 respectively. Based on equation (2-15) and the value of ideal factor η just

calculated by equation (2-14), the barrier height Φ_B and series resistance R_s of Gr/GO/Si Schottky junction are 0.94 eV and 268 Ω, respectively. The series resistance values of Gr/GO/Si Schottky junction calculated by the two equations are about 300 Ω, which is similar with that of Gr/Si Schottky junction. It can be seen that the introduction of GO interface layer has no obvious effect on the series resistance of Gr/Si Schottky photodetector.

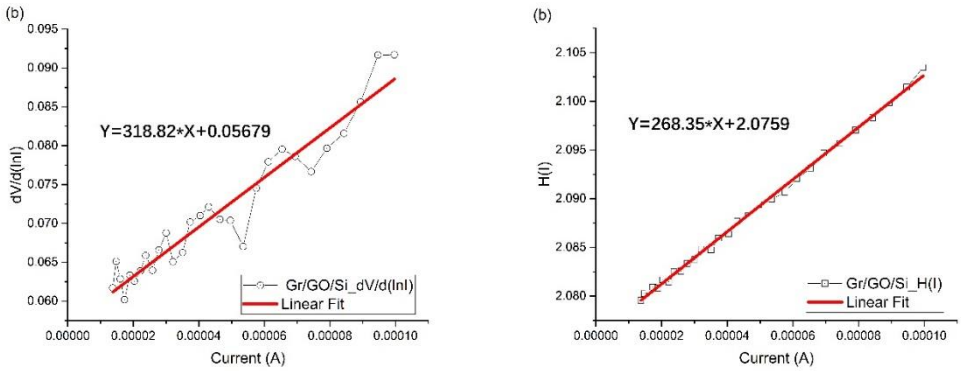

Figure 3-11 The dV/dlnI - I and H(I) - I curves of Gr/GO/Si Schottky photodetector

The barrier height of Gr/GO/Si Schottky junction can also be extracted based on Norde's function. The F(V)-V curve of Gr/GO/Si Schottky junction is shown in Figure 3-12. When the bias voltage is 0.13 V, the minimum value of function F(V) is 0.8373. Thus, the barrier height Φ_B of Gr/Si Schottky junction can be calculated as 0.86 eV.

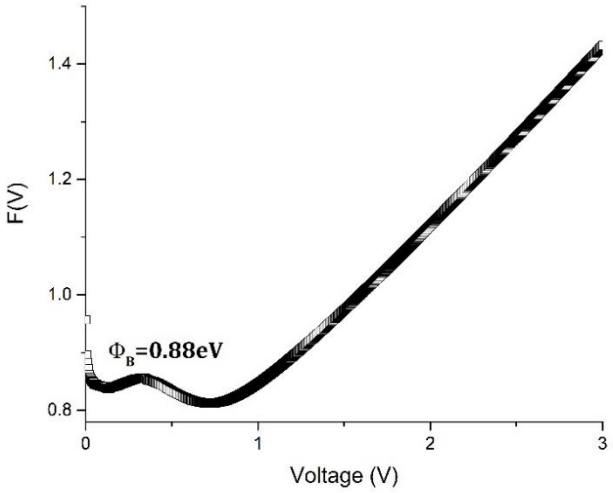

Figure 3-12 The F(V) - V curve of Gr/GO/Si Schottky photodetector

The characteristic parameters of Gr/Si and Gr/GO/Si Schottky junctions are shown in Table 3-2. The values of characteristic parameters of Schottky junctions based on thermal emission theory, Cheung's function and Norde's function are slightly different, because they are extracted from different regions of I-V characteristic curve of Schottky junctions. However, they show the same trend, that is, the ideal factor value of Gr/Si photodetector decreases after inserting the

GO interlayer, and the Schottky barrier height increases significantly, which improves the overall performance of the Schottky photodetector. The inherent mechanism is complex, but the bending of the silicon band and the decrease of the defect density at the Gr/Si interface caused by the GO interface layer play a important role.

Table 3-2 The performance parameters of Gr/Si and Gr/GO/Si Schottky photodetector

Parameters	Gr/Si	Gr/GO/Si
Based on thermal emission theory		
Ideality factor, η	2.29	2.10
Saturation current, I_0	4.93×10^{-10} A	1.68×10^{-10} A
Schottky barrier height, Φ_B	0.88 eV	0.91 eV
Based on Cheung's function(dV/dlnI - I)		
Ideality factor, η	2.26	2.19
Series resistance, R_s	285 Ω	319 Ω
Based on Cheung's function (H(I) - I)		
Schottky barrier height, Φ_B	0.91 eV	0.94 eV
Series resistance, R_s	294 Ω	268 Ω
Based on Norde's function		
Schottky barrier height, Φ_B	0.86 eV	0.88 eV

When a shunt resistance R_{sh} is included, the equation (2-9) can be further modified as,

$$I = \frac{R_{sh}}{R_s+R_{sh}}\left[I_0\left(e^{\frac{q(V-R_sI)}{\eta kT}}-1\right)-\frac{V}{R_{sh}}\right] \quad (3\text{-}2)$$

With the calculated series resistance and ideality factor, the shunt resistance R_{sh} is calculated as 6.5 GΩ and 26.2 GΩ for Gr/Si and Gr/GO/Si Schottky junction, respectively. Overall, the GO interface layer can suppress the dark current of the graphene photodetector by blocking the reverse current, increasing the Schottky barrier height and increasing the shunt resistance. Based on the thermal emission theory, Cheung's function and Norde's function, the analysis of I-V characteristics reveals the influence of GO interface layer on the Gr/Si Schottky photodetector. After inserting GO layer, the series resistance was maintained, the ideality factor showed slight increase, meanwhile significant increase could be observed on Schottky barrier height and shunt resistance, which led to the suppression of revise saturation current, thus the enhanced graphene based photodiode with low dark current was realized.

As shown in Figure 3-6, the graphene-silicon photodiode with GO interlayer shows not only the suppression of dark current, but also the increase of photocurrent by 2.73 times. The exact reason for this photocurrent enhancement is not clear, but we believe it is a result of various factors.

According to the equation (2-3), the built-in potential V_{bi} of Schottky junction is directly related to the Schottky barrier height Φ_B. The Schottky barrier heights

of Gr/GO/Si Schottky junction calculated by three different methods are significantly higher than those of Gr/Si. As the doping concentration of n-type silicon substrate is same for Gr/Si and Gr/GO/Si Schottky junction, the built-in potential of Schottky junction increases with the insertion of GO interlayer. The separation of photogenerated carriers in Schottky junction photodetectors depends heavily on the built-in potential. The increase of built-in potential can not only promote the photogenerated holes to move to graphene, but also reduce the recombination of photogenerated carriers, thus improving the photocurrent of the photodetectors.

Moreover, the inserted GO layer was helpful to absorb the incident light, both the GO itself and the surface where GO contacted with graphene and silicon had the ability to collect light energy [155,156]. The transparency of GO films was relevant to the π-electron system in GO. As GO contains various functional groups, there was a distinct transmittance difference between GO and graphene[155].Actually, graphene oxide is also one kind of photosensitive material, there are many reports on photodetectors based on graphene oxide and reduced graphene oxide[88, 157-160]. Those photogenerated electron-hole pairs in graphene oxide can also be separated by built-in or external electric field and generate extra photocurrent. As a result, more light energy could be collected and could be used to excite electron-hole pairs, so the device showed enhanced photoresponse.

Passivation effect of the GO layer on the Si surface also contributed to the improvement of the photodetector. As the electronic states caused by interfacial defects act as the recombination centers for minority carriers, the Gr/Si interface played a very important role in the performance of the photodetector. The GO interfacial layer could effectively suppress the interface recombination of graphene/Si photodetector and enhance its photo response[132, 161]. Yang et al. revealed that the GO layer could effectively passivate the Si surface and increase the effective carrier lifetime from 12 μs to 33 μs[132]. The reduction of Si surface recombination for minority carriers was definitely beneficial for the improvement of graphene photodetector performance.

Overall, the inserted GO interlayer in Gr/Si Schottky photodetector decreases the dark current by blocking the reverse current, increasing the Schottky barrier height and increasing the shunt resistance. Meanwhile, the GO interlayer increases the photocurrent due to the improved built-in potential, the extra light absorption and the passivated interface. The experimental results in this chapter demonstrate the enhancement effect of GO interface layer on Gr/Si Schottky photodetector, and the improved method can also be applied to other types of Schottky photodetectors in theory. According to the equation (1-13) and (1-14), the specific detectivity and NEP of the Gr/GO/Si photodetector were calculated as 1.88×10^{12} Jones and 0.09 $pW/Hz^{1/2}$, respectively. The comparison with previous published work is shown in Table 3-3, indicating the good performance of the Gr/GO/Si photodetector, especially the higher ON/OFF ratio that benefits from the enhanced photocurrent and suppressed dark current.

Table 3-3 Comparison of the performances of the graphene based photodetectors

Structure	λ (nm)	R (A/W)	D* (Jones)	NEP ($pW/Hz^{1/2}$)	I_d (nA)	$R_{on/off}$	Ref
Gr/GO/Si	633	0.65	1.88×10^{12}	0.09	9.472	2.73×10^{5}	This work
Gr/Si	890	0.73	4.2×10^{12}	0.075	9.3	10^{4}	[125]
Gr/Si	730	0.435	2.1×10^{8}	33	—	10^{4}	[87]
MoO3-Gr/Si	750	0.4	5.4×10^{12}	—	—	—	[162]
P3HT–Gr/Si	540	0.78	2.6×10^{10}	0.14	40	—	[134]
Gr/GO/Si	visible	0.266	—	—	—	—	[132]

3.4 Summary

In this chapter, graphene/silicon Schottky photodetector enhanced by graphene oxide inlayer was fabricated. The current-voltage characteristics showed that the dark current of Gr/GO/Si Schottky junction photodetector was 26 times lower than that of Gr/Si photodetector, and the photocurrent was 2.73 times higher than that of Gr/Si photodetector. The responsivity of the photodetector to 633 nm incident light reached 0.65 A/W under 2 V reverse bias voltage. The current-voltage curves showed that the photocurrent was proportional to the incident light power, and the photocurrent remained stable while the bias voltage increased. The response speed of graphene-silicon photodiode was well preserved after inserting GO interlayer, where the response time and recovery time were ~1ms.

Based on the thermal emission theory, Cheung's function and Norde's function, the analysis of I-V characteristics reveals the influence of GO interface layer on the Gr/Si Schottky photodetector. The GO interface layer can suppress the dark current of the graphene photodetector by blocking the reverse current, increasing the Schottky barrier height and increasing the shunt resistance. Meanwhile, due to the improved built-in potential, the extra light absorption and the passivated interface, the photocurrent of the detector increases significantly after inserting GO interlayer. Benefiting from the suppression of dark current and the improvement of photocurrent, the on/off ratio of the photodetector reaches 2.73×10^{5}, the specific detectvity and the equivalent noise power are 1.88×10^{12} Jones and 0.09 $pW/Hz^{1/2}$, respectively. This work exhibited the double effects of GO interlayer: the suppression of dark current and the improvement of photocurrent. It also showed the potential prospect of graphene oxide on photosensitive devices.

Chapter 4

Graphene/silicon Schottky photodetector enhanced by gold nanoparticles

4.1 Introduction

As a typical two dimensional carbon material, graphene has ultrafast carrier mobility, zero band gap structure and broadband light absorption. Graphene can be applied to photodetectors to achieve ultrafast and wide spectrum detection. However, the low light absorption of graphene is one of the main reasons that hinder the efficiency improvement of graphene photodetector. The absorbance of single-layer graphene to incident light is only 2.3%. Enhancing the interaction between graphene and incident light is the key to realize high efficiency graphene photodetector.

Surface plasmon polarizations (SPP) are electromagnetic excitations formed by the interaction of electrons and photons on the metal surface, free electrons are driven by the alternating electric field to collectively oscillate at a resonant frequency. With the help of the surface plasmon nano-structure, the light energy can be collected in a spatial region beyond the diffraction limit and form a confined near-field optical field. By coupling sub-wavelength metal nanostructures to graphene photodetector, the enhanced optical field will directly improve the responsivity of the photodetector. Meanwhile, wavelength selective response can be realized by changing the configuration of nanostructures.

In this chapter, gold nanoparticles (AuNPs) were fabricated on Gr/Si Schottky photodetectors by two different methods, gold film annealing and electron beam lithography. The photoelectric and electrical properties of AuNPs enhanced photodetectors were tested, and the effects of AuNPs on the responsivity and spectral response of the photodetectors were analyzed. The finite-difference time-domain (FDTD) method was utilized to simulate and analyze the near-field light

field enhancement effect of gold nanoparticles, and the simulation results were compared with the experimental spectral response of the AuNPs enhanced photodetector. Based on the thermal emission theory, Cheung's function and Norde's function, the key characteristic parameters of the AuNPs/Gr/Si Schottky junction are extracted from the current-voltage characteristic curve, and the mechanism of Au nanoparticles to improve the performance of the photodetector was discussed.

4.2 Gold nanoparticles enhanced graphene photodetectors by thin film annealing

Annealing is a common material treatment process, which is to heat the material to a predetermined temperature, hold for a certain time, and then cool to room temperature. Annealing is low cost and easy to operate, which can improve ductility, reduce brittleness, relieve internal stresses, refine grain size and eliminate structural defects. It is widely used in the treatment of various metal and non-metal materials. In the past decade, with the deepening of the research on the local surface plasmon enhancement of the light field by sub-wavelength nanostructures, annealing technology has been used to fabricate metal nanoparticles, which are formed by melting, spheroidizing and re-solidifying the metal film with nanometer thickness at high temperature. At present, the commonly used metal film deposition methods include magnetron sputtering, electron beam evaporation, etc. The metal film obtained by magnetron sputtering has higher internal stress and less adhesion to the substrate, which is easier to crack and form metal nanoparticles under the same annealing conditions. Therefore, in this chapter, the gold film deposited by magnetron sputtering is annealed to obtain gold nanoparticles, which can be used to enhance performance of graphene/silicon Schottky photodetector.

4.2.1 Preparation of gold nanoparticles by thin film annealing

Under the condition of high temperature annealing, the gold film with nanometer thickness stays in an unstable state, which will crack and agglomerate under the action of surface tension. Based on this method, the nanoscale gold particles can be obtained on the surface of the substrate. The size and density of gold nanoparticles can be tuned by changing the annealing temperature and time. In this chapter, the gold nanofilms deposited by magnetron sputtering were annealed with different time, and the morphology of gold nanoparticles was characterized. The detailed process is as follows:

1) The silicon substrate was cleaned by ultrasonic treatment sequentially in isopropanol, acetone and deionized water for 15 minutes for each, and then dried by nitrogen.

2) Gold films with thickness of 5 nm and 10 nm were deposited on the substrate by magnetron sputtering system. Due to the small thickness, the metal layer did not form a continuous film.

3) The sample was placed in a vacuum tube furnace. After vacuumizing the furnace, high-purity argon was introduced until the furnace pressure reached atmospheric pressure, and then vacuumized again. Repeat this for three times to ensure that the air in the furnace has been exhausted. Finally, high-purity argon was introduced as protective gas, and the gas pressure in the chamber was slightly higher than the atmospheric pressure.

4) The samples were heated to 400 ℃ for 15 minutes and 30 minutes respectively, and then cooled to room temperature. After heat treatment, the metal layers on the substrate will agglomerate to form uniformly distributed semi ellipsoidal nanoparticles.

The morphology of gold nanoparticles was characterized by scanning electron microscopy. As shown in Figure 4-1, when the deposition thickness is 5 nm, the gold film is not completely formed, and there are many gaps on the surface; intermittent connected island structure can be formed after annealing at 400 ℃ for 15 minutes, which is evenly distributed on the surface of the sample; when the annealing time is increased to 30 minutes, the agglomeration of the gold film is more sufficient, and disordered gold nanoparticle arrays are formed on the surface of the sample. For the gold film with a thickness of 10 nm, the gap on the surface of the film has been filled, and the film has relatively good continuity. However, due to the high thickness of the film, independent gold nanoparticles are formed after annealing. They adhere to each other and take on banded distribution on the surface of the sample. With the increase of annealing time from 15 minutes to 30 minutes, the width of the formed nanoribbons also increases significantly, and the adhesion between them is more obvious.

It can be seen from the SEM images that the deposition thickness and annealing time of the gold film have a significant effect on the surface morphology of the agglomerated gold film. The 5 nm thick gold film annealed for 30 minutes can form well distributed, independent and non-adhesive gold nanoparticles. When the incident light irradiates the gold particles whose size is not larger than the wavelength of light, there will be local near-field enhancement around the gold nanoparticles due to the local surface plasmon resonance. Considering that the direct measurement of the near-field optical field is not easy to realize experimentally, the enhancement effect of the local optical field is verified by the enhancement of the Raman signal of graphene oxide by gold nanoparticles.

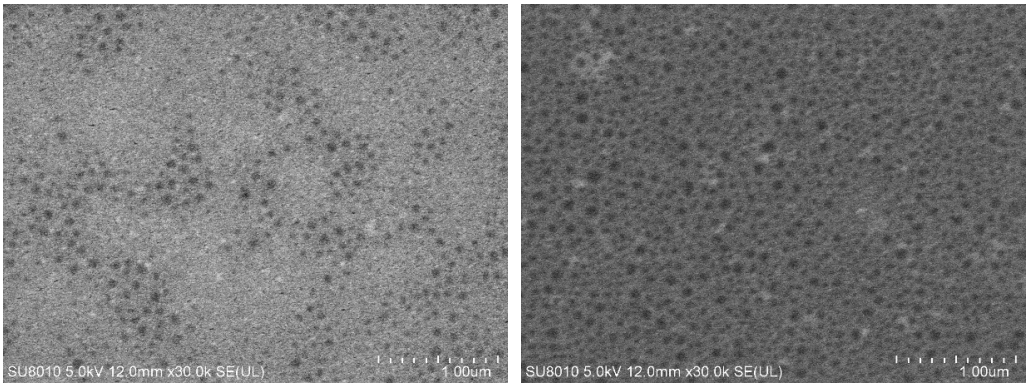

(a) 5 nm film without annealing. (b) 10 nm film without annealing.

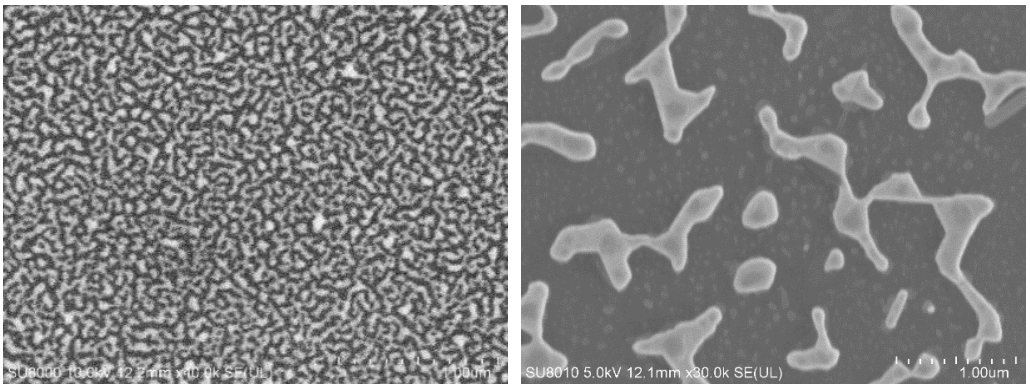

(c) 5 nm film with 15 min annealing. (d) 10 nm film with 15 min annealing.

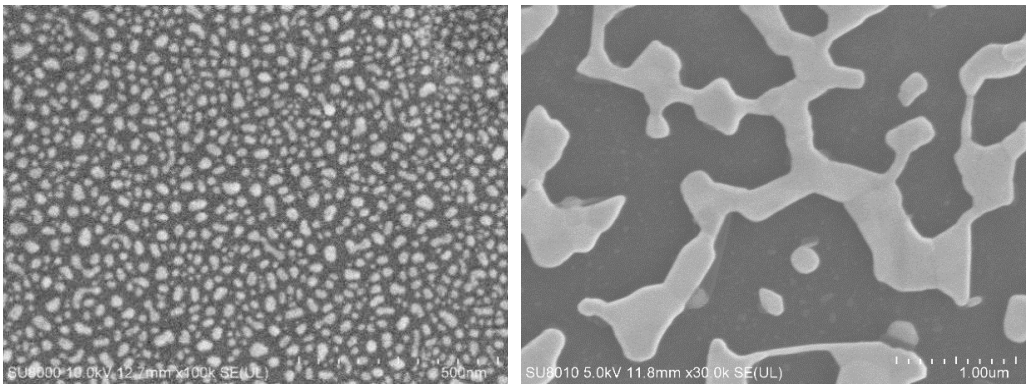

(e) 5 nm film with 30 min annealing. (f) 10 nm film with 30 min annealing.

Figure 4-1 The gold nanoparticles fabricated by thin film annealing.

Gold films with thickness of 5 nm and 10 nm were deposited on graphene oxide films and annealed at 400 ℃ for 30 minutes. As shown in Figure 4-2, the Raman spectrum of GO covered with the gold film is obviously weakened, the reason is the shielding effect of the gold film, which reduces the excitation light incident on the GO film. After annealing at 400 ℃ for 30 minutes, the Raman signal intensity of GO sample with 5 nm gold film is higher than that of pure GO sample, which indicates that gold nanoparticles enhance the light field intensity in the region where GO is located; while for gold films with 10 nm gold film, the results show that the Raman signal intensity of the annealed sample is stronger than before annealing, but it is still weaker than that of the GO sample annealed without gold particles. This is because the shielding effect of the gold nanoribbons is stronger than the enhancement of the local surface plasmon resonance. Therefore, gold nanoparticles formed by annealing 5 nm thick gold film for 30 minutes are selected to enhance the photoelectric response of graphene/silicon photodetector.

In order to obtain the three-dimensional morphology of gold nanoparticles, the gold films before and after annealing were measured by atomic force microscope. Figure 4-3 and Figure 4-4 show the AFM images of 5 nm thick gold film before and after annealing for 30 minutes at 400 ℃. From the results we can see that the surface of the gold film before annealing is smooth and fluctuates in the range of ~1 nm; after annealing, the gold thin film agglomerates and forms

semi ellipsoidal gold nanoparticles with the diameter of 40 nm ~ 60 nm and the height of 3 nm ~ 6 nm.

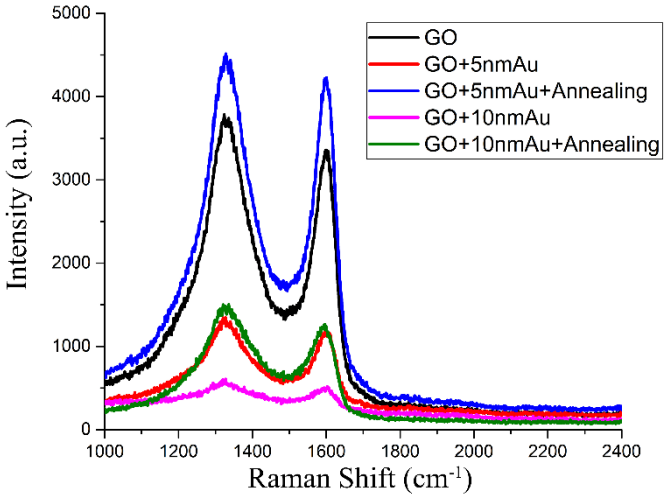

Figure 4-2 Raman spectrums of GO covered with the gold film and nanoparticles

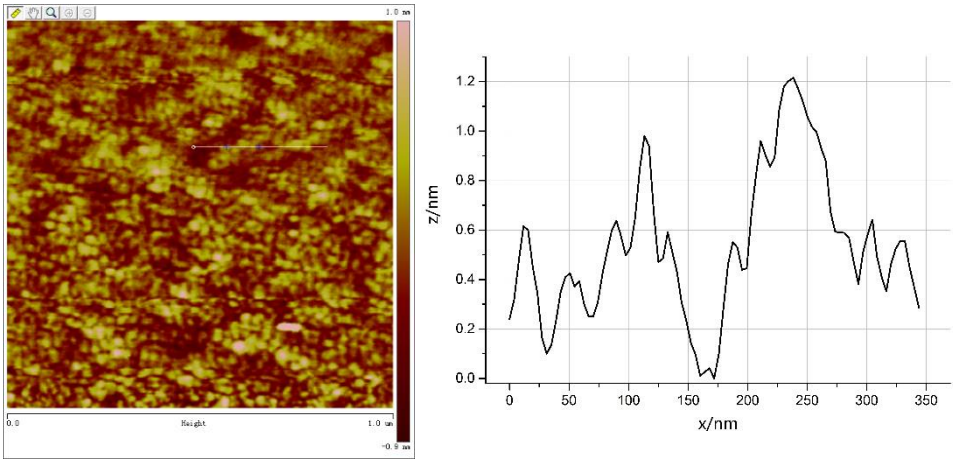

Figure 4-3 AFM image of 5 nm gold film before annealing

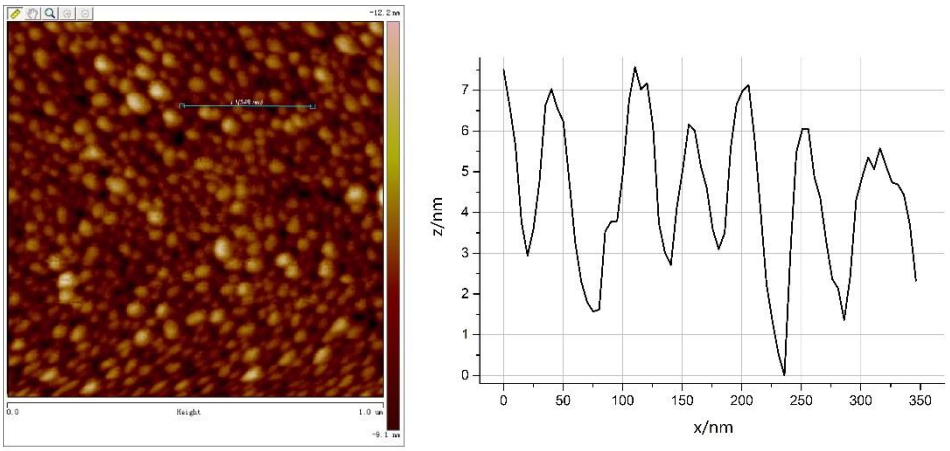

Figure 4-4 AFM image of 5 nm gold film after annealing

The three-dimensional morphology of gold nanoparticles is shown in Figure 4-5. In order to analyze the light field enhancement effect, a three-dimensional

model of gold nanoparticles is established based on the measurement result of atomic force microscope. The substrate material is silicon, and the light field distribution is simulated by using the finite-difference time-domain method.

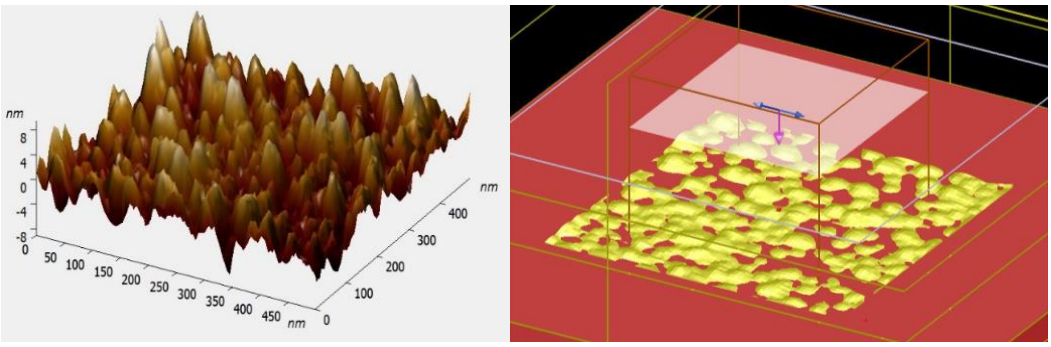

Figure 4-5 The 3D morphology of gold nanoparticles. (a) The 3D morphology measured by AFM. (b) The 3D model in FDTD simulation.

We take the average value of the light field intensity of each XY plane with different heights, and draw the distribution diagram of the light field intensity near the gold nanoparticles with height and incident light wavelength, as shown in Figure 4-6. The area with $z < 0$ is silicon, the gold nanoparticles are distributed on the silicon surface, and the rest is air medium. We calculate and plot the curve of the average light field intensity with the incident wavelength, as shown in Figure 4-7. At the interface of gold nanoparticles and silicon ($z = 0$), when the incident light wavelength is 500 nm ~ 600 nm, the light field intensity is significantly enhanced. At the peak position of 570 nm, it is ~2.5 times higher than that without gold nanoparticles. However, with the decrease of height, the peak wavelength shows obvious blue shift, and the resonance peak wavelength is about 500 nm at $z = -50$ nm.

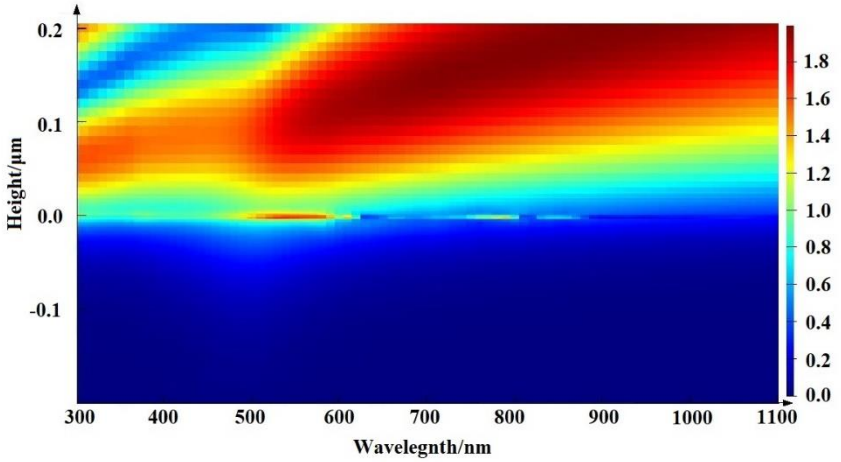

Figure 4-6 The light field intensity near the gold nanoparticles versus height and incident light wavelength

From the transmission spectrum in Figure 4-8, we can observe the obvious anomalous transmission. The abnormal transmission peak is at 533 nm, and the transmittance is 83%. The abnormal transmission phenomenon is due to the surface plasmon resonance excited by gold nanoparticles, and the wavelength of

the abnormal transmission peak is same as that of the surface plasmon resonance peak.

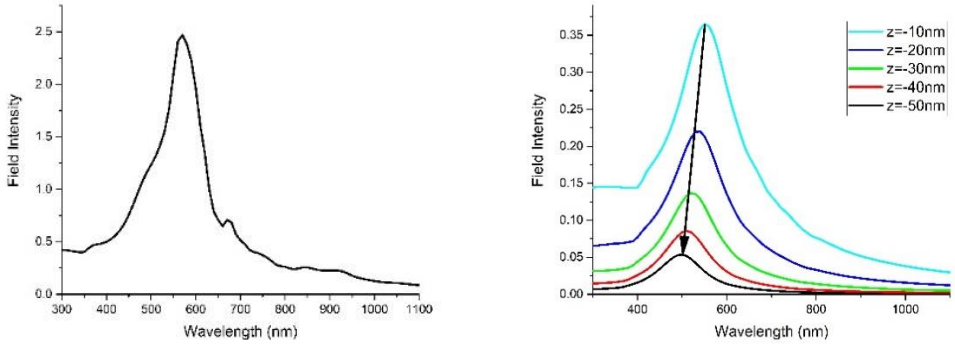

Figure 4-7 The average light field intensity as a function of wavelength. (a) At the interface. (b) At various depths.

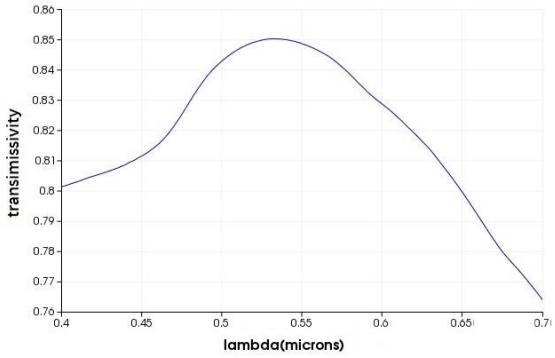

Figure 4-8 The transmissivity as a function of wavelength.

4.2.2 Fabrication and characterization of gold nanoparticles enhanced photodetectors

Firstly, the graphene/silicon Schottky photodetector was fabricated with the same process of the foregoing chapters. The active area of the photodetector was 1.6 × 1.6 mm square window. Then a 5 nm thick gold film was deposited on the surface of the Gr/Si Schottky junction and annealed at 400 ℃ for 30 minutes to form the gold nanoparticles, which was used to enhance the performance of the photodetector.

The photoelectric response of the photodetector were tested by the semiconductor device analyzer (keysight B1500A). The sample and the analyzer were connected by a probe station, and a 633 nm semiconductor laser was used as the incident light source. Figure 4-9 shows the current-voltage response curves of AuNPs/Gr/Si Schottky photodetectors in the dark and light conditions at room temperature, where the incident light power density is 160 mW/cm^2. The short circuit current is 29.8 μA and the open circuit voltage is 0.29 V. Under the reverse bias voltage of 2 V, the dark current is 42.8 nA and the photocurrent is 1.146 mA. According to the equation (1-3) and (1-15), the current responsivity and on/off ratio are calculated as 0.28 A/W and 1.8×10^4 respectively. As shown in table 4-1,

the AuNPs/Gr/Si photodetector has obvious enhancement compared with that without gold nanoparticles.

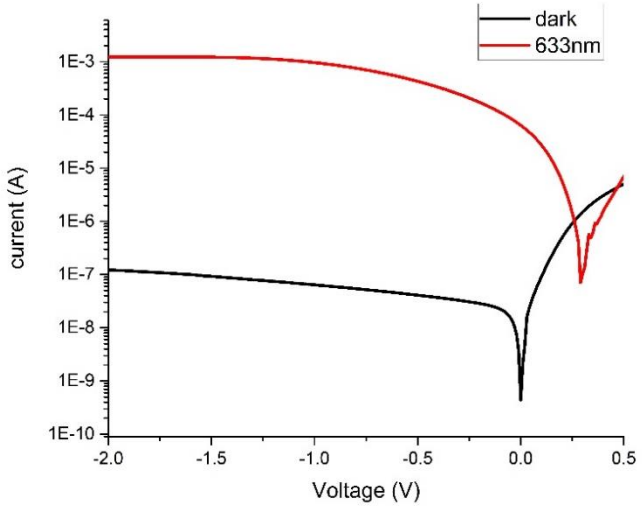

Figure 4-9 The I-V curves of thin film annealing AuNPs/Gr/Si Schottky photodetector at room temperature under dark and illumination

Table 4-1 The performance paramters of Gr/Si and AuNPs/Gr/Si Schottky photodetector

Structure	V_{oc} (V)	I_{sc} (μA)	I_d (nA)	I_{ph} (mA)	R (A/W)	$r_{on/off}$
Gr/Au	0.25	20.7	256	0.941	0.23	3.7×10^3
AuNPs/Gr/Si	0.29	29.8	42.8	1.146	0.28	2.9×10^4

The photoelectric response characteristics of the photodetector under different incident light power intensity are shown in Figure 4-10. For the periodic incident light signals with different power, the photodetector has stable response current. With the increase of the incident light power intensity, the photocurrent of the detector increases linearly in a wide dynamic range.

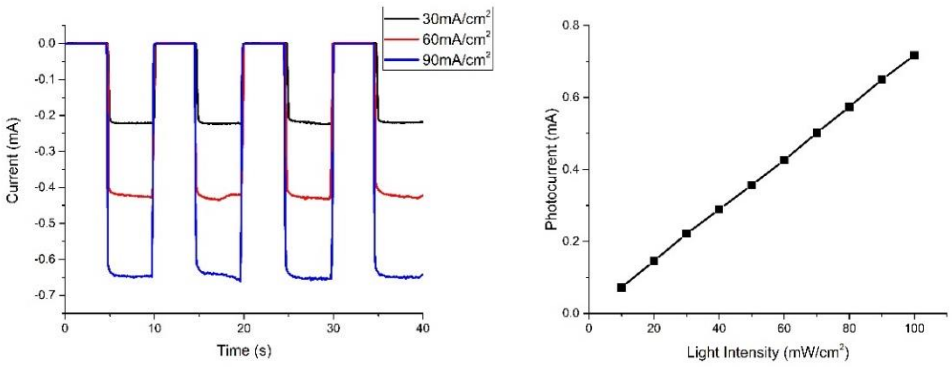

Figure 4-10 The photoreponse of AuNPs/Gr/Si Schottky photodetector. (a) Photoresponse under periodic light signal. (b) Photocurrent as a function of incident light power intensity

The spectral response of the thin film annealed gold nanoparticles enhanced Gr/Si photodetector is shown in Figure 4-11. It can be seen that the photocurrent

response of AuNPs/Gr/Si photodetector is higher than that of Gr/Si detector in the visible light band of 400 nm-780 nm. When the incident light wavelength is 500 nm, the gold nanoparticles have the maximum gain for the photodetector, and the current responsivity increases from 0.15 A/W to 0.22 A/W, which increases by 48%. When the incident light wavelength is 610 nm, the Au nanoparticles enhanced Gr/Si photodetector has the maximum current responsivity of 0.24 A/W. Since the incident light is mainly absorbed by silicon in the Gr/Si photodetector, considering that the wavelength of the light field enhancement peak of gold nanoparticles is continuously blue shifted with the increase of depth, the position of the surface plasmon resonance peak in silicon is 500 nm ~ 570 nm. The enhancement of Au nanoparticles on the photodetector measured in the experiment is in good agreement with the light field intensity and transmission spectrum in the simulation result. Meanwhile, it can be seen from the spectral response of the photodetector that the responsivity of AuNPs/Gr/Si decreases to a certain extent in the ultraviolet band with wavelength less than 400 nm and the infrared band with wavelength greater than 800 nm. The reason is that the shielding effect of nanoparticles is greater than the enhancement effect of near-field light field in the band far from the resonance peak. Due to the enhancement and attenuation effect of gold nanoparticles on different wavelengths, the current responsivity of AuNPs/Gr/Si photodetector is basically unchanged in a wide spectral range of 500 nm ~ 900 nm, ranging from 0.22 A/W~0.24 A/W.

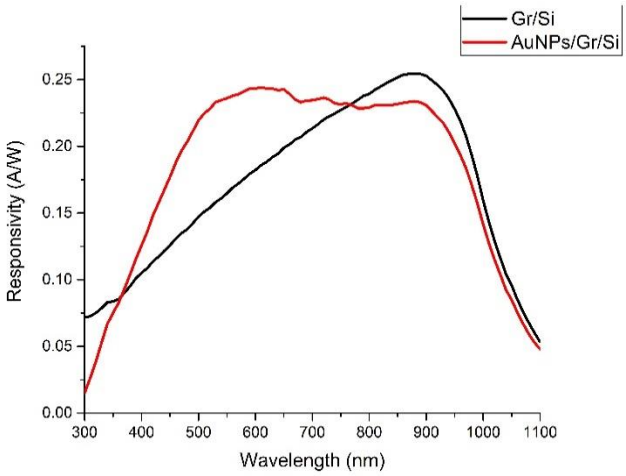

Figure 4-11 The spectral response of AuNPs/Gr/Si Schottky photodetector

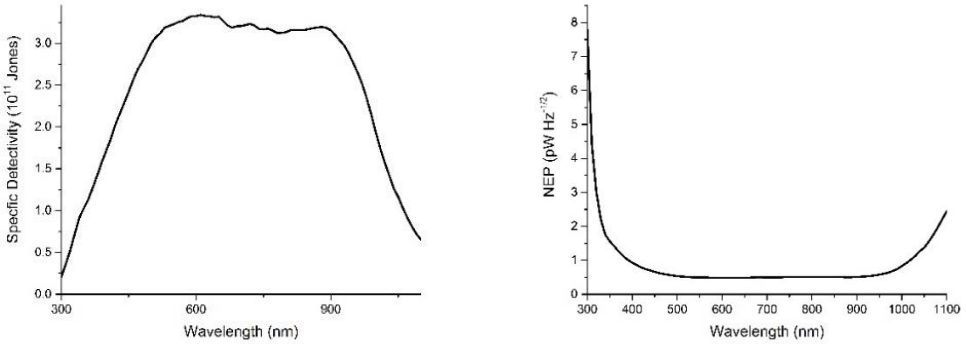

Figure 4-12 The specific detectivity and noise equivalent power of AuNPs/Gr/Si Schottky photodetector. (a) specific detectivity. (b) noise equivalent power.

The specific detectivity and noise equivalent power of AuNPs/Gr/Si photodetector can be calculated by equation (1-13) and (1-14). The noise equivalent power is the minimum incident light power required for an output signal-to-noise ratio of 1, which reflects the detection limit of the photodetector for weak signal, while the specific detectivity reflects the ability of the photodetector to produce an observable output signal under the influence of noise. As shown in Figure 4-12, when the incident light wavelength is 610 nm, the specific detectivity of AuNPs/Gr/Si photodetector reaches the maximum value of 3.34×10^{11} Jones, and the noise equivalent power of the photodetector reaches the minimum value of 0.48 pW Hz $^{-1/2}$.

The semi log current-voltage curve of AuNPs/Gr/Si photodetector under dark condition is shown in Figure 4-13, as well as its linear fitting. The slope and intercept of the fitting line are 7.09 and -18.87 respectively. Based on thermal emission theory and equation (2-12), the ideal factor η, reverse saturation current I_0 and Schottky barrier height Φ_B of AuNPs/Gr/Si photodetector can be calculated to be 5.45 and 6.36 $\times10^{-9}$ A and 0.81 eV respectively.

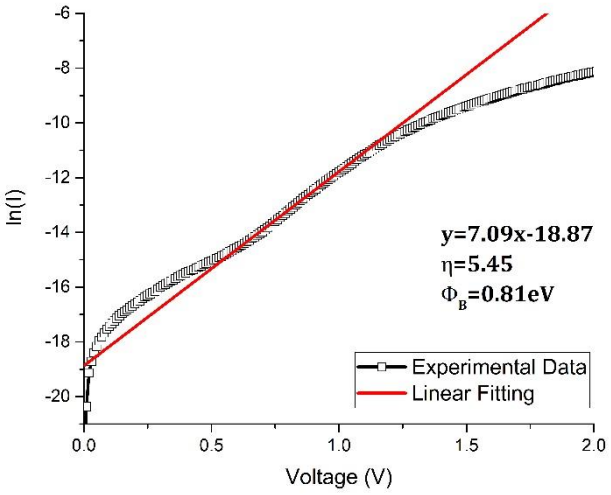

Figure 4-13 The semilogarithmic I-V curves of AuNPs/Gr/Si Schottky photodetector

Based on Cheung's function, the characteristic parameters of AuNPs/Gr/Si Schottky junction can be extracted from the linear fitting of the dV/dlnI - I and H(I) - I curves. As shown in Figure 4-14 (a), the slope and intercept of dV/dlnI - I fitting line are 1775 and 0.1486 respectively, so the ideality factor η and series resistance R_s of AuNPs/Gr/Si Schottky junction are 5.74 and 1775 Ω respectively. The slope and intercept of H(I) - I fitting line in Figure 4-14 (b) are 568 and 5.3517 respectively, so the barrier height Φ_B and series resistance R_s are 0.93 eV and 568 Ω respectively.

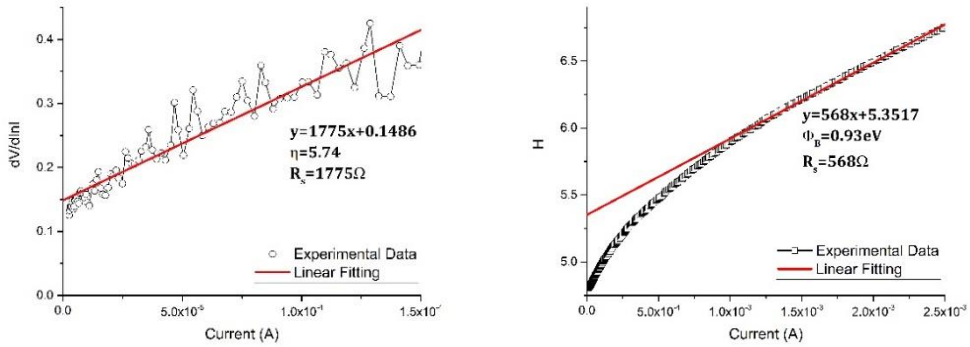

Figure 4-14 The dV/dlnI - I and H(I) - I curves of AuNPs/Gr/Si Schottky photodetector

Likewise, the Schottky barrier height Φ_B can also be calculated by Norde's function. According to equation (2-17), the F(V)-V curve of Schottky junction was calculated and plotted. As shown in Figure 4-15, when the bias voltage is 0.1V, F(V) reaches the minimum value of 0.8202. According to equation (2-18), the barrier height Φ_B of AuNPs/Gr/Si Schottky junction is 0.89 eV.

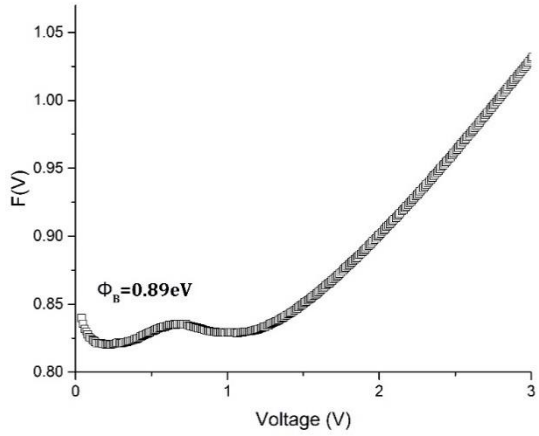

Figure 4-15 The F(V) - V curve of AuNPs/Gr/Si Schottky photodetector

The characteristic parameters of Gr/Si and AuNPs/Gr/Si Schottky junctions are shown in Table 4-2. The Schottky barrier height Φ_B of AuNPs/Gr/Si calculated by thermal emission theory is lower than that calculated by Cheung's function and Norde's function, because the influence of series resistance on current is ignored in the equation (2-12) of thermal emission theory. For AuNPs/Gr/Si Schottky junction, the annealing process to form gold nanoparticles leads to the degradation of graphene and the increase of series resistance, resulting in a large error in the value of Schottky barrier height Φ_B calculated by thermal emission theory equation. The Schottky barrier height of AuNPs/Gr/Si calculated by Cheung's function and Norde's function is higher than that of Gr/Si Schottky junction, because the work function of gold (5.3 eV) is larger than that of graphene (~ 4.6 eV). When the two materials contact to each other, electrons in graphene flows to gold particles, resulting in p-type doping of graphene. According to the equation (2-2), the height of Schottky barrier is determined by

the Fermi energy level of graphene and the electron affinity energy of silicon. Therefore, the Schottky barrier height Φ_B of the Schottky junction increases after the modification of gold nanoparticles.

It can also be seen from Table 4-2 that the ideal factor of AuNPs/Gr/Si Schottky junction increases greatly, that means the interface quality is greatly affected by metal deposition and thin film annealing. The series resistance of AuNPs/Gr/Si Schottky junction also increases a lot compared with that of Gr/Si Schottky junction, which might be the reason that the photocurrent improvement of the photodetector is lower than the improvement of light field intensity. In the wavelength range far away from the surface plasmon resonance peak, the photoelectric response of the photodetector is even weaker than that without gold nanoparticles.

Table 4-2 The performance parameters of Gr/Si and thin film annealing AuNPs/Gr/Si Schottky photodetector

Parameters	Gr/Si	AuNPs/Gr/Si
Based on thermal emission theory		
Ideality factor, η	2.29	5.45
Saturation current, I_0	4.93×10^{-10} A	6.36×10^{-9} A
Schottky barrier height, Φ_B	0.88 eV	0.81 eV
Based on Cheung's function (dV/dlnI - I)		
Ideality factor, η	2.26	5.74
Series resistance, R_s	285 Ω	1775 Ω
Based on Cheung's function (H(I) - I)		
Schottky barrier height, Φ_B	0.91 eV	0.93 eV
Series resistance, R_s	294 Ω	568 Ω
Based on Norde's function		
Schottky barrier height, Φ_B	0.86 eV	0.89 eV

The above results show that, by thin film annealing method, the modification of gold nanoparticles on Gr/Si Schottky photodetector can enhance the photoelectric response in the visible light band. However, compared with the enhancement of the light field intensity by gold nanoparticles in the simulation result, the photocurrent amplitude measured in the experiment is relatively smaller. The photoelectric response of the photodetector is even weaker than that without gold nanoparticles in the wavelength range far away from the surface plasmon resonance peak due to the shielding effect on the incident light and the weak enhancement effect of Au nanoparticles. Meanwhile the deposition and annealing process of Au film has an obvious influence on the interface quality of Schottky junction, which leads to the substantial increase of ideal factor and series resistance. Although the p-type doping of Au on graphene improves the Schottky barrier height, the responsivity of AuNPs/Gr/Si photodetector is still lower than that of Gr/Si photodetector in the UV band of less than 400 nm and the infrared band of more than 800 nm. It is worth mentioning that due to the different enhancement amplitude of Au nanoparticles in different light bands, the

AuNPs/Gr/Si photodetector has a relatively flat current response in a wide spectral range of 500 nm to 900 nm, which enables the photodetector to directly measure and compare the power of different wavelengths without additional conversion. It has certain advantages in the application where the measurement accuracy is not high and convenience is more important, such as portable optical power meter.

4.3 Gold nanoparticles enhanced graphene photodetectors by e-beam lithography

4.3.1 Preparation of gold nanoparticles by e-beam lithography

The gold nanoparticles obtained by different methods have different morphology. As shown in Figure 4-16, the gold nanoparticles obtained by the thin film annealing method are semi-ellipsoidal and randomly distributed on the substrate surface. Although the size and density can be adjusted by the annealing process parameters, the arrangement of the gold nanoparticles are disordered and the size distribution shows great randomness. The method to fabricate gold nanoparticles by electron beam lithography is a typical top-down strategy, and the obtained gold nanoparticles are cylindrical in shape (also called nanodisks) and aligned orderly and uniformly. The height, diameter, periodic distance and other structural parameters of the nanodisks can be pre-designed and precisely controlled. Before the fabrication of gold nanoparticles by electron beam lithography, the optical field distributions of gold nanodisk arrays with different structural parameters were simulated by the finite difference time domain method, and the optimal parameters were obtained for the fabrication.

The nanoparticles was simplified as periodically arranged nanoscale cylinders, as shown in Figure 4-17. The simulation boundary of the selected cell was set as periodic boundary, and the optical field was calculated by finite difference time domain method. The simulation variables are as follows: the radius of nanodisks is 50 nm ~ 100 nm, the height of nanodisks is 10 nm ~ 100 nm, the wavelength of incident light is 300 nm ~ 1700 nm, the periodic distance of nanodisks is 320 nm / 480 nm.

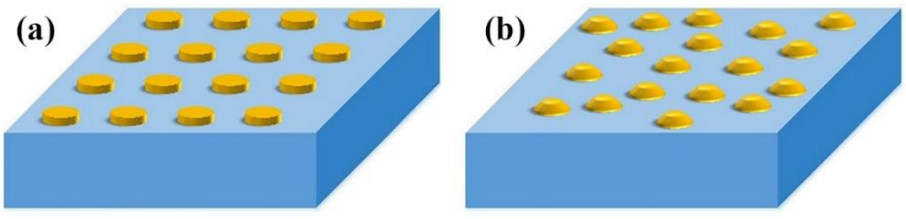

Figure 4-16 The gold nanoparticles fabricated by different methods. (a) Electron beam lithography method. (b) Thin film annealing method.

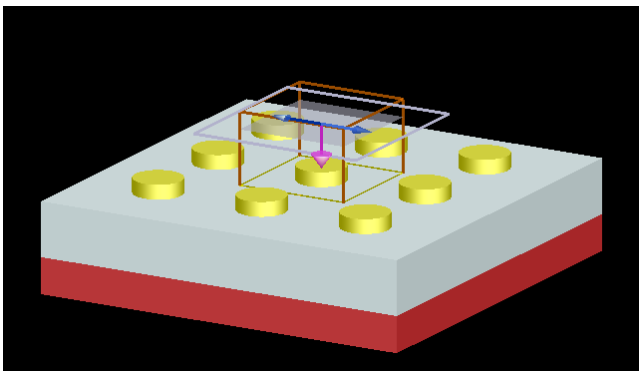

Figure 4-17 The FDTD simulation for The gold nanoparticles fabricated by electron beam lithography.

The transmissivity spectrum and light field intensity of Au nanoparticle arrays with period distance of 320 nm and 480 nm are shown in Figure 4-18 and Figure 4-19 respectively. The abnormal transmission peak can be observed in the transmissivity spectrum, as well as the obvious light field enhancement at the corresponding wavelength in the corresponding light field intensity spectrum.

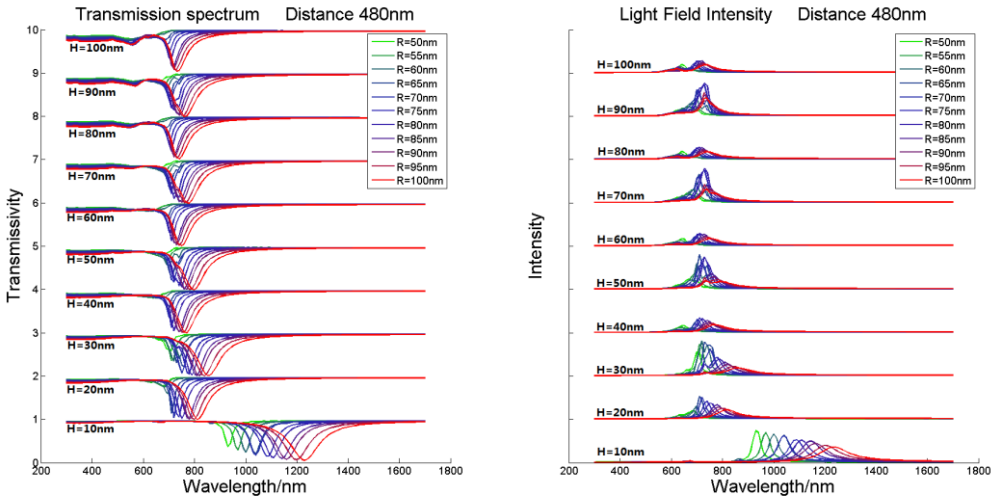

Figure 4-18 The transmissivity and light field intensity as a function of wavelength with the periodic distance of 480 nm. (a) Transmission spectrum. (b) Light field intensity

With the increase of the radius of the gold nanodisks, the anomalous transmission peak shows red shift, especially when the thickness of the gold nanodisks is 10 nm. With the increase of the thickness of the gold nanodisks, the anomalous transmission peak shows blue shift, and the transmissivity decreases in the short wavelength. The decrease becomes more obvious with the increase of the radius, especially when the periodic distance of the gold nanodisks is 320 nm, which is due to the absorption of the incident light by gold. The larger, thicker and denser the nanoparticles are, the more the transmissivity decreases. Because this part of the incident light energy is absorbed by gold, there is no light field enhancement in the corresponding light field intensity spectrum.

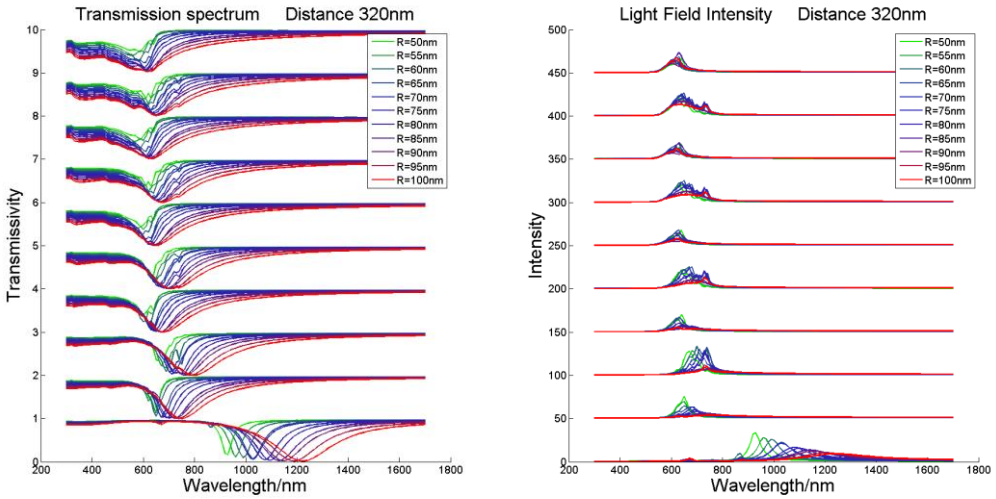

Figure 4-19 The transmissivity and light field intensity as a function of wavelength with the periodic distance of 320 nm. (a) Transmission spectrum. (b) Light field intensity

For the incident light wavelength of 630 nm, when the distance, radius and height of the gold nanodisks are 320 nm, 75 nm and 90 nm respectively, the light field intensity on the surface reaches the maximum value, which is 23 times stronger than that without gold nanoparticles, as shown in Figure 4-20. For the gold nanodisk array with this structural parameter, 630 nm is the wavelength of the abnormal transmission peak, which means that the incident light excites the surface plasmon resonance of the gold nanodisks and focus the incident light energy into the near-field region to enhance the light field intensity, as shown in Figure 4-21. In this circumstance, the transmissivity is 31.3% under 630 nm illumination, and the light field intensity distribution near the gold nanodisks is shown in Figure 4-22.

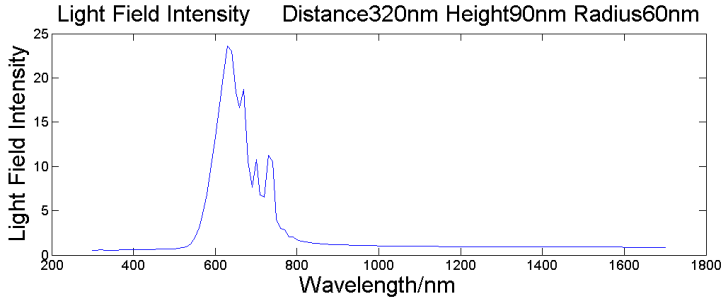

Figure 4-20 The average light field intensity on the surface with the nanodisk distance, radius and height of 320 nm, 75 nm and 90 nm.

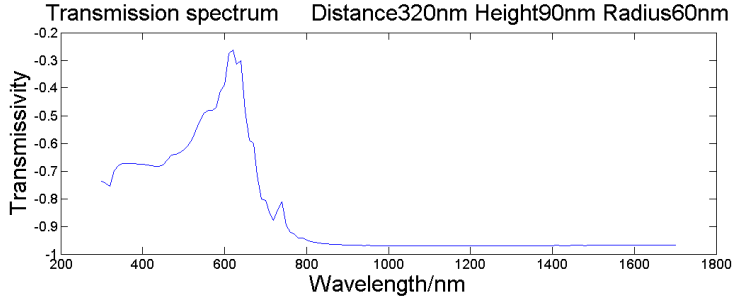

Figure 4-21 The transmission spectrum on the surface with the nanodisk distance, radius and height of 320 nm, 75 nm and 90 nm.

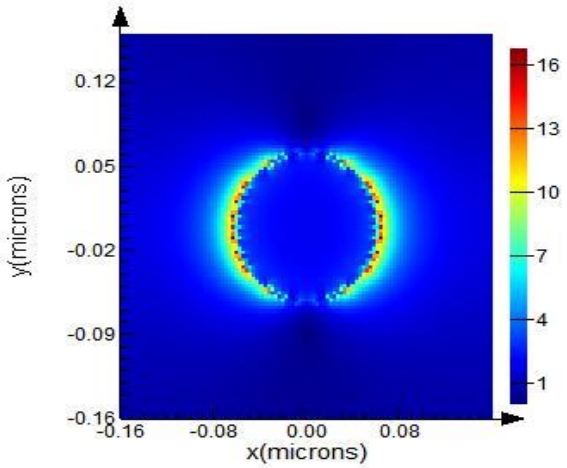

Figure 4-22 The light field intensity distribution near the gold nanodisk.

4.3.2 Fabrication and characterization of gold nanoparticles enhanced photodetectors

Based on the FDTD simulation results, the distance, radius and height of the optimized gold nanodisk array are 320 nm, 75 nm and 90 nm respectively. The gold nanodisks were fabricated to modify the Gr/Si Schottky photodetector by electron beam lithography. The detailed process is as follows:

1) The positive photoresist (AR-P 679.04) was spin coated on the Gr/Si Schottky junction. The spin coating speed and time were 300 rpm for 5 seconds and 2000 rpm for 50 seconds.

2) The electron-beam direct-writing system (CABL-9000C) was utilized to define the pattern. The exposure pattern is an array of circle dots with the periodic distance of 320 nm and the diameter of 60 nm, covering the whole window area of the Gr/Si Schottky photodetector. Because of the diffusion effect, the diameter of the obtained dots is ~150 nm.

3) The exposed sample was developed with the developer (AR 600-56) for 150 seconds.

4) Gold film with the thickness of 90 nm was deposited on the surface of the sample by the electron beam evaporation system (TF500, HHV Ltd).

5) The samples were immersed in acetone to remove the remaining photoresist and the gold film on the photoresist. In the region without photoresist, the gold film was retained, and finally the required gold nanodisk array was obtained.

Scanning electron microscope and atomic force microscope were employed to characterize the morphology of the gold nanodisk array fabricated by e-beam lithography method. As shown in Figure 4-23 and Figure 4-24, the gold nanodisks were arranged orderly, with a diameter of 153 nm, and the periodic distance was 320 nm.

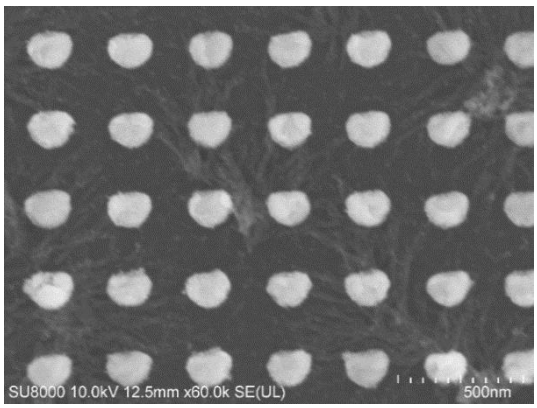

Figure 4-23 SEM image of the gold nanodisk array fabricated by electron beam lithography.

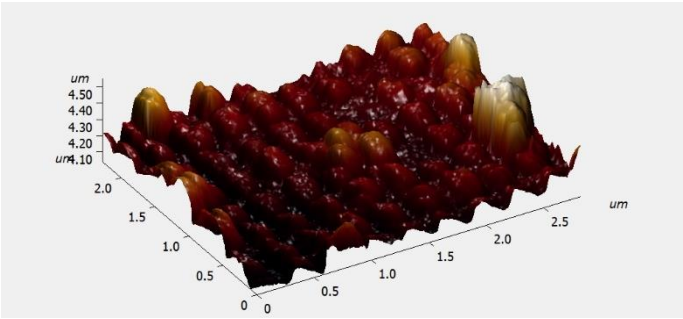

Figure 4-24 The 3D morphology of the electron beam lithography fabricated gold nanodisk array measured by AFM.

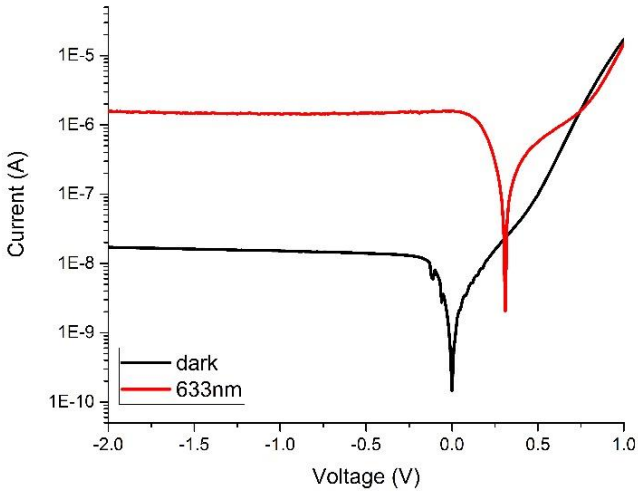

Figure 4-25 The I-V curves of electron beam lithography fabricated AuNPs/Gr/Si Schottky photodetector at room temperature under dark and illumination

The photoelectric response of the gold nanodisk array enhanced Gr/Si photodetector was tested by the semiconductor device analyzer (Keysight B1500A). The sample was connected with the analyzer through a probe station, and a 633 nm semiconductor laser was used as the incident light source. Figure 4-25 shows the current-voltage curves of AuNPs/Gr/Si Schottky photodetectors in the dark and light conditions at room temperature, where the incident light power

density is 160 mW/cm^2. The short circuit current is 83.8 μA and the open circuit voltage is 0.30 V. The dark current is 17.2 nA and the photocurrent is 1.516 mA under the reverse bias voltage of 2 V. The photocurrent responsivity and on/off ratio can be calculated as 0.37 A/W and 8.8 × 10^4 respectively by equation (1-3) and (1-15). As shown in table 4-3, the modified Schottky photodetector shows obvious enhancement compared with that without gold nanoparticles.

Table 4-3 The performance parameters of Gr/Si and AuNPs/Gr/Si Schottky photodetector

Structure	V_{oc} (V)	I_{sc} (μA)	I_d (nA)	I_{ph} (mA)	R (A/W)	$r_{on/off}$
Gr/Au	0.25	20.7	256	0.941	0.23	3.7×10^3
AuNPs/Gr/Si	0.30	83.8	17.2	1.516	0.37	8.8×10^4

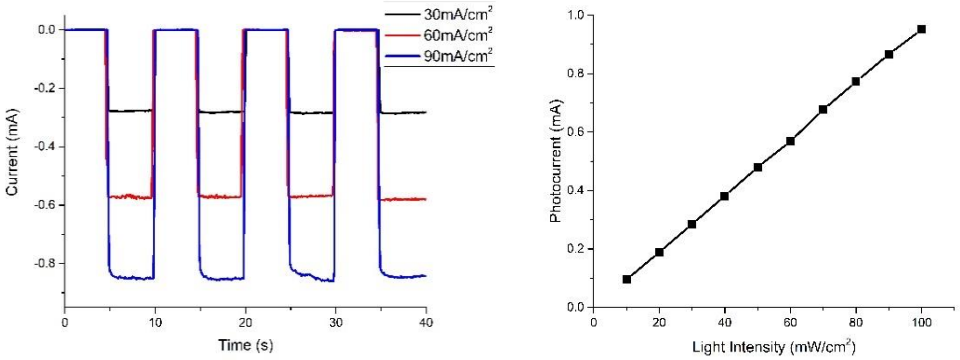

Figure 4-26 The photoreponse of AuNPs/Gr/Si Schottky photodetector. (a) Photoresponse under periodic light signal. (b) Photocurrent as a function of incident light power intensity

The response characteristics of the AuNPs/Gr/Si photodetector under different incident light power intensity are shown in Figure 4-26. For the periodic incident light signals with power density of 30 mW/cm^2, 60 mW/cm^2 and 90 mW/cm^2, the photodetector shows stable photocurrent response. With the increase of the incident light power intensity, the photocurrent increases linearly in the dynamic range of 10 mW/cm^2 ~ 100 mW/cm^2.

The spectral response of the electron beam lithography gold nanoparticles enhanced Gr/Si photodetector is shown in Figure 4-27. It can be seen from the figure that in the visible light band of 350 nm~950 nm, the AuNPs/Gr/Si photodetector shows higher photocurrent response than Gr/Si detector. When the incident light wavelength is 630 nm, the gold nanoparticles have the maximum enhancement for the photodetector, which is consistent with the FDTD simulation results. The photocurrent responsivity increases 61% (from 0.23 A/W to 0.37 A/W). Similar to the AuNPs/Gr/Si photodetector fabricated by thin film annealing, the photocurrent decreases slightly in the short wavelength region of less than 350 nm and the long wavelength region of more than 950 nm due to the shielding of the incident light by gold nanoparticles.

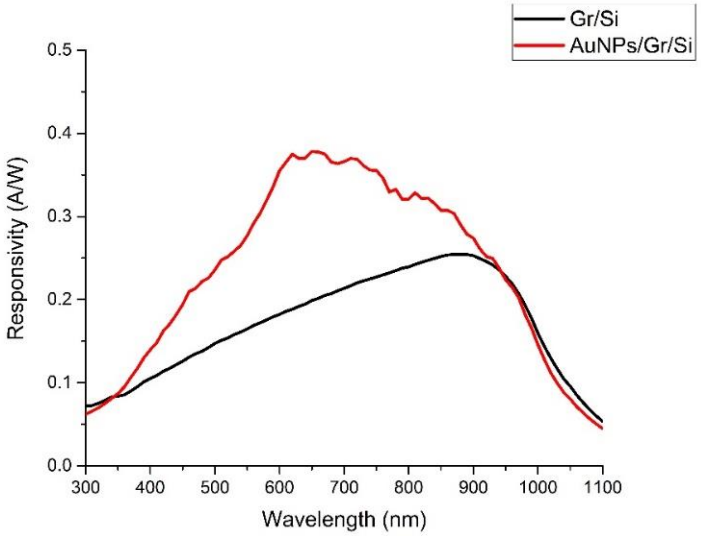

Figure 4-27 The spectral response of AuNPs/Gr/Si Schottky photodetector

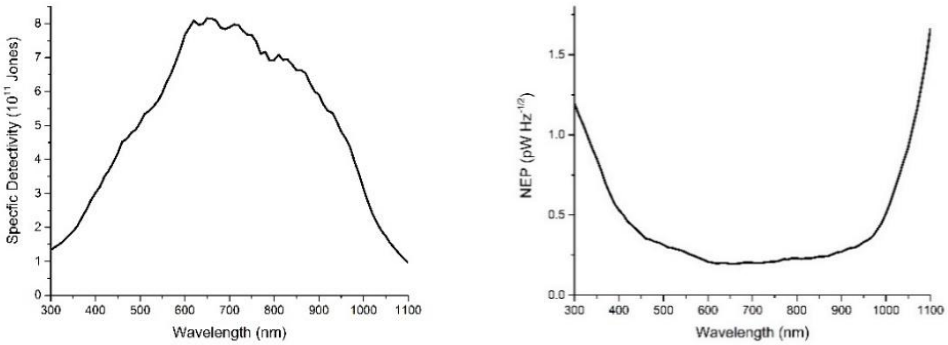

Figure 4-28 The specific detectivity and noise equivalent power of AuNPs/Gr/Si Schottky photodetector. (a) specific detectivity. (b) noise equivalent power.

The specific detectivity and noise equivalent power of the AuNPs/Gr/Si photodetector can be calculated by equation (1-13) and (1-14). As shown in Figure 4-28, when the incident light wavelength is 630 nm, the specific detectivity reaches the maximum value of 8.16×10^{11} Jones, and the noise equivalent power of the detector reaches the minimum value of 0.19 pW $Hz^{-1/2}$.

The semilogarithmic current-voltage curve of the AuNPs/Gr/Si photodetector in dark condition is shown in Figure 4-29. The slope and intercept of its linear fitting are 7.09 and -18.87 respectively. Based on thermal emission theory and equation (2-12), the ideal factor η, reverse saturation current I_0 and Schottky barrier height Φ_B of AuNPs/Gr/Si photodetector are calculated as 3.79 and 4.37 $\times 10^{-10}$ A and 0.88 eV respectively.

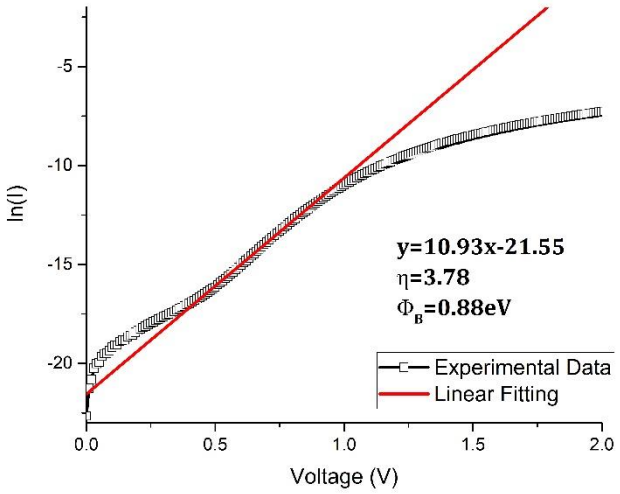

Figure 4-29 The semilogarithmic I-V curves of AuNPs/Gr/Si Schottky photodetector

Based on Cheung's function, the characteristic parameters of the AuNPs/Gr/Si Schottky junction can be extracted from the linear fitting of the dV/dlnI - I and H(I) - I curves. As shown in Figure 4-30 (a), the slope and intercept of dV/dlnI - I fitting line are 264 and 0.0911 respectively, so the ideality factor η and series resistance R_s are calculated as 3.52 and 264 Ω respectively. The slope and intercept of H(I) - I fitting line in Figure 4-30 (b) are 305 and 3.2390 respectively, so the barrier height Φ_B and series resistance R_s are calculated as 0.92 eV and 305 Ω respectively.

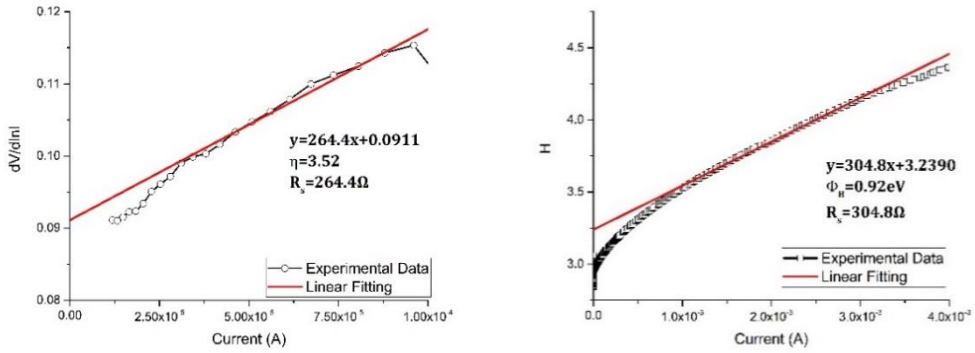

Figure 4-30 The dV/dlnI - I and H(I) - I curves of AuNPs/Gr/Si Schottky photodetector

Similarly, the Schottky barrier height Φ_B of the AuNPs/Gr/Si Schottky junction can also be calculated by Norde's function. According to equation (2-17), the F(V)-V curve of Schottky junction was calculated and plotted. As shown in Figure 4-31, when the bias voltage is 0.11 V, F(V) reaches the minimum value of 0.8439. According to equation (2-18), the barrier height Φ_B of AuNPs/Gr/Si Schottky junction is 0.89 eV.

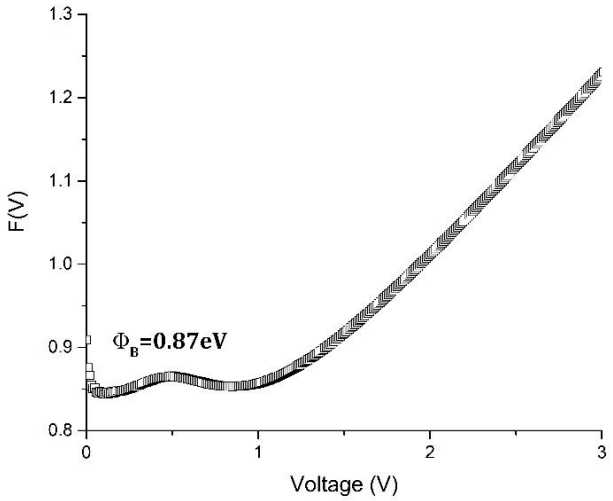

Figure 4-31 The F(V) - V curve of AuNPs/Gr/Si Schottky photodetector

Table 4-4 The performance parameters of Gr/Si and electron beam lithography fabricated AuNPs/Gr/Si Schottky photodetector

Parameters	Gr/Si	AuNPs/Gr/Si
Based on thermal emission theory		
Ideality factor, η	2.29	3.78
Saturation current, I_0	4.93×10^{-10} A	4.37×10^{-10} A
Schottky barrier height, Φ_B	0.88 eV	0.88 eV
Based on Cheung's function (dV/dlnI - I)		
Ideality factor, η	2.26	3.52
Series resistance, R_s	285 Ω	264 Ω
Based on Cheung's function (H(I) - I)		
Schottky barrier height, Φ_B	0.91 eV	0.92 eV
Series resistance, R_s	294 Ω	305 Ω
Based on Norde's function		
Schottky barrier height, Φ_B	0.86 eV	0.87 eV

The comparison of characteristic parameters between Gr/Si and electron beam lithography fabricated AuNPs/Gr/Si Schottky junction is shown in table 4-4. The ideal factor of AuNPs/Gr/Si Schottky junction calculated based on thermal electron emission theory and Cheung's function is larger than that of Gr/Si, which indicates that the interface quality of Schottky junction is negatively affected in the process of homogenization, exposure, development, metal deposition and exfoliation. Nevertheless, the series resistance does not change significantly, which indicates that the structure of graphene is unscathed and still has good conductivity. Similar to the AuNPs/Gr/Si Schottky junction fabricated by gold thin film annealing, the value of Schottky barrier height Φ_B increases due to the p-type doping of graphene by Au nanoparticles. However, compared with the gold nanoparticles fabricated by thin film annealing method, the contact area between the electron beam lithography fabricated gold nanodisk arrays and graphene is much smaller, which only exists at the bottom of the nanodisks. As a result, the

doping of graphene is weak, so the Schottky barrier height Φ_B is only slightly increased (~ 0.1 eV). Based on the equation (2-9), the reverse saturation current of AuNPs/Gr/Si Schottky junction decreases slightly due to the increase of Schottky barrier height Φ_B.

4.4 Summary

In this chapter, AuNPs were fabricated by thin film annealing and electron beam lithography respectively and used to enhance the performance of Gr/Si Schottky photodetector. The gold nanoparticles with subwavelength size on the surface of Gr/Si photodetector can excite the local surface plasmon resonance and enhance the intensity of the local light field under the incident light. In addition, the doping effect of gold on graphene also improves the Schottky barrier height and promotes the separation of photogenerated carriers. They work together to enhance the performance of the photodetector. The random distributed semi-ellipsoidal AuNPs with no adhesion was obtained by thin film annealing. The AuNPs enhanced graphene oxide Raman spectrum proves the existence of surface plasmon and the enhancement of the near-field light field. The FDTD simulation results also show that the intensity of the near-field light field can be significantly enhanced by gold nanoparticles. The gold thin film annealed AuNPs are utilized to modify the Gr/Si Schottky photodetector. When the incident light wavelength is 500 nm, the enhancement of AuNPs reaches maximum, and the photocurrent responsivity is increased by 48%. The analysis of the characteristic parameters of the Schottky junction shows that the Schottky barrier height Φ_B increases significantly due to the p-type doping of graphene by Au nanoparticles. The increase of the ideal factor η and the series resistance R_s indicates that the structure of graphene and the interface of the Schottky junction are partly damaged by the annealing process.

The AuNPs obtained by electron beam lithography are well-ordered gold nanodisk array. The diameter, height and periodic distance of the gold nanodisks were optimized by FDTD simulation, and the corresponding AuNPs were fabricated by electron beam lithography to modify the Gr/Si Schottky photodetector. When the incident light wavelength is 630 nm, the enhancement of AuNPs reaches maximum, which is consistent with the result of FDTD simulation, and the responsivity of the photodetector increases by 61%. The analysis of the characteristic parameters of the Schottky junction shows that due to the limited contact area between the gold nanodisks and graphene, the doping of graphene by gold nanodisks only slightly increases the Schottky barrier height Φ_B. Meanwhile, the series resistance R_s remains almost unchanged, and the increase of the ideal factor η is smaller than that of the thin film annealing AuNPs/Gr/Si Schottky junction, which indicates that the AuNPs/Gr/Si Schottky junction fabricated by the electron beam lithography method has relatively less damage to the Schottky junction.

Both thin film annealing method and electron beam lithography method can fabricate gold nanoparticles to improve the photodetection performance of Gr/Si

Schottky junction. The former is simple, but the obtained AuNPs are randomly distributed, and the annealing process to some content has a damage to the Gr/Si Schottky junction. The latter can obtain a well-ordered gold nanodisk array and avoid the damage of high temperature annealing to the material and device, but it is complicated, costly, and time consuming. This chapter verifies the effect of gold nanoparticles on the performance improvement of Gr/Si photodetector. This method modifies the photosensitive surface of photodetector, which is suitable for not only Schottky junction photodetectors, but also other types of photodetectors. The morphologies of AuNPs fabricated by the two methods are different, as well as their enhancement extent and wavelength range, which can be used in different applications.

Chapter 5

Graphene/silicon Schottky photodetector based on direct transfer of graphene by hot embossing

5.1 Introduction

The most common method to fabricate graphene/silicon Schottky junction devices is to use PMMA as a temporary support layer to transfer graphene from the original metal substrate to the silicon substrate [78, 127, 163-165]. This method requires meticulous manual operation, which is difficult to be compatible with semiconductor manufacturing process, and it is easy to cause wrinkles and folds in the procedure of picking up graphene. In addition, PMMA residue will increase the density of surface defects, resulting in device performance degradation. In order to solve this problem, researchers have proposed a variety of methods to eliminate the influence of PMMA residues, such as deep ultraviolet irradiation [78, 163], Ar ion beam treatment [164], using low molecular weight PMMA [165], etc., while all of these methods increase the complexity of the process.

Hot embossing is a cost-effective and flexible fabrication technology which has been widely used for micro-/nano- fabrication, but it has been used only recently to transfer CVD grown graphene[166]. By applying this novel method, CVD grown graphene was directly transferred from copper foil to Cyclic Olefin Copolymer (COC) foil without PMMA sacrificial layer, which avoids the residues of PMMA and simplifies the processing steps, thus providing the opportunity for large scale production. The success of hot embossing graphene transferring benefits from the nature of the polymer material, which is flexible and able to contact well with graphene on original metal substrate under a certain pressure

and temperature. As a result, this method was proposed to fabricate flexible graphene device, while is not suitable for the fabrication of graphene device on hard substrate.

In this chapter, hot embossing process was employed twice to transfer graphene and fabricate Gr/Si Schottky photodiodes. As a direct graphene transfer technique, CVD monolayer graphene was transferred by hot embossing from copper foil to COC foil, and hot embossing was employed once again to bond graphene/COC with as-prepared substrate and form Schottky contact in the window area. The transparent COC foil remains on the top of photodetector and protects graphene from external pollution. The incident light goes through transparent COC and graphene layer, and finally excites electron–hole pairs in silicon, which is the origin of photoelectrical response of Gr/Si Schottky photodetector. The photoelectric characteristics reveal that the Gr/Si Schottky diode fabricated by hot embossing has equivalent or even better performance as those fabricated by traditional method, which provides a simple and reliable approach for the fabrication of graphene based devices.

5.2 Fabrication of graphene/silicon photodetector by two-step hot-embossing method

5.2.1 Synthesis of graphene and transferring to COC substrate

After rinsing Cu foils in 10% HCl for 15 min, single layer graphene was grown on them in a CVD system (Moorfield NanoCVD 8G). The Gr/Cu was then hot embossed onto a COC foil (140 μm, TOPAS 8007 × 04). This process was performed with a hot embossing system (model HEX01JENOPTIK Mikrotechnik) with the temperature of 80 °C and the applied force of 10,000 N for 120 seconds. Since the surface was 2 cm×2 cm, the pressure was 25 MPa. Then the Cu layer was wet etched by $FeCl_3$ solution and the samples were rinsed in deionized (DI) water to remove $FeCl_3$ residues, thus graphene on COC was obtained.

5.2.2 Fabrication of graphene/silicon photodetector

The fabrication process of hot embossing transferred Gr/Si Schottky photodetector is shown in Figure 5-1. N-type Si (100) wafer (1–10 Ω cm) with 300 nm SiO_2 was used as the substrate for the fabrication of Schottky junction. Firstly, the SiO_2 layer on the backside was removed by HF etching, and Ti/Au (20nm/80nm) was deposited by e-beam evaporation to form ohmic contact. After that, Cr/Au (20nm/80nm) electrode was patterned and evaporated on the front side of SiO_2/Si wafer. Photolithography was used to define a square window on the substrate (1.6mm×1.6mm), followed by a wet etching process in buffered oxide etch (BOE) solution to remove SiO_2 layer. Then hot embossing was used once again to bond graphene with the prepared silicon substrate to form Schottky contact in the window, which was the active area of this photodetector.

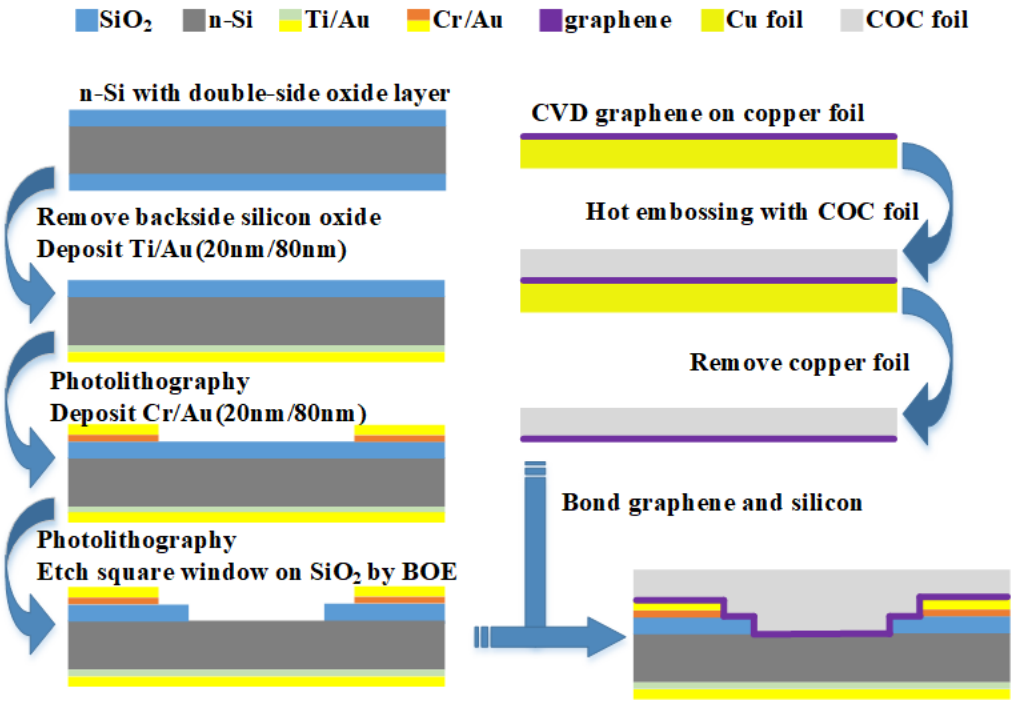

Figure 5-1 Fabrication process of hot embossing transferred Gr/Si Schottky photodetector

5.3 Measurement and analysis

Raman microscope (Renishaw plc, Wotton-under-Edge, UK) with a 532nm laser and a Leica DMLM microscope was used to characterize the graphene transferred by hot embossing process. The spectrum of COC foil was obtained in advance and was taken off from that of graphene on COC to get the contribution of graphene alone.

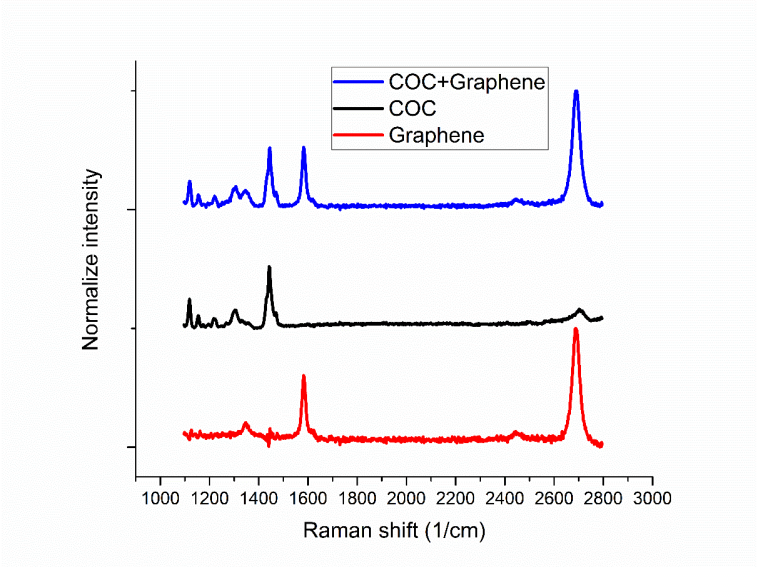

Figure 5-2 Raman spectrum of hot embossing transferred graphene

The Raman spectrum of the graphene transferred on COC foil by hot embossing (Figure 5-2) shows three main peaks: D peak at 1346 cm^{-1}, G peak at

1582 cm^{-1}, 2D peak at 2678 cm^{-1}. The 2D peak is sharp and symmetric, the full width at half maximum of the 2D peak is 35 cm^{-1} and the intensity ratio of the 2D peak to the G peak is 1.75. The shape of the peaks and the intensity ratio indicate the monolayer nature of this graphene thin film[137, 138, 167]. From the Raman spectrum it can be seen that the graphene structure is well preserved after experiencing the 25 MPa molding pressure during hot embossing process.

Keysight B2912A Source/Measure unit was used for electrical characterizations, and photoelectrical characterization was carried out under dark and 633 nm illumination with a semiconductor laser (laser power has been calibrated with Sanwa LP-1 before the measurements).

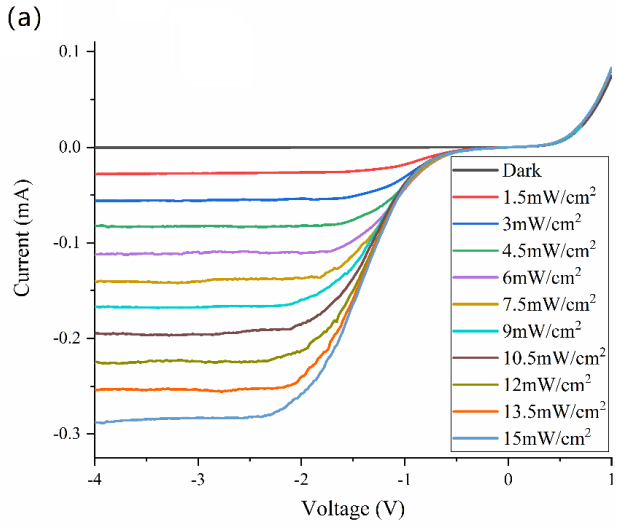

Figure 5-3 I–V curves of the Gr/Si photodetector under various incident light power intensity

As shown in Figure 5-3, I–V measurements were carried out under different incident light intensity from 0 to 15 mW/cm^2. The curves exhibit typical rectifying behavior and Gr/Si Schottky junction works in the backward voltage segment, which is similar to that of a metal/semiconductor Schottky diode. From the family of I-V curves we can see that the photocurrent of the device is highly dependent on the bias voltage: for a certain incident light power, the photocurrent rises with the increase of reverse bias and saturates at higher reverse bias. This phenomenon origins for the photovoltaic characteristic of Gr/Si Schottky junction, which can be understood from the energy band diagram.

As shown in Figure 5-4, E_c, E_v, E_F, E_g, Φ_G, χ_{Si}, Φ_B, Φ_i are the bottom of conduction band, the top of valence band, Fermi level, band gap, work function, electron affinity, Schottky barrier height, and built-in potential, respectively. At the graphene/silicon interface, the incident photons are absorbed by silicon and excite electron–hole pairs, which are separated by the built-in potential and transported efficiently to the external electrode under the appropriate biases, where graphene acts as a carrier collector and a high-speed channel for photo-generated carriers due to its low light absorbance. While the built-in potential, Φ_i, is related to the bias voltage, as shown in Figure 5-4(b), the ability of charge

separation can be tuned by the bias and a relatively large built-in potential is favorable for injecting all of the photoexcited holes from silicon to graphene and obtaining the saturated photocurrent.

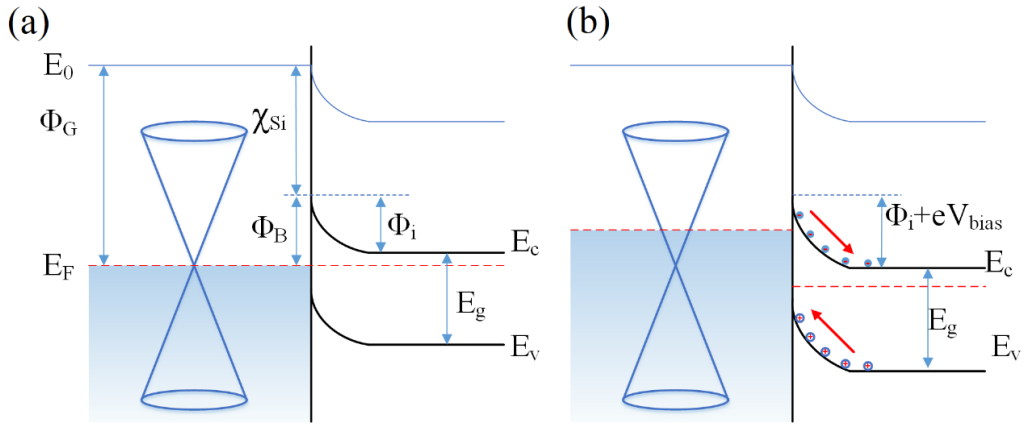

Figure 5-4 Energy band diagram of the Gr/Si Schottky junction. (a) Thermal equilibrium energy band diagram of the heterojunction in darkness. (b) Reverse bias under illumination.

While an appropriate reverse bias is applied on the Gr/Si Schottky junction, the saturated photocurrent increases linearly with the incident light intensity. Figure 5-5 displays the time dependent photoresponse to a pulse optical signal of various intensity with the reverse bias voltage of -3V, which shows the reliability and stability of the hot embossing fabricated Gr/Si photodiode. Based on equation (1-3), the responsivity of the hot embossing Gr/Si Schottky photodetector is calculated as 0.73 A/W.

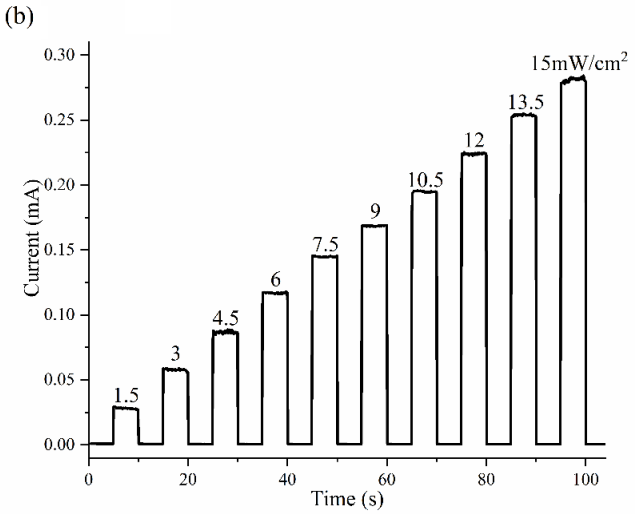

Figure 5-5 Time dependent photocurrent response of the Gr/Si photodetector.

Based on thermal emission theory, the characteristic parameters of the hot embossing fabricated Gr/Si Schottky junction are calculated from the measured current-voltage response to evaluate the its performance. The semi log current-voltage curve of the photodetector under dark condition is shown in Figure 5-6, as well as its linear fitting. The slope and intercept of the fitting line are 19.84 and -22.58 respectively. According to equation (2-12), the ideal factor η, reverse

saturation current I_0 and Schottky barrier height Φ_B of AuNPs/Gr/Si photodetector can be calculated to be 1.95 and 1.55 $\times 10^{-10}$ A and 0.91 eV respectively.

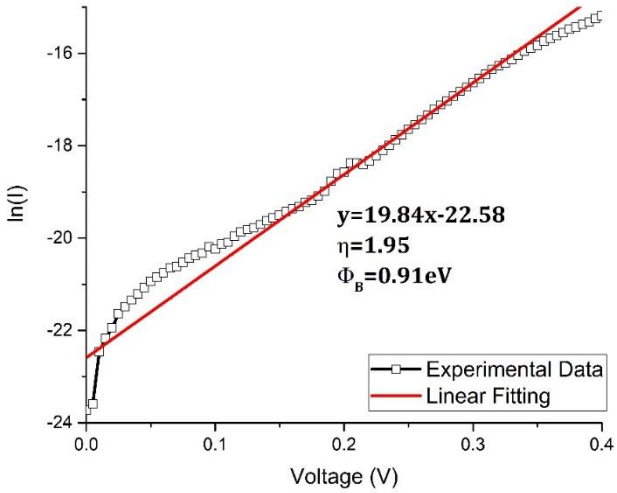

Figure 5-6 The semilogarithmic I-V curves of Gr/Si Schottky photodetector fabricated by hot embossing method.

To further investigate the hot embossing Gr/Si Schottky photodetector, the Schottky characteristic parameters are extracted from current-voltage measurement by Cheung's function. Plots of dV/dlnI - I and H(I) - I for the Gr/Si Schottky diode are presented in Figure 5-7. From the plot of dV/dlnI - I (Figure 5-7(a)), the values of series resistance and ideality factor are determined to be 2132 Ω and 2.66 from the intercept and slope of the forward bias. Using the value of ideality factor obtained from dV/dlnI - I plot, the Schottky barrier height is estimated by equation (2-5) from the H(I) - I plot (Figure 5-7 (b)). Φ_B and R_s are found to be 1.01 eV and 2153 Ω. The R_s values obtained from the both plots are almost the same, which can be attributed to the consistency of Cheung's functions[148, 168].

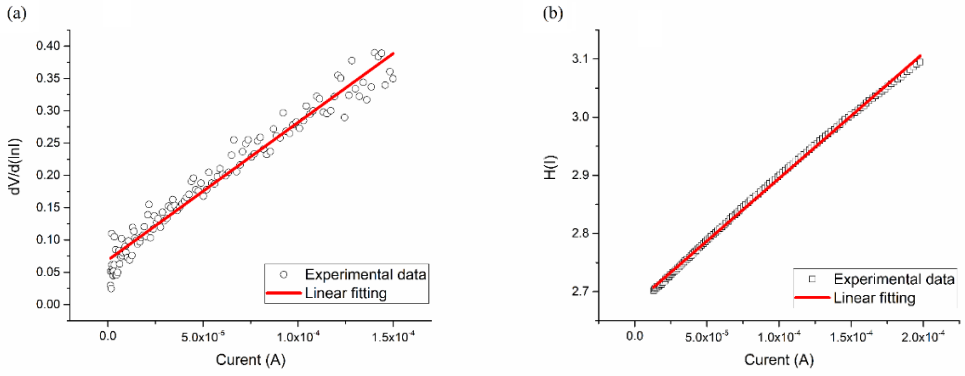

Figure 5-7 The dV/dlnI - I and H(I) - I curves of Gr/Si Schottky photodetector

The Schottky barrier height Φ_B can also be calculated by Norde's function. The F(V)-V curve of Schottky junction was calculated and plotted in Figure 5-8. According to equation (2-18), the barrier height Φ_B of AuNPs/Gr/Si Schottky junction is 0.88 eV.

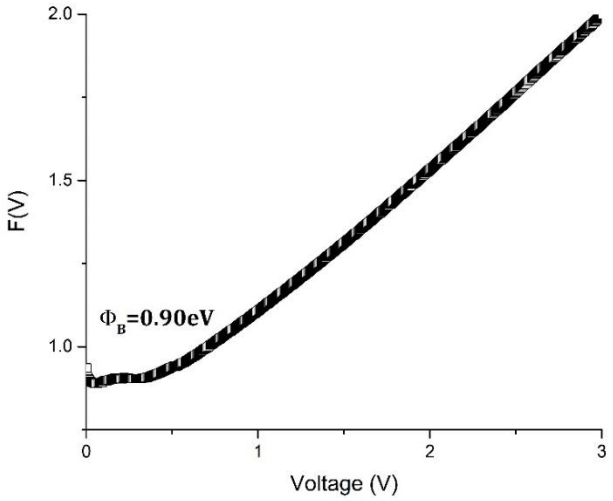

Figure 5-8 The F(V) - V curve of Gr/Si Schottky photodetector

Table 5-1 The performance parameters of Gr/Si Schottky photodetectors fabricated by traditional method and hot embossing method

Parameters	Traditional Gr/Si	Hot embossed Gr/Si
Based on thermal emission theory		
Ideality factor, η	2.29	1.95
Saturation current, I_0	4.93×10^{-10} A	1.55×10^{-10} A
Schottky barrier height, Φ_B	0.88 eV	0.91 eV
Based on Cheung's function (dV/dlnI - I)		
Ideality factor, η	2.26	2.66
Series resistance, R_s	285 Ω	2132 Ω
Based on Cheung's function (H(I) - I)		
Schottky barrier height, Φ_B	0.91 eV	1.01 eV
Series resistance, R_s	294 Ω	2153 Ω
Based on Norde's function		
Schottky barrier height, Φ_B	0.86 eV	0.88 eV

The characteristic parameters of Gr/Si Schottky junction fabricated by traditional method and two-step hot embossing method are shown in Table 5-1. The series resistance of two-step hot pressing Gr/Si is obviously higher, which may be due to the existence of submicron step at the edge of the silicon window. The step height is about 300 nm, which is equal to the thickness of the SiO_2 layer. During the hot embossing process, the graphene near the step suffers from tensile stress concentration, which leads to the decrease of the graphene conductivity and the increase of the series resistance of the Schottky junction. In addition, the Schottky barrier height Φ_B calculated by the three different methods is higher than that of Gr/Si fabricated by the traditional method. It is because that there is no PMMA residue on the surface of directly transferred graphene films by hot embossing method, which reduces the surface defect density and avoids the influence of Fermi pinning effect on the Schottky barrier. At the same time, the decrease of surface defect density also reduces the recombination of photo

generated carriers, which can improve the photoelectric detection ability of the Gr/Si photodetector.

Table 5-2 lists the performances of graphene based photodetectors, most of them are graphene/silicon Schottky structure, some surface modified graphene devices and graphene heterojunction with other materials are also included, it can be seen that the hot embossing fabricated Gr/Si shows the same level of photo detecting ability with the ones already published.

Table 5-2 Comparison of the performances of the graphene based photodetectors

Structure	R	Φ_B	R_s	η	Ref
Gr/Si	0.73 A/W	1.01 eV	2 kΩ	2.66	This work
Gr/Si	0.73 A/W	—	—	—	[125]
Gr/Si	230 mA/W	0.66 eV	6.7 kΩ	1.52	[94]
Gr/Si	435 mA/W	—	—	—	[87]
Gr/Si	140 mA/W	0.79 eV	32.1 Ω	2.24	[162]
Gr/Si	214 mA/W	0.79 eV	—	2.1	[132]
Gr/Si	152 mA/W	—	—	—	[113]
Gr/Si	142 mA/W	0.79 eV	14.9 Ω	—	[127]
Gr/Si	0.24 A/W	—	—	—	[134]
Gr/Si-tips	2.5 A/W	0.36 eV	4.5 kΩ	—	[145]
PEDOT-Gr/Si	172 mA/W	—	—	—	[113]
P3HT–Gr/Si	0.78 A/W	—	—	—	[134]
TFSA-Gr/Si	252 mA/W	0.89 eV	10.3 Ω	—	[127]
MoO3-Gr/Si	400 mA/W	0.86 eV	17.1 Ω	1.3	[162]
Gr/GO/Si	266 mA/W	0.81 eV	—	2.6	[132]
Gr/Au	225 mA/W	—	—	—	[82]
Gr/Ge	51.8 mA/W	—	—	—	[169]

In a Schottky photodiode, photogenerated electron-hole pairs are separated by a built-in electric field, which is associated with the Schottky barrier[130, 170, 171], thus the responsivity of 0.73 A/W was obtained with the high Schottky barrier height of 1.01 eV. Although the series resistance is higher than the traditional Gr/Si photodetector fabricated by PMMA graphene transfer, the sensitive, quick and stable photoresponse indicate the feasibility and effectiveness of this hot embossing fabrication process, which provides a new approach for graphene devices.

5.4 Summary

In this chapter, two-step hot embossing method was proposed to transfer graphene and to fabricate Gr/Si Schottky photodetector. As a direct graphene transfer technique, through a hot embossing system, CVD Graphene monolayer was transferred without any sacrificial layers, which avoid the PMMA residue on graphene surface. The Raman spectrum shows that the graphene structure is well preserved after experiencing the 25 MPa molding pressure during hot embossing process. In the second hot embossing process, graphene is bonded with the prepared silicon substrate to form Schottky contact.

The photoelectric characterizations show that the photocurrent increases linearly with the increase of the incident light power density under the irradiation of 633nm light. The Gr/Si photodetectors prepared by the same process parameters show good consistency, which indicates the stability and reliability of two-step hot embossing method. With an appropriate bias voltage, the maximum responsivity reaches 0.73 A/W. Extracted from I-V characteristics by Cheung's function, the Schottky barrier height, ideality factor and series resistance are 1.01 eV, 2.66 and 2 kΩ, respectively. As the separation of photogenerated carriers is closely related to the built-in potential of Schottky junction, a higher barrier height is helpful for higher photoelectric response. These results show that the two-step hot embossing method proposed in this chapter is feasible and effective for the fabrication of Gr/Si Schottky photodetector, which provides a new approach for graphene optoelectronic devices and demonstrates the possibility of large-scale industrial production.

Chapter 6

Conclusions and Prospects

6.1 Conclusions

In this thesis, the monolayer graphene synthesized by chemical vapor deposition was used to fabricate Gr/Si Schottky photodetectors. The insertion of graphene oxide interlayer and the modification by gold nanoparticles are utilized to enhance the performance of the Gr/Si photodetectors. The two-step hot embossing method was proposed to directly transfer graphene and fabricate Gr/Si Schottky photodetector. The main research work is as follows:

1) Monolayer graphene films were synthesized by chemical vapor deposition, and utilized to fabricate Gr/Si Schottky photodetectors. The results of Raman spectroscopy, SEM and AFM indicate the monolayer structure of the synthesized graphene. After transferring graphene via PMMA temporary support layer, the graphene still has good integrity and continuity, but there is PMMA residue with a thickness of ~5 nm on the graphene. The metal-graphene-metal structure verifies the photoelectric detection ability of the as-prepared graphene, but the low light absorption of graphene limited its photodetection performance. Then Gr/Si Schottky photodetector was fabricated by the CVD grown graphene. For the incident light with wavelength of 633 nm, the photocurrent responsivity of the Gr/Si photodetector is 0.23 A/W, and the on/off ratio is 3.7×10^3. The photodetector can quickly and accurately respond to the incident light with different power density, and the response time is about 1 ms. The spectral response shows that the responsivity reaches the maximum at about 900 nm, and the cutoff occurs at 1100 nm, which indicates that the absorption of incident light in the Gr/Si Schottky photodetector is dominated by silicon. Considering the intrinsic relationship between the photoelectric detection performance of the photodetector and the characteristics of the Gr/Si Schottky junction, three methods were introduced to extract the characteristic parameters of the Gr/Si Schottky junction, including thermal emission equation, Cheung's function and Norde's function. The ideal factor and Schottky barrier height obtained from the

thermal emission equation are 3.44 and 0.82 eV, respectively. The series resistance, ideal factor and Schottky barrier height calculated by Cheung's function are ~300 Ω, 2.26 and 0.91 eV, respectively. The Schottky barrier height based on Norde's function is 0.86 eV.

2) The performance of Gr/Si Schottky photodetector was enhanced by inserting graphene oxide film as interlayer. The I-V characteristic shows that the dark current of Gr/GO/Si Schottky photodetector is 26 times lower than that of Gr/Si photodetector, and the photocurrent is 2.73 times higher than the Gr/Si photodetector. Under 633 nm illumination, the responsivity of the Gr/GO/Si photodetector is 0.65 A/W with the reverse bias voltage of 2 V. Benefiting from the suppression of dark current and the improvement of photocurrent, the on/off ratio of the detector is as high as 2.73×10^5, the specific detectivity and noise equivalent power are 1.88×10^{12} Jones and 0.09 pW/Hz$^{1/2}$, respectively, which has obvious advantages comparing with the similar devices reported in the literature. The photocurrent of the Gr/GO/Si photodetector increases linearly with the incident light power density, and it responds quickly and accurately to the periodic light signal. Meanwhile, the response speed remains unchanged after inserting GO interlayer, both of the rise time and fall time of the photoelectric response are about 1 ms. Based on thermal emission equation, Cheung's function and Norde's function, the current-voltage characteristics of the device are analyzed to reveal the influence of GO interface layer on the Gr/Si Schottky photodetector. With the insertion of GO interlayer, the series resistance is almost unchanged, the ideal factor value decreases, while the Schottky barrier height and shunt resistance increase significantly, which suppresses the reverse saturation current and decreases the dark current. The photocurrent increment of Gr/GO/Si photodetector is affected by many factors, including the increase of Schottky barrier height, the extra optical absorption of GO layer and the passivation of Schottky junction interface. In summary, the GO interlayer have dual effects on suppressing the dark current and improving the photocurrent of the Gr/Si Schottky photodetector.

3) AuNPs fabricated by thin film annealing and electron beam lithography are utilized to enhance the performance of Gr/Si Schottky photodetector. The disordered gold nanoparticles obtained by thin film annealing method are semi ellipsoids with the diameter of 40 nm ~ 60 nm and the height of 3 nm ~ 6 nm, which can significantly improve the responsivity of the photodetector in the visible light band. When the incident light wavelength is 500 nm, the enhancement rate reaches maximum, and the responsivity increases 48% (from 0.15 A/W to 0.22 A/W). When the incident light wavelength is 610 nm, the photodetector has the maximum current responsivity of 0.24 A/W. The AuNPs fabricated by electron beam lithography are well-ordered gold nanodisk array, and the structural parameters are optimized by FDTD simulation. The gold nanodisk array with distance, radius and height of 320 nm, 75 nm and 90 nm have a light field intensity increase of 23 times for 630 nm incident light, and the responsivity increases 61% (from 0.23 A/W to 0.37 A/W). At the same time, the on/off ratio, detectivity, noise equivalent power and other performance parameters of the

photodetector are also improved. For both of the AuNPs/Gr/Si photodetectors fabricated by the two methods, the Schottky barrier height Φ_B increases significantly due to the p-type doping of graphene by gold, which reduces the dark current of the detector. While the negative influence on the surface of graphene and Schottky junction interface by the fabrication of AuNPs increases the ideal factor η and series resistance R_s. In summary, the morphologies of AuNPs fabricated by thin film annealing method and electron beam lithography method are different, but both of them show significant enhancement on the photoelectric response of Gr/Si photodetector, which can be used in different applications.

4) A new method of directly transferring graphene and fabricating Gr/Si Schottky photodetector is proposed. In this method, without the assistance of PMMA and other temporary support layer, graphene is directly transferred to the COC substrate by hot embossing, and then the COC/graphene structure is embossed with the silicon substrate with prefabricated window and electrode by using hot embossing process once again. The graphene and silicon contact through the window area to form Gr/Si Schottky junction. The Raman spectrum of graphene before and after hot embossing show that the structure of graphene remains intact after experiencing the 25 MPa molding pressure during hot embossing process. The photoelectric characteristics show that the photocurrent increases linearly with the incident light power density under the irradiation of 633 nm light source, and the responsivity reaches 0.73 A/W under the appropriate reverse bias voltage. The series resistance of Gr/Si Schottky junction fabricated by two-step hot embossing method is significantly higher than that by traditional method, which may be caused by tensile stress concentration on graphene at the edge of silicon window. Because there is no PMMA residue on graphene, the density of surface defects is relative low, which avoids the Fermi pinning effect on Schottky barrier, increases the Schottky barrier height, and reduces the recombination of photogenerated current carriers, thus significantly increases the responsivity of the photodetector. The above results show that the two-step hot embossing method is feasible and effective for the fabrication of Gr/Si Schottky photodetector. This work provides a new approach for the fabrication of graphene optoelectronic devices and shows the possibility of large-scale production.

6.2 Innovation

1) It is proposed in this thesis to modify the Gr/Si Schottky photodetector by graphene oxide interlayer, which can suppress the dark current and increase the photocurrent of the photodetector. At present, most of the reports on interface modified Gr/Si photodetector use silicon oxide as the interlayer material. Silicon oxide interlayer has simple preparation process and good compatibility with silicon substrate. It can even obtained by simply exposing silicon to air at room temperature. Although the SiO_2 interlayer can effectively suppress the dark current of the Gr/Si detector, it has no obvious improvement on the photocurrent. In this thesis, GO interlayer has dual effects on suppressing the dark current and improving the photocurrent of the Gr/Si Schottky photodetector.

2) It is proposed in this thesis that the AuNPs fabricated by thin film annealing method and electron beam lithography method can enhance the performance of Gr/Si Schottky photodetector. The light field enhancement effects of two kinds of AuNPs are analyzed by FDTD simulation, the photoelectric characteristics of two kinds of AuNPs/Gr/Si photodetectors are measured, and the difference of their enhancement effect on photodetector performance is compared and analyzed. The results show that the thin film annealing AuNPs/Gr/Si has a relatively flat responsivity spectrum in the visible light band, while the electron beam lithography AuNPs/Gr/Si has a higher responsivity increase at the resonance peak of 630 nm.

3) The two-step hot embossing method to directly transfer of graphene and fabricate Gr/Si Schottky photodetectors is proposed. Since high quality CVD graphene still needs to be grown on metal substrates, it is necessary to transfer graphene to other substrates before it can be used for device fabrication. At present, PMMA as temporary support layer is the most commonly used for graphene transfer, but this method requires experienced and meticulous manual operation, which is not suitable for large-scale production, and PMMA residue usually leads to device performance degradation. The hot embossing process is widely used in micro/nano fabrication and has good compatibility with silicon micromachining process. In this thesis hot embossing is utilized to directly transfer of graphene and fabricate Gr/Si Schottky photodetector, demonstrating the probability of large-scale production for graphene based devices.

6.3 Prospects

This thesis studies the graphene/silicon Schottky photodetector, including the CVD growth of graphene and the fabrication of Gr/Si Schottky photodetectors, the enhancement of Gr/Si photodetectors by GO interlayer and AuNPs surface modification, and the two-step hot embossing method of directly transferring graphene and fabricating Gr/Si photodetector. To further improve the performance of Gr/Si Schottky photodetector and promote the application of the proposed methods in this thesis, further research will be carried out in the following aspects.

1) Use nanocomposite as the interlayer to enhance the performance of Gr/Si photodetector. At present, the research of Gr/Si interlayer is based on a single kind of material, using composite material as interlayer may further improve the performance of Gr/Si photodetector.

2) Combine multiple methods to realize further enhancement of Gr/Si photodetector. The performance enhancement methods of Gr/Si photodetector include three categories: the improvement of silicon structure, the optimization of graphene/silicon interface and the modification of graphene surface. In theory, there is no conflict between them, and the Gr/Si photodetector can be improved by the combination of them. In practical terms, however, the combination of multiple enhancement methods will make the device structure more complex, the process compatibility of each part of the structure needs to be considered, especially graphene is easy to be affected by the external environment as a two-dimensional

material with single atomic layer thickness. Therefore, the fabrication process with the combination of multiple enhancement methods should be well designed to further improve the performance of Gr/Si photodetector.

3) Nanoimprint lithography could be combined with the two-step hot embossing method to improve the performance of Gr/Si photodetector. Nanoimprint lithography can fabricate nanostructure on COC surface to reduce the light reflection and increase the light transmission. Through the exquisite design of nanostructures, such as nano-grating or multi-annular structure, the incident light can be focused in the active area of the Gr/Si photodetector to improve the photoelectric response.

References

[1] Pearton SJ, Zolper JC, Shul RJ, et al. GaN: Processing, defects, and devices[J]. Journal of Applied Physics. 1999, 86(1): 1-78.

[2] Razeghi M, Rogalski A. Semiconductor ultraviolet detectors[J]. Journal of Applied Physics. 1996, 79(10): 7433-7473.

[3] Monroy E, Omn S F, Calle F. Wide-bandgap semiconductor ultraviolet photodetectors[J]. Semiconductor Science and Technology. 2003, 18(4): R33-R51.

[4] Rogalski A. Infrared detectors: status and trends[J]. Progress in Quantum Electronics. 2003, 27(2): 59-210.

[5] Renker D, Lorenz E. Advances in solid state photon detectors[J]. Journal of Instrumentation. 2009, 4(04): P4004.

[6] Morkoç H, Strite S, Gao GB, et al. Large‐band‐gap SiC, III‐V nitride, and II‐VI ZnSe‐based semiconductor device technologies[J]. Journal of Applied Physics. 1994, 76(3): 1363-1398.

[7] R. S. The Past, Present, and Future of Silicon Photonics[J]. IEEE Journal of Selected Topics in Quantum Electronics. 2006, 12(6): 1678-1687.

[8] H. I, S. K, Y. M, et al. High-speed and high-output InP-InGaAs unitraveling-carrier photodiodes[J]. IEEE Journal of Selected Topics in Quantum Electronics. 2004, 10(4): 709-727.

[9] Rogalski A. HgCdTe infrared detector material: history, status and outlook[J]. Reports on Progress in Physics. 2005, 68(10): 2267-2336.

[10] Rogalski A, Antoszewski J, Faraone L. Third-generation infrared photodetector arrays[J]. Journal of Applied Physics. 2009, 105(9): 91101.

[11] B. J, S. F. Silicon Photonics[J]. Journal of Lightwave Technology. 2006, 24(12): 4600-4615.

[12] Huang Z, Carey JE, Liu M, et al. Microstructured silicon photodetector[J]. Applied Physics Letters. 2006, 89(3): 33506.

[13] Dong H, Zhu H, Meng Q, et al. Organic photoresponse materials and devices[J]. Chemical Society Reviews. 2012, 41(5): 1754-1808.

[14] Miles RW, Zoppi G, Forbes I. Inorganic photovoltaic cells[J]. Materials Today. 2007, 10(11): 20-27.
[15] Bao Q, Loh KP. Graphene Photonics, Plasmonics, and Broadband Optoelectronic Devices[J]. ACS Nano. 2012, 6(5): 3677-3694.
[16] Ochoa H, Katsnelson MI, Gorbachev RV, et al. Limits on Charge Carrier Mobility in Suspended Graphene due to Flexural Phonons[J]. Physical Review Letters. 2010, 105(26): 266601.
[17] Nair RR, Blake P, Grigorenko AN, et al. Fine Structure Constant Defines Visual Transparency of Graphene[J]. Science. 2008, 320(5881): 1308.
[18] Lee C, Wei X, Kysar JW, et al. Measurement of the Elastic Properties and Intrinsic Strength of Monolayer Graphene[J]. Science. 2008, 321(5887): 385.
[19] Xia F, Mueller T, Lin Y, et al. Ultrafast graphene photodetector[J]. Nature Nanotechnology. 2009, 4(12): 839-843.
[20] Li J, Niu L, Zheng Z, et al. Photosensitive Graphene Transistors[J]. Advanced Materials. 2014, 26(31): 5239-5273.
[21] Schall D, Neumaier D, Mohsin M, et al. 50 GBit/s Photodetectors Based on Wafer-Scale Graphene for Integrated Silicon Photonic Communication Systems[J]. ACS Photonics. 2014, 1(9): 781-784.
[22] Mueller T, Xia F, Avouris P. Graphene photodetectors for high-speed optical communications[J]. Nature Photonics. 2010, 4(5): 297-301.
[23] Tielrooij KJ, Massicotte M, Piatkowski L, et al. Hot-carrier photocurrent effects at graphene – metal interfaces[J]. Journal of Physics: Condensed Matter. 2015, 27(16): 164207.
[24] Echtermeyer TJ, Nene PS, Trushin M, et al. Photothermoelectric and Photoelectric Contributions to Light Detection in Metal – Graphene – Metal Photodetectors[J]. Nano Letters. 2014, 14(7): 3733-3742.
[25] Mohammadian M, Saghai HR. Room temperature performance analysis of bilayer graphene terahertz photodetector[J]. Optik - International Journal for Light and Electron Optics. 2015, 126(11-12): 1156-1160.
[26] Wang X, Cheng Z, Xu K, et al. High-responsivity graphene/silicon-heterostructure waveguide photodetectors[J]. Nature Photonics. 2013, 7(11): 888-891.
[27] Furchi M, Urich A, Pospischil A, et al. Microcavity-Integrated Graphene Photodetector[J]. Nano Letters. 2012, 12(6): 2773-2777.
[28] Konstantatos G, Badioli M, Gaudreau L, et al. Hybrid graphene – quantum dot phototransistors with ultrahigh gain[J]. Nature Nanotechnology. 2012, 7(6): 363-368.
[29] Kumar M, Jeong H, Polat K, et al. Fabrication and characterization of graphene/AlGaN/GaN ultraviolet Schottky photodetector[J]. Journal of Physics D: Applied Physics. 2016, 49(27): 275105.
[30] Selvi H, Unsuree N, Whittaker E, et al. Towards substrate engineering of graphene – silicon Schottky diode photodetectors[J]. Nanoscale. 2018, 10(7): 3399-3409.
[31] Wan X, Xu Y, Guo H, et al. A self-powered high-performance graphene/silicon ultraviolet photodetector with ultra-shallow junction: breaking the limit of silicon?[J]. npj 2D Materials and Applications. 2017, 1(1): 4.
[32] Li X, Zhu H, Wang K, et al. Graphene-On-Silicon Schottky Junction Solar Cells[J]. Advanced Materials. 2010, 22(25): 2743-2748.

[33] Novoselov KS, Geim AK, Morozov SV, et al. Electric Field Effect in Atomically Thin Carbon Films[J]. Science. 2004, 306(5696): 666.
[34] Geim AK, Novoselov KS. The rise of graphene[J]. Nature Materials. 2007, 6(3): 183-191.
[35] Guinea F, Peres NMR, Novoselov KS, et al. The electronic properties of graphene[J]. Reviews of Modern Physics. 2009, 81(1): 109-162.
[36] Novoselov KS, Geim AK, Morozov SV, et al. Two-dimensional gas of massless Dirac fermions in graphene[J]. Nature. 2005, 438(7065): 197-200.
[37] Wan X, Chen K, Xu J. Interface Engineering for CVD Graphene: Current Status and Progress[J]. Small. 2014, 10(22): 4443-4454.
[38] Geim AK. Graphene: Status and Prospects[J]. Science. 2009, 324(5934): 1530.
[39] Avouris P, Chen Z, Perebeinos V. Carbon-based electronics[J]. Nature Nanotechnology. 2007, 2(10): 605-615.
[40] Ni Z, Wang Y, Yu T, et al. Raman spectroscopy and imaging of graphene[J]. Nano Research. 2008, 1(4): 273-291.
[41] Schmalian J, Sheehy DE. Optical transparency of graphene as determined by the fine-structure constant[J]. Physical Review B. 2009, 80(19): 193411.
[42] Balandin AA, Ghosh S, Bao W, et al. Superior Thermal Conductivity of Single-Layer Graphene[J]. Nano Letters. 2008, 8(3): 902-907.
[43] Zang X, Zhou Q, Chang J, et al. Graphene and carbon nanotube (CNT) in MEMS/NEMS applications[J]. Microelectronic Engineering. 2015, 132: 192-206.
[44] Chen W, Yu Y, Zheng X, et al. All-carbon based graphene field effect transistor with graphitic electrodes fabricated by e-beam direct writing on PMMA[J]. Scientific Reports. 2015, 5(1): 12198.
[45] Zhang Y, Tang T, Girit C, et al. Direct observation of a widely tunable bandgap in bilayer graphene[J]. Nature. 2009, 459(7248): 820-823.
[46] Liu N, Tian H, Schwartz G, et al. Large-Area, Transparent, and Flexible Infrared Photodetector Fabricated Using P-N Junctions Formed by N-Doping Chemical Vapor Deposition Grown Graphene[J]. Nano Letters. 2014, 14(7): 3702-3708.
[47] Chen Z, Cheng Z, Wang J, et al. High Responsivity, Broadband, and Fast Graphene/Silicon Photodetector in Photoconductor Mode[J]. Advanced Optical Materials. 2015, 3(9): 1207-1214.
[48] P. L, X. Z, X. Z, et al. High-Sensitivity and Fast-Response Graphene/Crystalline Silicon Schottky Junction-Based Near-IR Photodetectors[J]. IEEE Electron Device Letters. 2013, 34(10): 1337-1339.
[49] Shin DH, Choi S. Graphene-Based Semiconductor Heterostructures for Photodetectors[J]. Micromachines. 2018, 9(7).
[50] Meyer JC, Geim AK, Katsnelson MI, et al. The structure of suspended graphene sheets[J]. Nature. 2007, 446(7131): 60-63.
[51] Li D, Müller MB, Gilje S, et al. Processable aqueous dispersions of graphene nanosheets[J]. Nature Nanotechnology. 2008, 3(2): 101-105.
[52] May JW. Platinum surface LEED rings[J]. Surface Science. 1969, 17(1): 267-270.
[53] Lang B. A LEED study of the deposition of carbon on platinum crystal surfaces[J]. Surface Science. 1975, 53(1): 317-329.
[54] Eizenberg M, Blakely JM. Carbon monolayer phase condensation on Ni(111)[J]. Surface Science. 1979, 82(1): 228-236.
[55] Blakely JM, Kim JS, Potter HC. Segregation of Carbon to the (100) Surface of Nickel[J]. Journal of Applied Physics. 1970, 41(6): 2693-2697.

[56] Muñoz R, Gómez-Aleixandre C. Review of CVD Synthesis of Graphene[J]. Chemical Vapor Deposition. 2013, 19(10-11-12): 297-322.
[57] Sun X, Lin L, Sun L, et al. Low-Temperature and Rapid Growth of Large Single-Crystalline Graphene with Ethane[J]. Small. 2018, 14(3): 1702916.
[58] Ramón ME, Gupta A, Corbet C, et al. CMOS-Compatible Synthesis of Large-Area, High-Mobility Graphene by Chemical Vapor Deposition of Acetylene on Cobalt Thin Films[J]. ACS Nano. 2011, 5(9): 7198-7204.
[59] Wu T, Ding G, Shen H, et al. Triggering the Continuous Growth of Graphene Toward Millimeter-Sized Grains[J]. Advanced Functional Materials. 2013, 23(2): 198-203.
[60] Zhang B, Lee WH, Piner R, et al. Low-Temperature Chemical Vapor Deposition Growth of Graphene from Toluene on Electropolished Copper Foils[J]. ACS Nano. 2012, 6(3): 2471-2476.
[61] Faggio G, Messina G, Lofaro C, et al. Recent Advancements on the CVD of Graphene on Copper from Ethanol Vapor[J]. Journal of Carbon Research. 2020, 6: 14.
[62] Geng D, Wang H, Yu G. Graphene Single Crystals: Size and Morphology Engineering[J]. Advanced Materials. 2015, 27(18): 2821-2837.
[63] Deokar G, Avila J, Razado-Colambo I, et al. Towards high quality CVD graphene growth and transfer[J]. Carbon. 2015, 89: 82-92.
[64] Mohsin A, Liu L, Liu P, et al. Synthesis of Millimeter-Size Hexagon-Shaped Graphene Single Crystals on Resolidified Copper[J]. ACS Nano. 2013, 7(10): 8924-8931.
[65] Mcnerny DQ, Viswanath B, Copic D, et al. Direct fabrication of graphene on SiO2 enabled by thin film stress engineering[J]. Scientific Reports. 2014, 4(1): 5049.
[66] Chen X, Liu Z, Zheng C, et al. High-quality and efficient transfer of large-area graphene films onto different substrates[J]. Carbon. 2013, 56: 271-278.
[67] Gao L, Ni G, Liu Y, et al. Face-to-face transfer of wafer-scale graphene films[J]. Nature. 2014, 505(7482): 190-194.
[68] Fan Y, He K, Tan H, et al. Crack-Free Growth and Transfer of Continuous Monolayer Graphene Grown on Melted Copper[J]. Chemistry of Materials. 2014, 26(17): 4984-4991.
[69] Fechine GJM, Martin-Fernandez I, Yiapanis G, et al. Direct dry transfer of chemical vapor deposition graphene to polymeric substrates[J]. Carbon. 2015, 83: 224-231.
[70] Goniszewski S, Gallop J, Adabi M, et al. Self-supporting graphene films and their applications[J]. IET Circuits Devices & Systems. 2015, 9(6): 420.
[71] Cha S, Cha M, Lee S, et al. Low-Temperature, Dry Transfer-Printing of a Patterned Graphene Monolayer[J]. Scientific Reports. 2015, 5(1): 17877.
[72] Li X, Zhu Y, Cai W, et al. Transfer of Large-Area Graphene Films for High-Performance Transparent Conductive Electrodes[J]. Nano Letters. 2009, 9(12): 4359-4363.
[73] Liang X, Sperling BA, Calizo I, et al. Toward Clean and Crackless Transfer of Graphene[J]. ACS Nano. 2011, 5(11): 9144-9153.
[74] Kim HH, Lee SK, Lee SG, et al. Wetting-Assisted Crack- and Wrinkle-Free Transfer of Wafer-Scale Graphene onto Arbitrary Substrates over a Wide Range of Surface Energies[J]. Advanced Functional Materials. 2016, 26(13): 2070-2077.

[75] Bae S, Kim H, Lee Y, et al. Roll-to-roll production of 30-inch graphene films for transparent electrodes[J]. Nature Nanotechnology. 2010, 5(8): 574-578.
[76] Her M, Beams R, Novotny L. Graphene transfer with reduced residue[J]. Physics Letters A. 2013, 377(21): 1455-1458.
[77] Lin Y, Lu C, Yeh C, et al. Graphene Annealing: How Clean Can It Be?[J]. Nano Letters. 2012, 12(1): 414-419.
[78] Suhail A, Islam K, Li B, et al. Reduction of polymer residue on wet‐transferred CVD graphene surface by deep UV exposure[J]. Applied Physics Letters. 2017, 110(18): 183103.
[79] Lin W, Chen T, Chang J, et al. A Direct and Polymer-Free Method for Transferring Graphene Grown by Chemical Vapor Deposition to Any Substrate[J]. ACS Nano. 2014, 8(2): 1784-1791.
[80] Zhang G, Güell AG, Kirkman PM, et al. Versatile Polymer-Free Graphene Transfer Method and Applications[J]. ACS Applied Materials & Interfaces. 2016, 8(12): 8008-8016.
[81] Echtermeyer TJ, Britnell L, Jasnos PK, et al. Strong plasmonic enhancement of photovoltage in graphene[J]. Nature Communications. 2011, 2(1): 458.
[82] Cakmakyapan S, Jarrahi M. High responsivity and bias-free graphene photodetector with nano-grating contact electrodes[M]. San Jose, California: Optical Society of America. 2018: h3H-h4H.
[83] Grigorenko AN, Polini M, Novoselov KS. Graphene plasmonics[J]. Nature Photonics. 2012, 6(11): 749-758.
[84] Liu Y, Cheng R, Liao L, et al. Plasmon resonance enhanced multicolour photodetection by graphene[J]. Nature Communications. 2011, 2(1): 579.
[85] Wang J, Song J, Mu X, et al. Optoelectronic and photoelectric properties and applications of graphene-based nanostructures[J]. Materials Today Physics. 2020, 13: 100196.
[86] Png CE, Sun S, Bai P. State-of-the-art photodetectors for optoelectronic integration at telecommunication wavelength[J]. Nanophotonics. 2015, 4(3): 277-302.
[87] An X, Liu F, Jung YJ, et al. Tunable Graphene‐Silicon Heterojunctions for Ultrasensitive Photodetection[J]. Nano Letters. 2013, 13(3): 909-916.
[88] Zhu M, Li X, Guo Y, et al. Vertical junction photodetectors based on reduced graphene oxide/silicon Schottky diodes[J]. Nanoscale. 2014, 6(9): 4909-4914.
[89] Cao Y, Zhu J, Xu J, et al. Ultra-Broadband Photodetector for the Visible to Terahertz Range by Self-Assembling Reduced Graphene Oxide-Silicon Nanowire Array Heterojunctions[J]. Small. 2014, 10(12): 2345-2351.
[90] Zhu X, Yan W, Uhd Jepsen P, et al. Experimental observation of plasmons in a graphene monolayer resting on a two-dimensional subwavelength silicon grating[J]. Applied Physics Letters. 2013, 102(13): 131101.
[91] Luo L, Zeng L, Xie C, et al. Light trapping and surface plasmon enhanced high-performance NIR photodetector[J]. Scientific Reports. 2014, 4(1): 3914.
[92] Kim J, Joo SS, Lee KW, et al. Near-Ultraviolet-Sensitive Graphene/Porous Silicon Photodetectors[J]. ACS Applied Materials & Interfaces. 2014, 6(23): 20880-20886.
[93] Zhu M, Zhang L, Li X, et al. TiO2 enhanced ultraviolet detection based on a graphene/Si Schottky diode[J]. Journal of Materials Chemistry A. 2015, 3(15): 8133-8138.

[94] S. R, D. S, C. Y, et al. Spectral sensitivity of a graphene/silicon pn-junction photodetector[M]. 2015: 77-80.
[95] Lin Y, Li X, Xie D, et al. Graphene/semiconductor heterojunction solar cells with modulated antireflection and graphene work function[J]. Energy & Environmental Science. 2013, 6(1): 108-115.
[96] Li X, Xie D, Park H, et al. Anomalous Behaviors of Graphene Transparent Conductors in Graphene – Silicon Heterojunction Solar Cells[J]. Advanced Energy Materials. 2013, 3(8): 1029-1034.
[97] Shi E, Li H, Yang L, et al. Colloidal Antireflection Coating Improves Graphene – Silicon Solar Cells[J]. Nano Letters. 2013, 13(4): 1776-1781.
[98] Li X, Zang X, Li X, et al. Hybrid Heterojunction and Solid-State Photoelectrochemical Solar Cells[J]. Advanced Energy Materials. 2014, 4(14): 1400224.
[99] Li X, Xie D, Park H, et al. Ion doping of graphene for high-efficiency heterojunction solar cells[J]. Nanoscale. 2013, 5(5): 1945-1948.
[100] Song Y, Li X, Mackin C, et al. Role of Interfacial Oxide in High-Efficiency Graphene – Silicon Schottky Barrier Solar Cells[J]. Nano Letters. 2015, 15(3): 2104-2110.
[101] Yang H, Heo J, Park S, et al. Graphene Barristor, a Triode Device with a Gate-Controlled Schottky Barrier[J]. Science. 2012, 336(6085): 1140.
[102] Chen C, Aykol M, Chang C, et al. Graphene-Silicon Schottky Diodes[J]. Nano Letters. 2011, 11(5): 1863-1867.
[103] Sinha D, Lee JU. Ideal Graphene/Silicon Schottky Junction Diodes[J]. Nano Letters. 2014, 14(8): 4660-4664.
[104] Singh A, Uddin MA, Sudarshan T, et al. Tunable Reverse-Biased Graphene/Silicon Heterojunction Schottky Diode Sensor[J]. Small. 2014, 10(8): 1555-1565.
[105] Kim H, Lee K, Mcevoy N, et al. Chemically Modulated Graphene Diodes[J]. Nano Letters. 2013, 13(5): 2182-2188.
[106] Kim J, Oh SD, Kim JH, et al. Graphene/Si-nanowire heterostructure molecular sensors[J]. Scientific Reports. 2014, 4(1): 5384.
[107] Zhu M, Li X, Chung S, et al. Photo-induced selective gas detection based on reduced graphene oxide/Si Schottky diode[J]. Carbon. 2015, 84: 138-145.
[108] F. R, C. EB. On black solar cells or the tetrahedral texturing of a silicon surface[J]. IEEE Transactions on Electron Devices. 1976, 23(10): 1195-1197.
[109] X. M, Z. L, H. L, et al. Surface Texturisation of Monocrystalline Silicon Solar Cells[M]. 2011: 1-4.
[110] Xie C, Zhang X, Ruan K, et al. High-efficiency, air stable graphene/Si micro-hole array Schottky junction solar cells[J]. Journal of Materials Chemistry A. 2013, 1(48): 15348-15354.
[111] Wu Y, Zhang X, Jie J, et al. Graphene Transparent Conductive Electrodes for Highly Efficient Silicon Nanostructures-Based Hybrid Heterojunction Solar Cells[J]. The Journal of Physical Chemistry C. 2013, 117(23): 11968-11976.
[112] Zhang X, Xie C, Jie J, et al. High-efficiency graphene/Si nanoarray Schottky junction solar cells via surface modification and graphene doping[J]. Journal of Materials Chemistry A. 2013, 1(22): 6593-6601.

[113] Feng T, Xie D, Lin Y, et al. Efficiency enhancement of graphene/silicon-pillar-array solar cells by HNO3 and PEDOT-PSS[J]. Nanoscale. 2012, 4(6): 2130-2133.
[114] Shin DH, Kim JH, Kim JH, et al. Graphene/porous silicon Schottky-junction solar cells[J]. Journal of Alloys and Compounds. 2017, 715: 291-296.
[115] Shin DH, Kim JM, Jang CW, et al. Effect of layer number and metal-chloride dopant on multiple layers of graphene/porous Si solar cells[J]. Journal of Applied Physics. 2018, 123(12): 123101.
[116] Shin DH, Jang CW, Kim JM, et al. Self-powered Ag-nanowires-doped graphene/Si quantum dots/Si heterojunction photodetectors[J]. Journal of Alloys and Compounds. 2018, 758: 32-37.
[117] Shin DH, Kim S, Kim JM, et al. Graphene/Si-Quantum-Dot Heterojunction Diodes Showing High Photosensitivity Compatible with Quantum Confinement Effect[J]. Advanced Materials. 2015, 27(16): 2614-2620.
[118] Di Bartolomeo A, Giubileo F, Luongo G, et al. Tunable Schottky barrier and high responsivity in graphene/Si-nanotip optoelectronic device[J]. 2D Materials. 2016, 4(1): 15024.
[119] Luongo G, Giubileo F, Iemmo L, et al. The role of the substrate in Graphene/Silicon photodiodes[J]. Journal of Physics: Conference Series. 2018, 956: 12019.
[120] Luongo G, Grillo A, Urban F, et al. Effect of silicon doping on graphene/silicon Schottky photodiodes[J]. Materials Today: Proceedings. 2020, 20: 82-86.
[121] Luongo G, Di Bartolomeo A, Giubileo F, et al. Electronic properties of graphene/p-silicon Schottky junction[J]. Journal of Physics D: Applied Physics. 2018, 51(25): 255305.
[122] Ryu S, Liu L, Berciaud S, et al. Atmospheric Oxygen Binding and Hole Doping in Deformed Graphene on a SiO2 Substrate[J]. Nano Letters. 2010, 10(12): 4944-4951.
[123] Schedin F, Geim AK, Morozov SV, et al. Detection of individual gas molecules adsorbed on graphene[J]. Nature Materials. 2007, 6(9): 652-655.
[124] Swami NK, Srivastava S, Ghule HM. The role of the interfacial layer in Schottky barrier solar cells[J]. Journal of Physics D: Applied Physics. 1979, 12(5): 765-771.
[125] Li X, Zhu M, Du M, et al. High Detectivity Graphene-Silicon Heterojunction Photodetector[J]. Small. 2016, 12(5): 595-601.
[126] Alnuaimi A, Almansouri I, Saadat I, et al. Interface engineering of graphene – silicon Schottky junction solar cells with an Al2O3 interfacial layer grown by atomic layer deposition[J]. RSC Advances. 2018, 8(19): 10593-10597.
[127] Miao X, Tongay S, Petterson MK, et al. High Efficiency Graphene Solar Cells by Chemical Doping[J]. Nano Letters. 2012, 12(6): 2745-2750.
[128] Cui T, Lv R, Huang Z, et al. Enhanced efficiency of graphene/silicon heterojunction solar cells by molecular doping[J]. Journal of Materials Chemistry A. 2013, 1(18): 5736-5740.
[129] An X, Liu F, Kar S. Optimizing performance parameters of graphene – silicon and thin transparent graphite – silicon heterojunction solar cells[J]. Carbon. 2013, 57: 329-337.

[130] Liu X, Zhang XW, Yin ZG, et al. Enhanced efficiency of graphene-silicon Schottky junction solar cells by doping with Au nanoparticles[J]. Applied Physics Letters. 2014, 105(18): 183901.
[131] Liu X, Zhang XW, Meng JH, et al. High efficiency Schottky junction solar cells by co-doping of graphene with gold nanoparticles and nitric acid[J]. Applied Physics Letters. 2015, 106(23): 233901.
[132] Yang L, Yu X, Xu M, et al. Interface engineering for efficient and stable chemical-doping-free graphene-on-silicon solar cells by introducing a graphene oxide interlayer[J]. Journal of Materials Chemistry A. 2014, 2(40): 16877-16883.
[133] Huang K, Yan Y, Li K, et al. High and Fast Response of a Graphene–Silicon Photodetector Coupled with 2D Fractal Platinum Nanoparticles[J]. Advanced Optical Materials. 2018, 6(1): 1700793.
[134] Aydın H, Kalkan SB, Varlikli C, et al. P3HT–graphene bilayer electrode for Schottky junction photodetectors[J]. Nanotechnology. 2018, 29(14): 145502.
[135] Meyer JC, Scardaci V, Casiraghi C, et al. Raman Spectrum of Graphene and Graphene Layers[J]. Physical Review Letters. 2006, 97(18): 187401.
[136] Malard LM, Pimenta MA, Dresselhaus G, et al. Raman spectroscopy in graphene[J]. Physics Reports. 2009, 473(5): 51-87.
[137] Bie Y, Zhou Y, Liao Z, et al. Site-Specific Transfer-Printing of Individual Graphene Microscale Patterns to Arbitrary Surfaces[J]. Advanced Materials. 2011, 23(34): 3938-3943.
[138] Liu R, Fu X, Meng J, et al. Graphene plasmon enhanced photoluminescence in ZnO microwires[J]. Nanoscale. 2013, 5(12): 5294-5298.
[139] Cançado LG, Jorio A, Ferreira EHM, et al. Quantifying Defects in Graphene via Raman Spectroscopy at Different Excitation Energies[J]. Nano Letters. 2011, 11(8): 3190-3196.
[140] Park JS, Reina A, Saito R, et al. G′ band Raman spectra of single, double and triple layer graphene[J]. Carbon. 2009, 47(5): 1303-1310.
[141] Solin SA, Nemanich RJ. First- and second-order Raman scattering from finite-size crystals of graphite[J]. Physical Review B. 1979, 20(2): 392-401.
[142] Cançado LG, Takai K, Enoki T, et al. General equation for the determination of the crystallite size La of nanographite by Raman spectroscopy[J]. Applied Physics Letters. 2006, 88(16): 163106.
[143] Di Bartolomeo A. Graphene Schottky diodes: An experimental review of the rectifying graphene/semiconductor heterojunction[J]. Physics Reports. 2016, 606: 1-58.
[144] Di Bartolomeo A, Luongo G, Giubileo F, et al. Hybrid Graphene/Silicon Schottky photodiode with intrinsic gating effect[J]. 2D Materials. 2017, 4: 25075.
[145] A. DB, G. L, L. I, et al. Graphene–Silicon Schottky Diodes for Photodetection[J]. IEEE Transactions on Nanotechnology. 2018, 17(6): 1133-1137.
[146] Guo H, Jou S, Mao T, et al. Silicon- and oxygen-codoped graphene from polycarbosilane and its application in graphene/n-type silicon photodetectors[J]. Applied Surface Science. 2019, 464: 125-130.
[147] Rao LD, Reddy VR. Electrical parameters and series resistance analysis of Au/Y/p-InP/Pt Schottky barrier diode at room temperature[J]. AIP Conference Proceedings. 2016, 1731(1): 120020.

[148] Cheung SK, Cheung NW. Extraction of Schottky diode parameters from forward current‐voltage characteristics[J]. Applied Physics Letters. 1986, 49(2): 85-87.
[149] Norde H. A modified forward I‐V plot for Schottky diodes with high series resistance[J]. Journal of Applied Physics. 1979, 50(7): 5052-5053.
[150] Riazimehr S, Belete M, Kataria S, et al. Capacitance‐Voltage (C‐V) Characterization of Graphene‐Silicon Heterojunction Photodiodes[J]. Advanced Optical Materials. 2020, n/a(n/a): 2000169.
[151] Aydoğan ^, 0ncekara Ü, Deniz AR, et al. Extraction of electronic parameters of Schottky diode based on an organic Orcein[J]. Microelectronic Engineering. 2010, 87(12): 2525-2530.
[152] Dutta M, Basak D. p-ZnO / n-Si heterojunction: Sol-gel fabrication, photoresponse properties, and transport mechanism[J]. Applied Physics Letters. 2008, 92(21): 212112.
[153] El-Sayed SM, Abdel Hamid HM, Radwan RM. Effect of electron beam irradiation on the conduction phenomena of unplasticized PVC/PVA copolymer[J]. Radiation Physics and Chemistry. 2004, 69(4): 339-345.
[154] E. HR. Metal-semiconductor contacts[J]. IEE Proceedings I - Solid-State and Electron Devices. 1982, 129(1): 1.
[155] Han F, Yang S, Jing W, et al. A highly efficient synthetic process of graphene films with tunable optical properties[J]. Applied Surface Science. 2014, 314: 71-77.
[156] Zhao J, Liu L, Li F. Application of GO in Energy Conversion and Storage[M]// Zhao J, Liu L, Li F. Graphene Oxide: Physics and Applications. Berlin, Heidelberg: Springer Berlin Heidelberg. 2015: 79-118.
[157] Darbari S, Ahmadi V, Afzali P, et al. Reduced graphene oxide/ZnO hybrid structure for high-performance photodetection[J]. Journal of Nanoparticle Research. 2014, 16(12): 2798.
[158] Liu Y, Yu C, Lin K, et al. Transparent, Broadband, Flexible, and Bifacial-Operable Photodetectors Containing a Large-Area Graphene‐Gold Oxide Heterojunction[J]. ACS Nano. 2015, 9(5): 5093-5103.
[159] Zhan Z, Zheng L, Pan Y, et al. Self-powered, visible-light photodetector based on thermally reduced graphene oxide‐ZnO (rGO‐ZnO) hybrid nanostructure[J]. Journal of Materials Chemistry. 2012, 22(6): 2589-2595.
[160] Ghosh S, Sarker BK, Chunder A, et al. Position dependent photodetector from large area reduced graphene oxide thin films[J]. Applied Physics Letters. 2010, 96(16): 163109.
[161] Gnisci A, Faggio G, Lancellotti L, et al. The Role of Graphene-Based Derivative as Interfacial Layer in Graphene/n-Si Schottky Barrier Solar Cells[J]. physica status solidi (a). 2019, 216(3): 1800555.
[162] Xiang D, Han C, Hu Z, et al. Surface Transfer Doping-Induced, High-Performance Graphene/Silicon Schottky Junction-Based, Self-Powered Photodetector[J]. Small. 2015, 11(37): 4829-4836.
[163] Jang M, Trung TQ, Jung J, et al. Improved performance and stability of field-effect transistors with polymeric residue-free graphene channel transferred by gold layer[J]. Physical Chemistry Chemical Physics. 2014, 16(9): 4098-4105.
[164] Seok K, Min, Seok K, et al. Graphene treatment using a very low energy Ar+ ion beam for residue removal.[J]. Journal of nanoscience and nanotechnology. 2014.

[165] Kim S, Shin S, Kim T, et al. Robust graphene wet transfer process through low molecular weight polymethylmethacrylate[J]. Carbon. 2016, 98: 352-357.
[166] Ballesio A, Parmeggiani M, Verna A, et al. A novel hot embossing Graphene transfer process for flexible electronics[J]. Microelectronic Engineering. 2019, 209: 16-19.
[167] Ni Z, Wang Y, Yu T, et al. Raman spectroscopy and imaging of graphene[J]. Nano Research. 2008, 1(4): 273-291.
[168] Dasaradha Rao L, Shanthi Latha K, Rajagopal Reddy V, et al. Effect of thermal annealing on the electrical and structural properties of Au/Y/p-type InP Schottky structure[J]. Vacuum. 2015, 119: 276-283.
[169] Zeng L, Wang M, Hu H, et al. Monolayer Graphene/Germanium Schottky Junction As High-Performance Self-Driven Infrared Light Photodetector[J]. ACS Applied Materials & Interfaces. 2013, 5(19): 9362-9366.
[170] Shafique S, Yang S, Woldu YT, et al. Hierarchical synthesis of urchin-like V2O5 hollow spheres and its photodetection properties[J]. Sensors and Actuators A: Physical. 2019, 288: 107-116.
[171] Shafique S, Yang S, Wang Y, et al. High-performance photodetector using urchin-like hollow spheres of vanadium pentoxide network device[J]. Sensors and Actuators A: Physical. 2019, 296: 38-44.

Appendix A. Publication list

[1] **Wang YM**, Yang SM, Lambada DR, et al. A graphene-silicon Schottky photodetector with graphene oxide interlayer[J]. Sensors and Actuators A: Physical, 2020, 314:112232. (SCI: 000579547300001; EI: 20203209018324).

[2] **Wang YM**, Yang SM, Ballesio A, et al. The fabrication of Schottky photodiode by monolayer graphene direct-transfer-on-silicon[J]. Journal of Applied Physics, 2020, 128(1):014501. (SCI: 000551878300001; EI: 20202808925789).

[3] Yang SM, **Wang YM**, Wang LJ, et al. Growth and characterization of ultra-long ZnO nanocombs[J]. AIP Advances, 2016, 6(6):065209. (SCI: 000379041400063; EI: 20162502510297).

[4] Shafique S, Yang SM, **Wang YM**, et al. High-performance photodetector using urchin-like hollow spheres of vanadium pentoxide network device[J]. Sensors and Actuators A: Physical, 2019, 296: 38-44. (SCI: 000485206300006; EI: 20192807167073).

[5] Li CS, Yang SM, **Wang YM**, et al. Measurement and characterization of a nano-scale multiple-step height sample using a stylus profiler.[J]. Applied Surface Science, 2016, 387: 732-735. (SCI: 000381251100089; EI: 20162902599404).

[6] Yang SM, Wang LJ, **Wang YM**, et al. Identification and characteristics of ZnO/MgO core-shell nanowires[J]. AIP Advances, 2015, 5(3). (SCI: 000352449500023; EI: 20151200649119).